

BULK AMORPHOUS/NANOCRYSTALLINE MATERIALS: STRUCTURAL  
AMORPHOUS STEELS

A THESIS SUBMITTED TO  
THE GRADUATE SCHOOL OF NATURAL AND APPLIED SCIENCES  
OF  
MIDDLE EAST TECHNICAL UNIVERSITY

BY

BENĞI YAĞMURLU

IN PARTIAL FULFILLMENT OF THE REQUIREMENTS  
FOR  
THE DEGREE OF MASTER OF SCIENCE  
IN  
METALLURGICAL AND MATERIALS ENGINEERING

DECEMBER 2014



Approval of the thesis:

**BULK AMORPHOUS/NANOCRYSTALLINE MATERIALS:  
STRUCTURAL AMORPHOUS STEELS**

submitted by **BENĐI YAĐMURLU** in partial fulfillment of the requirements for the degree of **Master of Science in Metallurgical and Materials Engineering Department, Middle East Technical University** by,

Prof. Dr. Gölbin Dural Ünver  
Dean, Graduate School of **Natural and Applied Sciences**

\_\_\_\_\_

Prof. Dr. Hakan C. Gür  
Head of Department, **Metallurgical and Materials Eng.**

\_\_\_\_\_

Prof. Dr. M. Vedat Akdeniz  
Supervisor, **Metallurgical and Materials Eng. Dept., METU**

\_\_\_\_\_

Prof. Dr. Amdulla O. Mekhrabov  
Co-Supervisor, **Metallurgical and Materials Eng. Dept., METU**

\_\_\_\_\_

**Examining Committee Members:**

Assoc. Prof. Dr. Y. Eren Kalay  
Metallurgical and Materials Eng. Dept., METU

\_\_\_\_\_

Prof. Dr. M. Vedat Akdeniz  
Metallurgical and Materials Eng. Dept., METU

\_\_\_\_\_

Prof. Dr. Amdulla O. Mekhrabov  
Metallurgical and Materials Eng. Dept., METU

\_\_\_\_\_

Assoc. Prof. Dr. Ziya Esen  
Materials Science and Eng. Dept., Çankaya Uni.

\_\_\_\_\_

Assist. Prof. Dr. Mert Efe  
Metallurgical and Materials Eng. Dept., METU

\_\_\_\_\_

Date: 30.12.2014

**I hereby declare that all information in this document has been obtained and presented with academic rules and ethical conduct. I also declare that, as required by those rules and conduct, I have fully cited and referenced all material and results that are not original to this work.**

Name, Last Name: Yağmurlu, Bengi

Signature:

## **ABSTRACT**

### **BULK AMORPHOUS/NANOCRYSTALLINE MATERIALS: STRUCTURAL AMORPHOUS STEELS**

Yağmurlu, Bengi

M.S., Department of Metallurgical and Materials Engineering

Supervisor: Prof. Dr. M. Vedat Akdeniz

Co-Supervisor: Prof Dr. Amdulla O. Mekhrabov

December 2014, 115 pages

Although conventional steels with crystalline structures have been extensively utilized by industries, bulk amorphous steels (BASs) show great potential to supersede these crystalline steels for some critical structural and functional applications because of their unusual combinations of engineering properties: these include higher strength and hardness, better wear and corrosion resistance. Moreover, compared with most other bulk amorphous alloy systems such as Zr- and Pd-based bulk metallic glasses, BASs offer some important advantages: much lower material cost, higher strength, better corrosion resistance, and higher thermal stability (the glass transition temperatures are close to or above 800 K). However, like all metallic glasses, usage of high purity constituent elements and advanced production methods, made commercial usage of BASs difficult due to production cost. Moreover, it is necessary to improve the glass forming abilities (GFA) of Fe-

based alloys in order to enhance their ability to form bulk glassy steels under conventional industrial conditions.

In this study, BASs design and production was successfully achieved from commercially available scrap cast irons by conventional centrifugal casting machine. For the first time, BAS production was succeeded from scrap precursors. Although the glassy phases of the initially produced base alloy had extremely wide supercooled liquid region ( $\sim 120\text{K}$ ),  $T_g$  (816K) needed to be improved for higher thermal stability. To destabilize the carbides formed in base alloy and to enhance the thermal properties of the BAS samples, different alloying additions with same amount of Mo substitutions were applied and Mn was determined as the best among the others.

In the second part of the study, the Mn was content tried to be optimized by microalloying technique. As Mn content increased up to 7at.% in composition, improved GFA was obtained from samples; however, after that point samples showed a decrease in GFA. The samples with 7at.% Mn showed high  $T_g$  (863K) with relatively low  $\Delta T_x$  (25K), high glass forming ability with necessity of low critical cooling rate to suppress nucleation, extreme hardness near 1200HV and superior corrosion resistance in extreme environments.

**Keywords:** Metallic Glasses, Bulk Amorphous Alloys, Amorphous Steels

## ÖZ

### İRİ HACİMLİ CAMSI/NANOKRİSTAL MALZEMELER: CAMSI YAPI ÇELİKLERİ

Yağmurlu, Bengi

Yüksek Lisans, Metalurji ve Malzeme Mühendisliği Bölümü

Tez Yöneticisi: Prof. Dr. M. Vedat Akdeniz

Ortak Tez Yöneticisi: Prof Dr. Amdulla O. Mekhrabov

Aralık 2014, 115 sayfa

Kristal yapıya sahip geleneksel çelikler endüstride yaygın olarak kullanılmasına rağmen, iri hacimli camsı çelikler (İHCÇ), sahip oldukları özellikler sayesinde, kritik değere sahip parçalarda geleneksel çeliklerin yerini alma potansiyeline sahip malzemelerdir. Bu sıra dışı özellikler, yüksek mukavemet ve sertlik, daha iyi aşınma ve korozyon direncidir. Bunlara ek olarak, Zr ve Pd esaslı iri hacimli camsı metallerle karşılaştırıldığında da, bu malzemelere karşı bir çok avantaj sergilemiştir: düşük maliyet, yüksek mukavemet, yüksek korozyon direnci ve daha yüksek ısı istikrarı. Ancak, diğer camsı metal türlerinde de olduğu gibi, yüksek saflıkta element ve ileri üretim yöntemlerinin kullanılması, İHCÇlerin ticari alanda kullanılmasına engel oluşturmaktadırlar. Aynı zamanda, bu ileri malzemelerin geleneksel yöntemler

ile üretilebilmeleri için cam oluşturma eğilimlerinin (COE) de geliştirilmesi gerekmektedir.

Bu çalışmada, İHCÇ tasarımı ve üretimi ana malzeme olarak hurda dökme demir ve geleneksel santrifüj döküm yöntemi kullanılarak başarıyla üretilmiştir. İHCÇ üretimi ilk kez hurda malzeme kullanımı ile başarıya ulaşmıştır. Üretilen baz alaşımın çok geniş aşırı soğumuş eriyik bölgesi bulunmasına rağmen, görece düşük cama geçiş sıcaklığına sahip olması, termal olarak kararlılığının geliştirmesi gerekliliğini göstermektedir. Baz alaşımında gözlenen karbit fazlarının kararsız hale getirilmesi ve termal kararlılığının artırılması amacıyla değişik alaşım element ilaveleri yapılmıştır. Bu element ilavelerinin sonuçlarına göre, aralarında en iyisinin Mn olduğu gözlemlenmiştir.

Çalışmanın ikinci kısmında ise, alaşımlarda bulunan Mn miktarı mikroalaşımlama yöntemi kullanılarak optimize edilmeye çalışılmıştır. Numunelerdeki Mn miktarı 7%at. seviyesine çıkarıldığında COE de bu limite kadar artış gözlemlenmiş, fakat, bu seviyeden sonra tekrar düşüş gözlemlenmiştir. 7% at Mn içeren numunelerde yüksek cama geçiş sıcaklığı, görece dar aşırı soğumuş eriyik bölgesi, gelişmiş COE ile çekirdeklenmenin engellenmesi için düşük kritik soğuma hızı, aşırı sertlik ve çok yüksek korozyon direnci gözlemlenmiştir.

**Anahtar Kelimeler:** Camsı Metaller, İri Hacimli Camsı Alaşımlar, İri Hacimli Camsı Çelikler

To my dear family;

## ACKNOWLEDGEMENTS

First and foremost, I would like to express my sincere appreciation and gratitude to my supervisors Prof. Dr. M. Vedat Akdeniz and Prof. Dr. Amdulla O. Mekhrabov for their limitless and continuous guidance, wisdom, never-ending belief and their endless patience and understanding in preparation of this thesis.

I would like to express my gratitude to HABAŞ, İstanbul; especially to the technical manager Hakkı Çakmak for their support in this study and for providing scrap pig iron which was used to produce bulk amorphous steels.

I would like to thank my colleagues and friends Mehmet Yıldırım, Gülten Kılıç, Orkun Muğan, Bahadır Can Kocaoğlu, Amir Fadaie, Mahsuni Yalçın and Utku Olgun who were with me and helped me along the way with their emotional support, guidance, suggestions, and valuable friendships. I would like to present my special thanks to my friends Mehmet Dincer, Kıvanç Korkmaz, Onur Saka, Özgün Yalçın and Çağrı Arıcı whom we spent most our time together throughout my journey which was full of laughter and joy.

I would like to thank specially to my dear, Başak Kalelioğlu, for her endless support, understanding and patience. In all stages of my study, she not only shared my burdens and helped me to overcome but also brought joy to my life. She was there for me every time I needed.

At last but not least, I would like to express my gratitude to my family for their support, patience and guidance throughout my education life. They helped and mentored during my whole life and influenced my vision.

## TABLE OF CONTENTS

ABSTRACT .....	v
ÖZ .....	vii
ACKNOWLEDGEMENTS .....	x
TABLE OF CONTENTS .....	xi
LIST OF TABLES .....	xv
LIST OF FIGURES .....	xvii
CHAPTERS	
1. INTRODUCTION .....	1
2. THEORETICAL BACKGROUND .....	5
THEORETICAL BACKGROUND .....	5
2.1. Early Developments of Metallic Glasses .....	5
2.2. BMG Systems and Their Features.....	6
2.2.1. Thermodynamic and Kinetic Aspects of Metallic Glasses.....	6
2.2.2. Design of a BMG Alloy.....	8
2.2.3. Structures of BMG systems .....	11
2.3. Fe-Based BMGs .....	12
2.3.1. Properties of Fe-Based BMGs .....	14
2.3.1.1. Magnetic Properties .....	14
2.3.1.2. Mechanical Properties .....	15
2.3.1.2.1. Non-Uniform Deformation of BMGs.....	15
2.3.1.2.2. Uniform Deformation of BMGs.....	16
2.3.1.2.3. Mechanical Properties of Fe-Based BMGs .....	17

2.3.1.3. Thermal Properties of Fe-Based BMGs .....	19
2.3.1.4. Corrosion Properties of Fe-Based BMGs.....	21
2.4. Bulk Amorphous Steels .....	22
2.4.1. Previous Studies .....	23
2.4.2. Effects of Alloying Elements .....	25
2.4.3. Production Methods of Bulk Amorphous Steels.....	27
2.4.3.1. Copper Mold Casting .....	27
2.4.3.2. Suction Casting.....	27
2.4.3.3. Centrifugal Casting.....	28
2.5. Glass Forming Ability and Parameters .....	29
2.5.1. Reduced Glass Transition Temperature ( $T_{rg}$ ).....	29
2.5.2. Supercooled Liquid Region ( $\Delta T_x$ ) .....	29
2.5.3. The $\gamma$ and $\gamma_m$ Parameters .....	30
2.5.4. The $\alpha$ and $\beta$ Parameters.....	30
2.5.5. The $\omega$ Parameter.....	31
2.5.6. Ideal Value of the GFA Parameters .....	31
2.6. Crystallization Kinetics .....	32
2.6.1. Isochronal Crystallization Kinetics .....	32
2.6.2. Isothermal Crystallization Kinetics.....	33
3. EXPERIMENTAL PROCEDURE.....	35
3.1. Raw Materials.....	35
3.2. Production of the Samples .....	36
3.2.1. Arc Melting .....	37
3.2.2. Rapid Solidification by Centrifugal Casting .....	37
3.2.3. Rapid Solidification Suction Casting .....	37

3.3. Characterization Techniques .....	38
3.3.1. X-Ray Diffractometry .....	38
3.3.2. Microstructural Investigation.....	39
3.3.3. Differential Scanning Calorimetry.....	39
3.3.4. Vibrating Sample Magnetometry.....	40
3.3.5. Micro-Hardness Measurements .....	40
3.3.6. Corrosion Tests .....	40
4. SYNTHESIS OF BULK AMORPHOUS STEELS IN AN ECONOMICAL AND CONVENTIONAL MANNER.....	41
4.1. Introduction .....	41
4.2. Design, Production and Characterization of Base Alloy.....	42
4.3. Carbide Destabilization by Alloying Element Addition .....	45
4.4. Effect of Al and Mn.....	53
5. IDENTIFYING THE BEST MANGANESE CONTENT FOR ENHANCED PROPERTIES OF BULK AMORPHOUS STEELS PRODUCED BY SCRAP CAST IRONS .....	61
5.1. Introduction and Aim .....	61
5.2. Production Route and Microalloying .....	62
5.3. Effect of Mn Addition on Thermal Characteristics.....	64
5.4. Effect of Mn addition on Magnetic Properties .....	71
5.5. Near Equilibrium Solidification and Microstructural Investigation.....	74
5.6. Effect of Mn addition on Mechanical Properties .....	83
5.7. Identifying the best Alloy System .....	85
5.7.1. Critical Temperatures and Glass Forming Ability.....	85
5.7.2. Crystallization Kinetics.....	86
5.7.3. Corrosion Studies.....	93

5.7.4. Mechanical Properties.....	97
6. CONCLUSION .....	99
REFERENCES .....	103
APPENDICES	
A. T <sub>g</sub> CALCULATION.....	115

## LIST OF TABLES

### TABLES

Table 2.1 Previously investigated non-ferrous BMG systems in literature are arranged according to the first paper of each alloy published .....	12
Table 2.2 Previously investigated ferrous BMG systems in literature arranged according to first paper of each alloy published .....	13
Table 2.3 Summary of the Fe-based BMG systems in the literature with their glass transition temperature ( $T_g$ ), crystallization temperature ( $T_x$ ), supercooled liquid region ( $\Delta T_x$ ) and the years alloys are first published. ....	19
Table 2.4 BAS systems and their critical thermal parameters .....	23
Table 2.5 Ideal values of the discussed GFA parameters .....	31
Table 3.1 The elements in the scrap cast iron and their weight percentages .....	35
Table 3.2 The purity grades of the elements used in the alloy preparation .....	36
Table 4.1 Critical thermal parameters of samples $M_{60}Cr_{13}Mo_{14}B_8Y_2X_3$ .....	49
Table 4.2 GFA parameters of base alloy and $M_{60}Cr_{13}Mo_{14}B_8Y_2X_3$ .....	50
Table 4.3 Critical temperatures for $M_{60}Cr_{13}Mo_{17-x}B_8Y_2Al_x$ and $M_{60}Cr_{13}Mo_{17-x}B_8Y_2Mn_x$ alloys.....	56
Table 4.4 GFA parameters of $M_{60}Cr_{13}Mo_{17-x}B_8Y_2Al_x$ and $M_{60}Cr_{13}Mo_{17-x}B_8Y_2Mn_x$ alloys .....	56
Table 5.1 Critical temperatures of the $M_{60}Cr_{13}Mo_{17-x}B_8Y_2Mn_x$ alloy system where x varies from 0 to 10 .....	69
Table 5.2 Glass forming ability parameters of the $M_{60}Cr_{13}Mo_{17-x}B_8Y_2Mn_x$ alloy system where x varies from 0 to 10 .....	70

Table 5.3 Critical temperatures and GFA parameters of the $M_{60}Cr_{13}Mo_{10}B_8Y_2Mn_7$ BASs.....	86
Table 5.4 Critical temperatures at 5 K/min, 10 K/min, 20 K/min and 40 K/min.....	87
Table 5.5 Activation energies for glass transition and crystallization calculated from Kissinger plots.....	89
Table 5.6 Activation energies for glass transition and crystallization calculated from Kissinger plots.....	90
Table 5.7 Critical temperatures at different heating rates .....	91

## LIST OF FIGURES

### FIGURES

Figure 2.1 Viscosity comparison of different glass-forming liquids .....	8
Figure 2.2 Comparison of critical cooling rate with $T_{rg}$ in different glass system .....	9
Figure 2.3 Structural features of BMG systems .....	11
Figure 2.4 Metallic glass samples bended in superplastic region .....	16
Figure 2.5 Relationship between fracture strength and Young's modulus for metallic glasses and conventional materials .....	17
Figure 2.6 Relationship between Vickers hardness and Young's modulus for metallic glasses and conventional materials .....	18
Figure 2.7 Comparison of corrosion behavior of Fe-Co-Cr-Mo-Mn-C-B-Y BAS system with conventional steels .....	21
Figure 2.8 Image of arc melting device with suction casting unit .....	28
Figure 3.1 The samples produced by a) centrifugal casting b) suction casting .....	38
Figure 4.1 a) XRD b) DSC c) SEM analysis of centrifugally casted base alloy.....	44
Figure 4.2 Ellingham Diagram for carbide formation .....	45
Figure 4.3 XRD patterns of base alloy and elemental additions.....	47
Figure 4.4 DSC plots of base alloy and elemental additions .....	47
Figure 4.5 Hysteresis loops of base alloy and $M_{60}Cr_{13}Mo_{14}B_8Y_2X_3$ alloys.....	50
Figure 4.6 SEM micrographs $M_{60}Cr_{13}Mo_{14}B_8Y_2X_3$ alloy system taken from the 1.5 thickness of the wedge shape forms. These images belongs to a) X = Ti b) X = V c)X = Al and d) X = Mn.....	52
Figure 4.7 XRD diffractogrammes of suction casted $M_{60}Cr_{13}Mo_{17-x}B_8Y_2Al_x$ and $M_{60}Cr_{13}Mo_{17-x}B_8Y_2Mn_x$ alloys where x = 3, 6 and 9 individually.....	55

Figure 4.8 DSC thermogrammes of suction casted $M_{60}Cr_{13}Mo_{17-x}B_8Y_2Al_x$ and $M_{60}Cr_{13}Mo_{17-x}B_8Y_2Mn_x$ alloys where $x = 3, 6$ and $9$ individually .....	55
Figure 4.9 Hysteresis loops of $M_{60}Cr_{13}Mo_{17-x}B_8Y_2Al_x$ alloy systems .....	58
Figure 4.10 Hysteresis loops of $M_{60}Cr_{13}Mo_{17-x}B_8Y_2Mn_x$ alloy systems .....	58
Figure 4.11 SEM micrographs of produced BAS systems with compositions of a) $M_{60}Cr_{13}Mo_{11}B_8Y_2Al_6$ b) $M_{60}Cr_{13}Mo_8B_8Y_2Al_9$ c) $M_{60}Cr_{13}Mo_{11}B_8Y_2Mn_6$ d) $M_{60}Cr_{13}Mo_8B_8Y_2Mn_9$ at 8000 magnification.....	60
Figure 5.1 $M_{60}Cr_{13}Mo_{17-x}B_8Y_2Mn_x$ samples fabricated by suction casting .....	62
Figure 5.2 XRD diffractogrammes of the $M_{60}Cr_{13}Mo_{17-x}B_8Y_2Mn_x$ alloy system where $x$ varies from 0 to 10.....	63
Figure 5.3 Heating DSC thermogrammes of the $M_{60}Cr_{13}Mo_{17-x}B_8Y_2Mn_x$ alloy system where $x$ varies from 0 to 10.....	65
Figure 5.4 Magnified view of heating DSC thermogrammes of the $M_{60}Cr_{13}Mo_{17-x}B_8Y_2Mn_x$ alloy system where $x$ varies from 0 to 10. ....	66
Figure 5.5 First cycle of the cooling curves of the $M_{60}Cr_{13}Mo_{17-x}B_8Y_2Mn_x$ alloy system where $x$ varies from 0 to 10.....	67
Figure 5.6 Change of $T_g$ , $T_x$ and $\Delta T_x$ with Mn content of the base alloy.....	69
Figure 5.7 Hysteresis loops of the $M_{60}Cr_{13}Mo_{17-x}B_8Y_2Mn_x$ alloy system where $x$ varies from 0 to 10.....	72
Figure 5.8 Magnified view of the hysteresis loops of the $M_{60}Cr_{13}Mo_{17-x}B_8Y_2Mn_x$ alloy system where $x$ varies from 0 to 10.....	73
Figure 5.9 Variation of the $M_r$ , $M_s$ and the $S$ parameters with Mn content .....	74
Figure 5.10 XRD diffractogrammes of heat treated $M_{60}Cr_{13}Mo_{17}B_8Y_2$ (base alloy) and $M_{60}Cr_{13}Mo_{17-x}B_8Y_2Mn_x$ alloy systems where $x=3, 7, 10$ .....	75
Figure 5.11 Microstructural investigation of the heat treated base alloy system ( $M_{60}Cr_{13}Mo_{17}B_8Y_2$ ). a) SEM micrograph at 1000 magnification b) SEM micrograph	

at 4000 magnification c) EDS line scan zone of base alloy d) line scan results of the micrograph (c).....	77
Figure 5.12 EDS mapping observations of the base alloy a) Mapping micrograph of base alloy and results according to b) Fe, c) Cr, d) Mo, e) Si.....	78
Figure 5.13 Microstructural investigation of the heat treated 3at% Mn added system ( $M_{60}Cr_{13}Mo_{17}B_8Y_2Mn_3$ ). a) SEM micrograph at 1000 magnification b) SEM micrograph at 4000 magnification c) EDS line scan zone of base alloy d) line scan results of the micrograph (c). .....	79
Figure 5.14 EDS mapping observations of the system containing 3at.% Mn a)Mapping of base alloy and results according to b)Fe, c)Cr, d)Mo, e)Si.....	80
Figure 5.15 SEM micrographs of system containing 7 at.% Mn a) 1000 magnification b) 4000 magnification and system containing 10at.% Mn c) 1000 magnification d) 4000 magnification .....	81
Figure 5.16 Hardness distributions with respect to Mn content of the system of heat treated, as-cast and rapidly cooled specimens.....	83
Figure 5.17 DSC thermogrammes of heating rates of 5 K/min up to 99 K/min .....	87
Figure 5.18 DSC thermogrammes of heating rates of 5 K/min up to 40 K/min.....	88
Figure 5.19 Kissinger plot of $M_{60}Cr_{13}Mo_{10}B_8Y_2Mn_7$ bulk amorphous steel.....	89
Figure 5.20 Ozawa plot of $M_{60}Cr_{13}Mo_{10}B_8Y_2Mn_7$ bulk amorphous steel .....	90
Figure 5.21 Barandiaran-Colmenero plot of $M_{60}Cr_{13}Mo_{10}B_8Y_2Mn_7$ BAS .....	91
Figure 5.22 Barandiaran-Colmenero plot for eutectic suppression of BAS .....	92
Figure 5.23 Weight loss measurements of different samples in 0.5M $H_2SO_4$ .....	94
Figure 5.24 Weight loss measurements of different samples in 1M NaOH .....	95
Figure 5.25 Weight loss measurements of different samples in 1M NaOH .....	96
Figure 5.26 Comparison of hardness values of BAS with conventional materials...	97
Figure A.1 Example of $T_g$ calculation by SETARAM thermal analysis .....	115



## CHAPTER 1

### INTRODUCTION

From the beginning of the chalcolithic age, metals have had a significant importance in advance of technology. Since the natural structures of the metals are ordered symmetrical crystalline structure, many of the properties were completely understood and relations which explain these properties with structure were established. These repeating patterns of atoms are obtained by cooling molten metals with usual cooling rates. However, with advances in production technique in materials science, higher cooling rates can be achieved. For the first time, ordered atomic arrangements in Au-Si alloy system were prevented with one of the techniques which are applying high cooling rates ( $\approx 10^7$  K/s) and liquid-like metallic material was fabricated [1]. These materials with no atomic arrangements were defined as metallic glasses or amorphous alloys.

Discovery of amorphous alloys started a new era in material science. Numerous and synchronous researches contributed remarkably to this aspect [2-7]. Bulk metallic glasses (BMGs) which have thicknesses or diameters in millimeter scales were developed in 1982 [8, 9]. Among all classes of BMGs, Fe-based BMGs attracted attentions due to their extreme mechanical properties, corrosion and wear resistances with showing ferromagnetic behavior. Bulk amorphous steels (BASs) are also another division of those promising Fe-based BMGs [10]. The difference is that BASs behave as non-ferromagnetic. Since they are paramagnetic, the commercial areas diverged from medical to advanced structural purposes than conventional ferromagnetic Fe-based BMGs [11-13].

However, requirement of advanced production techniques with heavily controlled atmosphere such as melt spinning and suction casting and the necessity of using

highly pure constitution elements are obstructing adaptation of BMGs to the industry. These materials can only be used in highly special purposes due to their fabrication costs. Furthermore, the thermal characteristics and heat resistances had to be increased for higher temperature applications.

The first part of the study aims to design and synthesize BASs from scrap cast irons containing high carbon contents by conventional methods. By replacing the greater part of constituent elements with scrap and producing them with conventional centrifugal casting technique, expense of fabrication will be reduced via providing a waste management for cast irons. BASs systems containing 60at.% cast iron scraps, in other words major part of the composition, and pure constituent elements such as Mo, Cr, B and Y chosen in accordance with combining the knowledge of theoretical and experimental background in NOVALAB with published researches in literature, fabricated successfully with having high supercooled liquid region. Additionally, GFA of the samples tried to be increased by various elemental additions via substituting Mo in the system and manganese found to be the best among the others.

In the second part of the study, optimum Mn content in at least 3mm-diameter BAS samples tried to be found by micro-alloying technique for enhanced thermal and mechanical characteristics with the highest GFA. All samples were completely characterized by x-ray diffractions, thermal and magnetic analysis and microstructural investigations. Kinetic analyses were performed to obtain the critical parameters for mechanisms and suppression of the crystallization. Through all modifications and investigations, optimized Mn content specified as 7at.% which is one of the best thermally stable amorphous steel systems was developed along with lowering fabrication costs.

This study covers six chapters. A brief introduction about the study is presented in the first chapter. Theoretical background about bulk metallic glasses and bulk amorphous steels are given in the second chapter. In the third chapter, materials and the methods which were used to fabricate and enhance the properties of bulk amorphous steels are given. In the following chapter, results are given and discussions on these results are expounded about synthesis of bulk amorphous steels

in economical and conventional manner. The optimization results of Mn by the substitution of Mo are given in the fifth chapter. Finally, the essential and the fundamental points which were achieved during this study are summarized.



## CHAPTER 2

### THEORETICAL BACKGROUND

#### 2.1. Early Developments of Metallic Glasses

Since the beginning of pre-historic ages, metallic materials have been used in lots of different applications. After the industrial revolution, material science and processing technology has been developed rapidly. However, until 1960s metallic materials were only known as crystalline materials and glass term used to define the ceramic glasses. In 1960, Duwez et. al. [1] successfully bypassed the nucleation and growth steps of crystallization in Au-Si alloys by applying high cooling rates and synthesize the first metal with disordered structure which is defined as metallic glass or amorphous metals.

After this successful attempt, in 1970s and 1980s the researches about metallic glasses gained momentum due to their importance in fundamental science and potential engineering applications [2, 3, 14, 15]. Turnbull et. al. [3, 15] showed that metallic glasses and conventional glasses had some similarities in the thermal characteristic point of view. According to this study, metallic glasses also show glass transition temperature which is one of the crucial contributions in the field of metallic glass.

Until 1974, metallic glasses could only be produced in the size of microns. In 1974, Chen et. al. [16] succeeded to manufacture first millimeter sized metallic glass with Pd-Cu-Si ternary system with relatively lower cooling rates. These metallic glasses larger than millimeter scale were called bulk metallic glasses (BMGs). In the beginning of 1980s, Turnbull and coworkers produced almost a centimeter sized BMG from Pd-Ni-P ternary system with cooling rates as low as 10K/s [8, 9]. With

these exciting developments, BMGs emerged to be the new class of materials which is needed to be developed and investigated.

## 2.2. BMG Systems and Their Features

Metals were considered as crystalline materials until bypassing nucleation and crystallization step in 1960 with very high a cooling rate  $\sim 10^6\text{K/s}$  [1]. By skipping these steps, periodicity between atoms was vanished and amorphous alloys were introduced to the literature. However, not all alloy systems could produce BMGs. There are some limitations for suppressing the crystallization step.

### 2.2.1. Thermodynamic and Kinetic Aspects of Metallic Glasses

Thermodynamic is one of the most fundamental approaches to determine the relative stability of phases. So, with this point of view, one can simply determine the limitations of glass forming. The Gibbs free energy ( $\Delta G$ ) is the term which shows the stability of any phases.

$$\Delta G = \Delta H_{tr} - T\Delta S_{tr} \quad \text{and} \quad (\Delta G = G_{\text{glass}} - G_{\text{crystal}}) \quad (2.1)$$

where  $\Delta H_{tr}$  is enthalpy of transformation and  $\Delta S_{tr}$  is entropy of transformation

It is commonly acknowledged that the glass formation becomes more favorable as the Gibbs free energy becomes negative. In other words, to bypass the crystallization free energy of glass has to be lower than competing crystalline phase.

In accordance with the Eq. 2.1, it is obvious that the system becomes more stable when the lowest G value is obtained. In order to obtain negative  $\Delta G$ , either  $\Delta H_f$  term should be lowered or  $\Delta S_f$  term should be increased.

The entropy of the system represents the measure of different ways in which the constituent atoms can be arranged, when the case is metallic glasses with high

number of constituent elements, entropy term automatically increases because of the diversity of arrangement possibilities. Surely, the interactions between constituent atoms will also affect the enthalpy of formation. By increasing  $\Delta S_f$ , atoms will pack more randomly, which will lead the decrease of  $\Delta H_f$ . As a result, the solid/liquid interfacial energy will increase [17]. It is obvious that the production of multicomponent BMGs is much easier and requires lower cooling rates than binary alloy systems.

In the kinetics point of view, viscosity has an important influence on metallic glasses and glass forming capabilities. The alteration of viscosity of a liquid as a function of undercooling can be tool for categorizing and characterizing the liquids since it reveals the change of mobility of atom during supercooling [18]. Viscosity can be determined from Vogel-Fulcher-Tammann (VFT) relation [18]:

$$\eta = \eta_0 \exp \left[ \frac{DT_0}{T - T_0} \right] \quad (2.2)$$

where  $T_0$  is Vogel-Fulcher temperature and  $D$  is the fragility parameter.

Previous studies about metallic glasses [19] showed that the liquid which forms BMGs, behaves like/similar to the silicate melts kinetically.

In Fig.2.1 the viscosities of common non-metallic liquids were compared with metallic glasses.  $\text{SiO}_2$  shows the strongest glass formability with fragility parameter around 100 and high melt viscosity. In accordance with the plot, BMG forming liquids could be classified as strong liquids like silica glasses. The melt viscosities of the BMG former liquids have fragility parameters around 20.

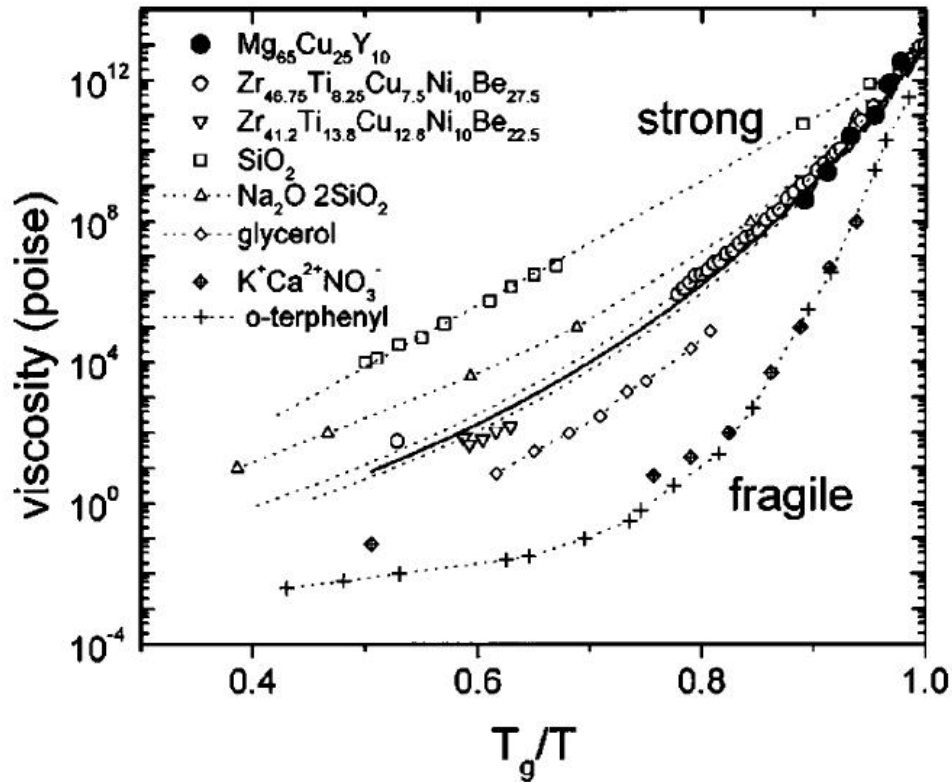


**Figure 2.1** Viscosity comparison of different glass-forming liquids [20]

### 2.2.2. Design of a BMG Alloy

Bulk term represents the systems having thicknesses or diameters in millimetric scale. So as to produce metallic glasses in bulk form, the required cooling rates should be lowered. In Fig. 2.2, cooling rate comparison of silicate glass, BMGs and conventional metallic glasses can be seen in relation with reduced glass transition temperature ( $T_{rg}$ ) which will be stated following sections of the thesis. The figure indicates that critical cooling rate for BMGs needs to be below  $10^4$  K/s. So, critical cooling rate should be the one of the considerations while designing BMG compositions.

In 1996, Inoue set the criteria for the BMG production by considering several multicomponent alloy systems [21]. These rules can be stated as:

- 1- The alloy system must contain at least three constituent elements.
- 2- Atomic radius of the constituent elements should be different.
- 3- Negative heats of mixing should be attained among major constituent elements of the alloy system

The first criterion is based on the thermodynamic and kinetic aspects of the glass formation. As it was discussed before, as the component number of the system is increased, entropy of the system is also increased while the enthalpy of the system is decreased which leads to decrease in the Gibbs free energy, consequently, creates an opportunity for glassy phase to compete the crystalline phases. Moreover, as the component number is increased, viscosity of the melt is also increased and forms a better glass former melt. By this way, both nucleation and growth rates are reduced.

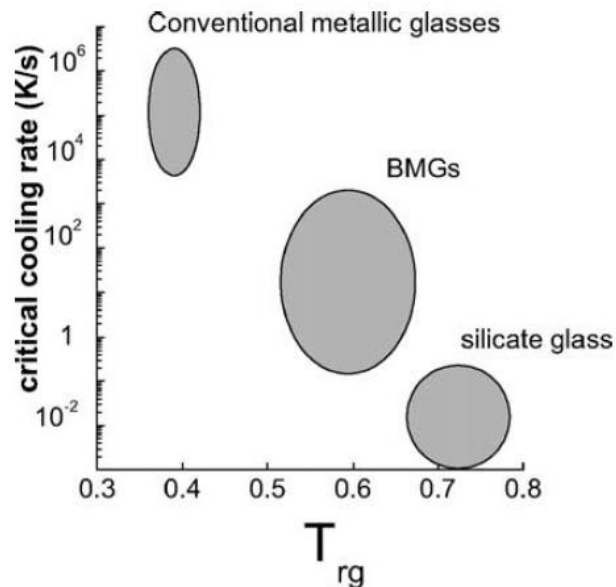


**Figure 2.2** Comparison of critical cooling rate with  $T_{rg}$  in different glass system [19]

Greer's confusion principle [22] is in an agreement with the second criterion. As it was stated in this principle, adding constituent elements with different atomic radius, system could not be able to choose a viable crystal structure which resulted in the increase in glass forming of the system. When this statement combined with the Inoue's second criteria, most feasible elements to stabilize the amorphous phase is the ones with diverge in atomic sizes.

Significant variations in atomic radius between the constituent elements and negative heat of mixing caused efficient packing of clusters and therefore the density of unsystematic packing of atoms in supercooled liquid state increased. As a result, the solid/liquid interfacial energy and viscosity of the system is increased with decrease in atomic diffusivity [17, 23, 24].

In addition to these criteria, the systems where deep eutectics are presented showed better glass forming. The main reason of this fact is the stability of the liquid at lower temperatures.

This is also verified by the solidification model proposed by Akdeniz [25]. According to this model, glass formability of the alloys was enhanced and amorphous structure could be achieved when composition involves peritectic reaction followed by eutectic reactions. As it was mentioned, the stability of the liquid was increased as the formation of the solid was delayed with these kinds of reactions.

### 2.2.3. Structures of BMG systems

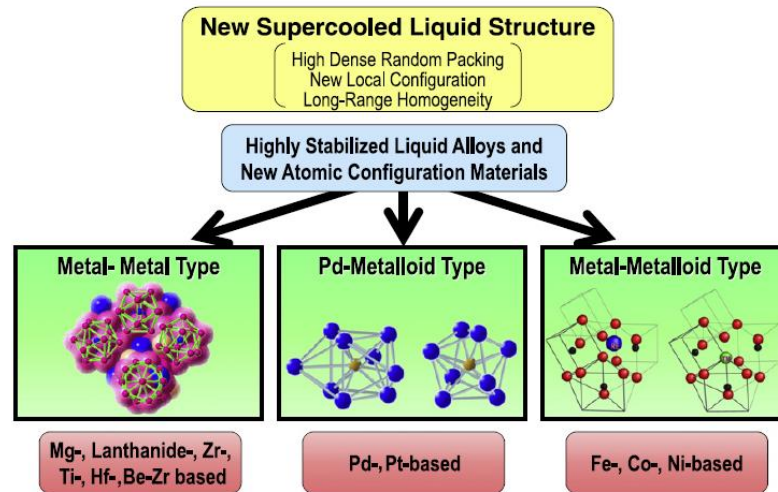


**Figure 2.3** Structural features of BMG systems [7]

There are 3 types of atomic arrangements of commonly used BMGs. The first one is the interaction between metal-metal types. The constituent atoms of BMGs arrange as icosahedral-like ordered structure [26]. Highly dense packed configurations of two types of polyhedral are commonly observed in Pd-based BMG systems. Finally, Fe, Co and Ni based BMGs have network-like atomic arrangements which can be presented as distorted trigonal prism and anti-Archimedean prism [7]. These complex arrangements of constituent atoms can prevent the long-range ordering of the system and consequently suppress the crystallization step of the system, which leads the formation of glassy phase.

In Table 2.1, different BMG systems and their years of discoveries are given. After the first BMG composition which is Pd-M-Si system, great research efforts had been given to enhancement of BMG systems and their properties.

**Table 2.1** Previously investigated non-ferrous BMG systems in literature are arranged according to the first paper of each alloy published

<b>Non-ferrous alloy systems</b>	<b>Year</b>
Pd-M-Si (M= Cu, Ag, Au, Fe, Co, Ni)	1974 [16]
Pt-Ni-P	1975 [27]
Au-Si-Ge	1975 [27]
Mg-Ln-M (Ln= Lanthanides, M= Fe, Co, Ni, Cu)	1988 [28]
Al-Ce-M (M= Nb, Co, Fe, Ni, Cu)	1988 [29]
Ln-Al-TM (TM= Fe, Co, Ni, Cu)	1989 [30]
Ln-Ga-TM	1989 [30]
Zr-Al-TM	1991 [5]
Ti-Zr-TM	1993 [6]
Zr-Ti-TM-Be	1993 [31]
Co-(Al,Ga)-(P, B, Si)	1995 [10]
Pd-Cu-Ni-P	1996 [32]
Ti-Ni-Cu-Sn	1998 [6]
Pd-Ni-Fe-P	1999 [33]
Ca-Cu-Ag-Mg	2000 [7]
Cu-Zr, Cu-Hf	2001 [34]
Cu-(Zr, Hf)-Al	2003 [35]
Y-Sc-Al-Co	2003 [36]
Pt-Cu-Ni-P	2004 [37]
Au-Ag-Pd-Cu-Si	2005 [38]
Pd-Pt-Cu-P	2007 [7]
Ti-Zr-Cu-Pd	2007 [7]

### 2.3. Fe-Based BMGs

Since the first fabrication of Fe-based bulk metallic glasses was achieved by Fe-Ga-Al-P-B-C alloy system [10], these BMGs attracted attention due to their relatively

low costs when it is compared with the other BMG classes, extreme mechanical properties, excellent magnetic properties and high corrosion and wear resistances. Since Fe-based BMGs have unique properties when they are compared to the crystalline counterparts and seem to be more likely to be commercialized than other the BMG systems, numerous studies had been done to enhance these properties. In Table 2.2, the Fe-based BMG alloys are given with respect to the date that system was firstly published. In accordance with the table, since binary Fe-based systems require very high cooling rates around  $10^6$ - $10^8$ K/s, these alloys contain 3 or more constituent elements to produce metallic glasses in bulk form. Via alloying more constituent elements, critical cooling rates of the mentioned systems were reduced to  $\sim 10$ - $10^2$ K/s.

**Table 2.2** Previously investigated ferrous BMG systems in literature arranged according to first paper of each alloy published

<b>Ferrous alloy systems</b>	<b>Year</b>
Fe-(Al, Ga)-(P, C, B, Si, Ge)	1995 [10]
Fe-(Nb, Mo)-(Al, Ga)-(P, B, Si)	1995 [6]
Fe-(Zr, Hf, Nb)-B	1996 [39]
Fe-Co-Ln-B	1998 [40]
Fe-Ga-(Cr, Mo)-(P, C, B)	1999 [41]
Fe-Co-Ta-B	1999 [42]
Fe-Ga-(P, B)	2000
Fe-Si-B-Nb	2002
Fe-Mn-Mo-Cr-B-C	2002 [43]
Fe-Co-Si-B-Nb	2002
Fe-(Cr, Mo)-(C, B)	2003 [11]
Co-Fe-Ta-B-Si	2003
Fe-(Cr,Mo)-(C,B)-Ln (Ln= Y, Er, Tm)	2004 [44]
Fe-(Nb, Cr)-(P, B, Si)	2010

### **2.3.1. Properties of Fe-Based BMGs**

Since metallic glasses are in amorphous form and lack of atomic order, they do not contain microstructural features such as grain boundaries. This random arrangement of atoms gives metallic glasses extreme properties. Fe-based systems are one of the most important classes of BMGs and they show unique properties than the other systems. In the following section these properties such as magnetic, mechanical, thermal and corrosion will be given.

#### **2.3.1.1. Magnetic Properties**

After the production of the first ferromagnetic BMGs (Fe-Si-B and Fe-C-P) by copper mold casting, lots of attention was given to the investigation of the magnetic behavior of these systems. Alloys showed different magnetic behavior according to their compositions.

Firstly, hard magnetic properties were obtained from Fe-Nd-B systems by annealing amorphous precursors. Due to their Nd-Fe clusters in the structure which produce very high magnetic anisotropy, high coercivity was obtained. These kinds of magnets are available in industry and presumed to be one of the best hard magnets in the industry. Moreover hard magnetic behavior was detected in Nd-Al-Fe systems; however, these results were only achieved in the bulk forms. The desired coercivities could be obtained by changing the diameter of these systems [45-47].

Secondly, Fe-based BMGs generally behave as soft magnetic materials. Until now, countless soft magnetic Fe-based BMG compositions were investigated such as Fe-Al-Ga-P-C-B, Fe-P-B-Si, Fe-Co-Ni-Zr-B, Fe-Co-B-Si-Nb, etc. They showed excellent magnetic properties as soft magnets with high saturation magnetization between 0.75 to 1.5T, low coercivity between 1 to 12A/m and high magnetic permeability between 900 to 1200 [10, 48-50]. The effect of annealing on soft magnetic properties had been also investigated. Upon annealing, controlled

formation of nanocrystals which are mainly  $\alpha$ -(Fe, Co), soft magnetic properties of these alloy systems increased heavily.

Finally, relatively new concept which is Fe-based metallic glasses with non-ferromagnetic properties was introduced to the literature. These Fe-based BMGs were defined as bulk amorphous steels (BASs). Mainly, magnetic transition temperatures (Curie temperatures) of these materials are below room temperature so they behave as non-ferromagnetic materials at room temperature [43]. Addition of alloying elements like Cr and Mn help to suppress the magnetic effect by lowering the Curie temperature.

### **2.3.1.2. Mechanical Properties**

Another important aspect that makes Fe-based BMGs charming is their extreme mechanical properties. However, before examining Fe-based BMGs mechanical properties in detail, the deformation mechanisms of BMGs should be considered. BMGs showed 2 completely different deformation mechanisms below and above their glass transition temperatures ( $T_g$ ):

- 1- Non-uniform deformation
- 2- Uniform deformation

#### **2.3.1.2.1. Non-Uniform Deformation of BMGs**

This kind of deformation can be seen below  $T_g$ . Inhomogeneous deformation can be observed by shear bands formation, rapid propagation and finally catastrophic fracture of the sample. These shear bands are formed on planes where maximum resolved shear stress obtained and most of the plastic strain is localized. In contrast to their crystalline counterparts, BMGs show strain softening which can be interpreted as material become softer as the strain was increased. The formation of the shear bands are the direct reasons of the strain softening. Although the whole mechanism behind these phenomena is still unclear, there are some hypotheses

about this kind of deformation. The first one suggests that during deformation, owing to the formation of free volume, viscosity is reduced in the shear bands [51-53]. According to the second approach, the viscosity of the metallic glass is dropped due to the local adiabatic heating in the shear bands [54-56].

### 2.3.1.2.2. Uniform Deformation of BMGs

Homogeneous deformation can be seen at high temperatures (above  $T_g$ ). Upon heating, between the glass transition and the crystallization step, metallic glasses behave as supercooled liquids. In this range, metallic glasses show superplastic behavior due to Newtonian-flow behavior. This is one of the most important properties of metallic glasses. Large tensile elongations up to  $\sim 10^4\%$  can be obtained within this range [57-60].

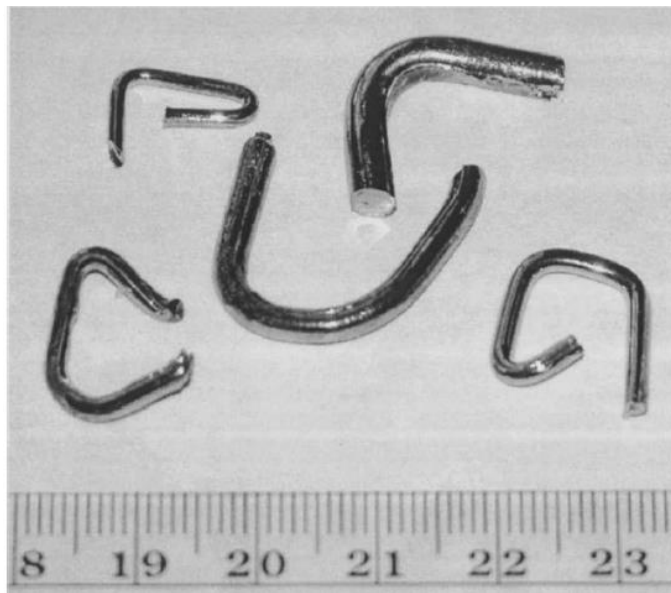


**Figure 2.4** Metallic glass samples bent into different shapes in superplastic region

### 2.3.1.2.3. Mechanical Properties of Fe-Based BMGs

Fe-based BMGs exhibit very high fracture strengths. Figure 2.5 shows that Fe-based BMGs have fracture strengths between 3000 to 4000MPa which is 3-4 times higher values than their crystalline counterparts.

There are various studies about the mechanical properties of BASs. Gu et. al. [61] showed the effect of metalloids on Fe-Cr-Mo-P-C-B system and found that the fracture strength was around 3.5GPa. Another study of the same group [62] revealed that as Er introduced to the Fe-Mo-C-B BAS system, fracture strength was increased from 3.8GPa to 4.2GPa while plastic strain was decreased from 0.6% to 0%. Moreover, according to the same study, addition of Cr had augmenting effect on fracture strength. Shiflet et. al. [63] investigated the effect of C content on strength of Fe-Cr-Mo-C-B-Ln (Ln= Lanthanides) BASs by keeping metalloid content stable. They found that as C on the system increased, strength showed almost no change; however, due to the change in interactions between metal-metal bonding, bulk modulus of this system is lowered. Another similar study about Fe-Cr-Co-Mo-B-C-Y system by Lu et. al [13] showed fracture strength of material as 3GPa. To sum up, BASs fracture strength varies from around 3 to 4GPa like rest of Fe-based BMGs.

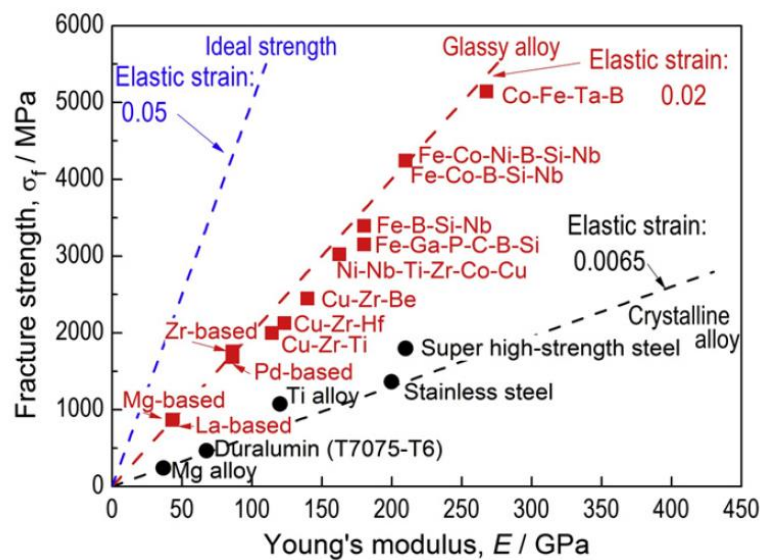


**Figure 2.5** Relationship between fracture strength and Young's modulus for metallic glasses and conventional materials [6]

Another important mechanical characteristic of the Fe-based BMGs is their high hardness. In relation to Fig. 2.6, Fe-based BMGs show hardness values between 900 to 1300HV. These values are almost 10 times higher than conventional steels and almost 5 times higher than stainless steels.

The Vickers hardness of amorphous steel alloys varies almost in same range of Fe-based metallic glasses. Iqbal et. al. [64] found Vickers hardness values between 1200-1280Hv for the system Fe-Cr-Mo-C-B-Y. Lu et. al. [13] showed that Fe-Co-Cr-Mo-C-B-Mn-Y system reached values around 1250HV. Another study belongs to Hess [65] revealed the Vickers hardness of Fe-Cr-C-Mo-B-Er amorphous steels were in the range of 960 to 1150HV. In addition, the study which amorphous steel alloys were produced from low-purity materials by Tsai [66] found hardness values around 1200HV.

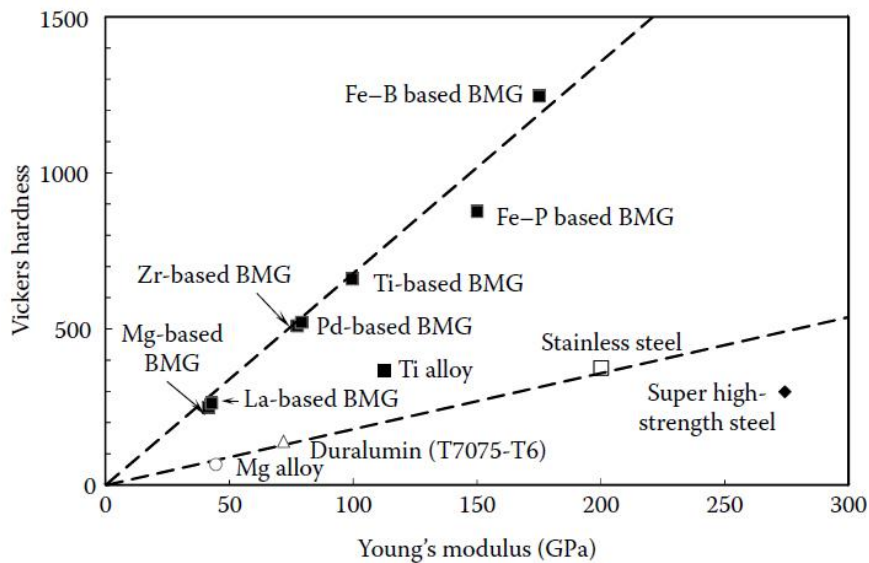


**Figure 2.6** Relationship between Vickers hardness and Young's modulus for metallic glasses and conventional materials [6]

### 2.3.1.3. Thermal Properties of Fe-Based BMGs

When the thermal parameters of BMGs are discussed, one should consider glass transition temperature ( $T_g$ ), crystallization temperature ( $T_x$ ), supercooled liquid region ( $\Delta T_x$ ) and liquidus temperature ( $T_l$ ).  $T_g$  and  $\Delta T_x$  values directly affect the thermal stability of BMGs. In this point of view, high  $T_g$  and wider  $\Delta T_x$  means, BMG will lose its amorphous nature at elevated temperatures and the supercooled liquid in the system will be more stable. This fact shows the importance of Fe-based BMGs. Fe-based BMGs have high  $T_g$  with relatively wide  $\Delta T_x$ . Table 2.3 shows, most of the alloy systems in the literature.

**Table 2.3** Summary of the Fe-based BMG systems in the literature with their glass transition temperature ( $T_g$ ), crystallization temperature ( $T_x$ ), supercooled liquid region ( $\Delta T_x$ ) and the years alloys are first published.

Alloy	$T_g$ (K)	$T_x$ (K)	$\Delta T_x$ (K)	Year
Fe <sub>75</sub> Al <sub>5</sub> Ga <sub>2</sub> P <sub>11</sub> C <sub>5</sub> B <sub>4</sub>	732	785	53	1995 [10]
Nd <sub>60</sub> Fe <sub>30</sub> Al <sub>10</sub>	NA	866	NA	1996 [46]
Fe <sub>60co</sub> Co <sub>3</sub> Ni <sub>7</sub> Zr <sub>10</sub> B <sub>20</sub>	810	870	60	1997 [39]
Fe <sub>46</sub> Co <sub>17</sub> Ni <sub>7</sub> Zr <sub>10</sub> B <sub>20</sub>	840	905	65	1997 [39]
Fe <sub>62</sub> Co <sub>7</sub> Hf <sub>4</sub> B <sub>20</sub>	800	840	40	1999 [42]
Fe <sub>58</sub> Co <sub>7</sub> Hf <sub>8</sub> B <sub>20</sub>	830	890	60	1999 [42]
Fe <sub>56</sub> Co <sub>7</sub> Hf <sub>10</sub> B <sub>20</sub>	835	910	75	1999 [42]
Fe <sub>54</sub> Co <sub>7</sub> Hf <sub>12</sub> B <sub>20</sub>	880	960	80	1999 [42]
Fe <sub>71</sub> Cr <sub>4</sub> Mo <sub>4</sub> P <sub>11</sub> B <sub>5</sub> C <sub>5</sub>	718	753	35	1999 [41]
Fe <sub>67</sub> Cr <sub>4</sub> Mo <sub>4</sub> Ga <sub>4</sub> P <sub>11</sub> B <sub>5</sub> C <sub>5</sub>	730	785	56	1999 [41]
Fe <sub>62</sub> Co <sub>5</sub> Cr <sub>4</sub> Mo <sub>4</sub> Ga <sub>4</sub> P <sub>11</sub> B <sub>5</sub> C <sub>5</sub>	731	786	55	1999 [41]
Fe <sub>65</sub> Sb <sub>2</sub> Cr <sub>4</sub> Mo <sub>4</sub> Ga <sub>4</sub> P <sub>11</sub> B <sub>5</sub> C <sub>5</sub>	719	775	56	1999 [41]
Fe <sub>65</sub> Co <sub>10</sub> Sm <sub>5</sub> B <sub>20</sub>	858	884	26	1999 [67]
Fe <sub>60</sub> Co <sub>10</sub> Sm <sub>10</sub> B <sub>20</sub>	NA	964	NA	1999 [67]
Fe <sub>55</sub> Co <sub>20</sub> Sm <sub>5</sub> B <sub>20</sub>	843	864	21	1999 [67]

**Table 2.3 (Continued)**

Fe <sub>76</sub> Sm <sub>4</sub> B <sub>20</sub>	805	824	19	1999 [67]
Fe <sub>58</sub> Co <sub>7</sub> Ni <sub>7</sub> Zr <sub>8</sub> B <sub>20</sub>	821	899	78	1999 [68]
Fe <sub>52</sub> Co <sub>10</sub> Nb <sub>8</sub> B <sub>30</sub>	907	994	87	1999 [68]
Fe <sub>40</sub> Ni <sub>40</sub> P <sub>14</sub> B <sub>6</sub>	640	683	43	2001 [50]
Fe <sub>45</sub> Cr <sub>16</sub> Mo <sub>16</sub> C <sub>18</sub> B <sub>5</sub>	856	914	58	2001 [69]
Fe <sub>45</sub> Cr <sub>16</sub> Mo <sub>14</sub> Ta <sub>2</sub> C <sub>18</sub> B <sub>5</sub>	853	906	53	2001 [69]
Fe <sub>45</sub> Cr <sub>16</sub> Mo <sub>14</sub> Nb <sub>2</sub> C <sub>18</sub> B <sub>5</sub>	852	903	51	2001 [69]
Fe <sub>43</sub> Cr <sub>16</sub> Mo <sub>16</sub> C <sub>15</sub> B <sub>10</sub>	870	860	90	2002 [70]
Fe <sub>43</sub> Cr <sub>16</sub> Mo <sub>16</sub> C <sub>10</sub> B <sub>5</sub> P <sub>10</sub>	860	930	70	2002 [70]
Fe <sub>43</sub> Cr <sub>16</sub> Mo <sub>16</sub> C <sub>10</sub> P <sub>15</sub>	880	910	30	2002 [70]
(Fe <sub>0.75</sub> B <sub>0.15</sub> Si <sub>0.1</sub> ) <sub>96</sub> Nb <sub>4</sub>	835	885	50	2003 [71]
Fe <sub>48</sub> Cr <sub>15</sub> Mo <sub>14</sub> Y <sub>2</sub>	839	886	47	2005 [72]
Fe <sub>39</sub> Co <sub>9</sub> Cr <sub>15</sub> Mo <sub>14</sub> Y <sub>2</sub>	838	888	50	2005 [72]
Fe <sub>65</sub> Mo <sub>14</sub> C <sub>15</sub> B <sub>6</sub>	789	843	54	2007 [61]
Fe <sub>61</sub> Cr <sub>6</sub> Mo <sub>14</sub> C <sub>15</sub> B <sub>6</sub>	806	858	52	2007 [61]
Fe <sub>50</sub> Cr <sub>15</sub> Mo <sub>14</sub> C <sub>15</sub> B <sub>6</sub>	839	874	45	2007 [61]

As stated by Table 2.3, the glass transition temperatures of Fe-based BMGs vary from 640 to 900K where supercooled liquid regions of the same systems change between 20 and 90K. Wide supercooled liquid region creates an opportunity to form different shapes, even nanowires, due to the superplastic behavior of the Newtonian supercooled liquid. Higher  $T_g$  means higher GFA (see section 2.5), and low cooling rate necessity. As critical cooling rates of Fe-based BMGs are reduced, the production methods become easier, cheaper and more conventional therefore, they can be easily adapted to the industry.

#### 2.3.1.4. Corrosion Properties of Fe-Based BMGs

Clearly, defect-free structures (grain boundaries, dislocations, etc.) of metallic glasses prevent corrosive environments to interact with the material in contrast to the crystalline materials. Therefore, it is a well-known fact that BMGs have high corrosion resistance. Furthermore, among BMG systems, Co and Fe based metallic glasses are determined as having the best resistance to corrosion. Adding Cr and Mo as alloying elements to the alloy system, results in stabilization of the passive region. Another important fact about corrosion resistances of BMGs is that as the temperature of the system is increased, the resistance to corrosion is decreased due to structural relaxation, which causes ordering in the system.

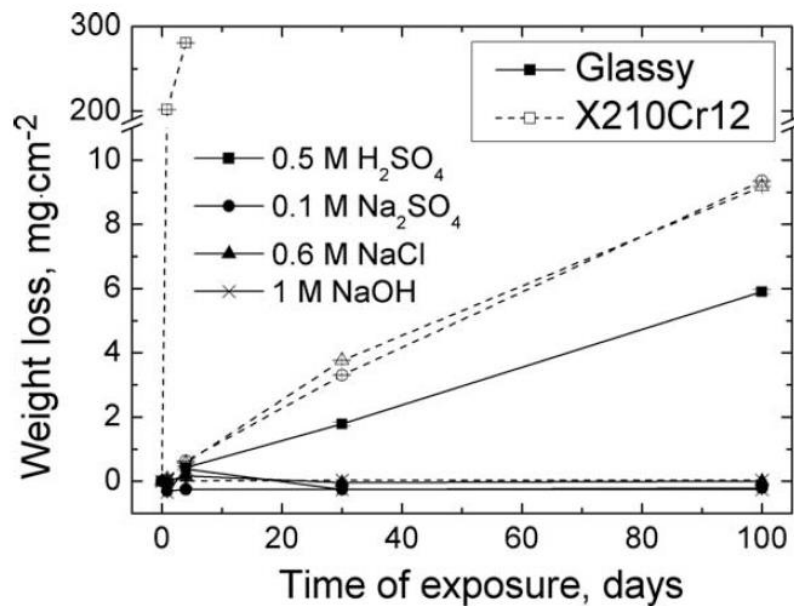


**Figure 2.7** Comparison of corrosion behavior of Fe-Co-Cr-Mo-Mn-C-B-Y BAS system with conventional steels [73]

Figure 2.7 shows the behavior of amorphous steels and their crystalline counterparts in different extreme environment conditions. It is obvious that, while materials which have crystalline structures had terrible performance, amorphous steels had

tremendous corrosion resistances. Only  $5\text{mg}/\text{cm}^2$  weight loss was observed in the concentrated  $\text{H}_2\text{SO}_4$  solution while in the other solutions weight of the system remained almost constant in 100 days [73].

Wang et. al. [74] investigated the effect of Y microalloying on corrosion resistance of the BASs and they concluded that in  $\text{Fe}_{50-x}\text{Cr}_{15}\text{Mo}_{14}\text{C}_{15}\text{Y}_2$  system, specimen showed instability for Y content below 1at.%; however, for samples which contained Y above 1at.%, they observed more stable behavior to polarized potential. Fang et. al. [75] examined the effect of Mn on corrosion properties and found that with increasing Mn content of the system resistance to corrode to HCL solution was significantly increased. Moreover, when BASs applied as coatings they showed superior corrosion resistance compared to the uncoated material. Fe-Cr-Mn-Mo-W-B-C-Si system was coated on AISI 316L and typical AISI 316. BAS coated samples showed superior passive film stability than AISI 316SS. Coated materials also showed low corrosion rates, as low as 100microns/year, than uncoated materials [76, 77].  $\text{Fe}_{41}\text{Cr}_{15}\text{Mo}_{14}\text{C}_{12}\text{B}_9\text{Y}_2\text{Co}_7$  system produced from low purity materials compared with AISI 304 and AISI 316 in Hank's balanced salt solution. BAS samples showed wider passive region and no pitting in experiments [66].

## **2.4. Bulk Amorphous Steels**

In 2002-2003, Shiflet et. al. [11, 43] synthesized a paramagnetic Fe-based BMG with using metalloids as C and B and defined this Fe-based BMGs as bulk amorphous steels. It was mentioned in the previous parts of the section that these prominent materials have high corrosion resistance, high fracture strength and high  $T_g$ . They are one of the most promising candidates among Fe-based BMGS which could be adapted to the industry and used in numerous applications due to their superior properties.

### 2.4.1. Previous Studies

Mechanical properties and resistance to corrosion were mentioned in the sections before. Normally, their glass forming abilities are lower than Pd- or Cu-based BMGs. However, with the increase in constituent elements in the system, their GFAs are now comparable with these BMG classes. But, due to lots of pure and rare constituent elements, the costs of BASs are high to use commercially. Moreover, increasing GFA means, necessary of reducing the cooling rate to produce fully amorphous structure, this will lead to fabricate BASs by conventional industrial methods. Although most of the previous studies about BASs focused on the increase of the GFA, less study had been done to lower the production cost.

Table 2.4 summarizes most of the studies about BAS. The obtained critical thermal properties and the thicknesses of the synthesized BASs systems can be found.

**Table 2.4** BAS systems and their critical thermal parameters

<b>Alloy</b>	<b>D (mm)</b>	<b>T<sub>g</sub> (K)</b>	<b>T<sub>x</sub> (K)</b>	<b>T<sub>l</sub> (K)</b>	<b>ΔT<sub>x</sub> (K)</b>	<b>Year</b>
Fe <sub>50</sub> Mn <sub>10</sub> Mo <sub>14</sub> Cr <sub>4</sub> C <sub>15</sub> B <sub>6</sub>	3					2002
Fe <sub>49</sub> Mn <sub>10</sub> Mo <sub>14</sub> Cr <sub>4</sub> W <sub>1</sub> C <sub>15</sub> B <sub>6</sub>	3	803	848	1353	45	2003
Fe <sub>48</sub> Mn <sub>10</sub> Mo <sub>13</sub> Cr <sub>4</sub> W <sub>2</sub> C <sub>15</sub> B <sub>6</sub>	2	to	to	to	to	[11,
Fe <sub>49</sub> Mn <sub>10</sub> Mo <sub>16</sub> Cr <sub>4</sub> Ga <sub>2</sub> C <sub>15</sub> B <sub>6</sub>	2	823	878	1363	55	43]
Fe <sub>49</sub> Mn <sub>10</sub> Mo <sub>14</sub> Cr <sub>4</sub> V <sub>1</sub> C <sub>15</sub> B <sub>6</sub>	3					
Fe <sub>53</sub> Mn <sub>10</sub> Cr <sub>4</sub> Mo <sub>12</sub> C <sub>15</sub> B <sub>6</sub>	3	803		1403		
Fe <sub>51</sub> Mn <sub>10</sub> Cr <sub>4</sub> Mo <sub>12</sub> Y <sub>2</sub> C <sub>15</sub> B <sub>6</sub>	6.5	803		1393		
Fe <sub>51</sub> Mn <sub>10</sub> Cr <sub>4</sub> Mo <sub>12</sub> Er <sub>2</sub> C <sub>15</sub> B <sub>6</sub>	7	813		1398		
Fe <sub>51</sub> Mn <sub>10</sub> Cr <sub>4</sub> Mo <sub>12</sub> Yb <sub>2</sub> C <sub>15</sub> B <sub>6</sub>	6.5	813	NA*	1403	NA*	2004
Fe <sub>51</sub> Mn <sub>10</sub> Cr <sub>4</sub> Mo <sub>12</sub> Gd <sub>2</sub> C <sub>15</sub> B <sub>6</sub>	6.5	813		1403		[44]
Fe <sub>51</sub> Mn <sub>10</sub> Cr <sub>4</sub> Mo <sub>12</sub> Dy <sub>2</sub> C <sub>15</sub> B <sub>6</sub>	6.5	808		1398		
Fe <sub>50</sub> Mn <sub>7</sub> Cr <sub>10</sub> Mo <sub>10</sub> Yb <sub>2</sub> C <sub>15</sub> B <sub>6</sub>	5	833		1413		

**Table 2.4 (Continued)**

(Fe <sub>44.3</sub> Cr <sub>5</sub> Co <sub>5</sub> Mo <sub>12.8</sub> Mn <sub>11.2</sub> C <sub>15.8</sub> B <sub>5.9</sub> ) <sub>98.5</sub> Y <sub>1.5</sub>	12	804	NA *	1491	NA *	2004
(Fe <sub>44.3</sub> Cr <sub>10</sub> Mo <sub>12.8</sub> Mn <sub>11.2</sub> C <sub>15.8</sub> B <sub>5.9</sub> ) <sub>98.5</sub> Y <sub>1.5</sub>	12	835		1439		[13]
Fe <sub>44</sub> Mn <sub>11</sub> Cr <sub>10</sub> Mo <sub>13</sub> C <sub>15</sub> B <sub>6</sub> Ho <sub>2</sub> (open to air)	8	837	870	1426	33	2005 [78]
Fe <sub>70.8</sub> C <sub>7</sub> Si <sub>3.5</sub> B <sub>3</sub> P <sub>9.6</sub> Cr <sub>2.1</sub> Mo <sub>2</sub> Al <sub>2</sub>	3	774	796	1292	22	2006
Fe <sub>64.8</sub> C <sub>7</sub> Si <sub>3.5</sub> B <sub>9</sub> P <sub>9.6</sub> Cr <sub>2.1</sub> Mo <sub>2</sub> Al <sub>2</sub>	1	817	855	1323	38	[79]
Fe <sub>65</sub> Mo <sub>14</sub> C <sub>15</sub> B <sub>6</sub>	1.5	789	843	1418	54	
Fe <sub>64</sub> Mo <sub>14</sub> C <sub>15</sub> B <sub>6</sub> Er <sub>1</sub>	3.5	783	832	1413	49	
Fe <sub>64</sub> Mo <sub>14</sub> C <sub>15</sub> B <sub>6</sub> Dy <sub>1</sub>	3	785	835	1408	50	2006
Fe <sub>63</sub> Mo <sub>14</sub> C <sub>15</sub> B <sub>6</sub> Er <sub>2</sub>	3	777	819	1423	42	[80]
Fe <sub>63</sub> Mo <sub>14</sub> C <sub>15</sub> B <sub>6</sub> Dy <sub>2</sub>	3	777	817	1418	40	
Fe <sub>48</sub> Cr <sub>15</sub> Mo <sub>14</sub> C <sub>15</sub> B <sub>6</sub> Er <sub>2</sub>	12	843	883	1443	40	2006 [61]
Fe <sub>43.7</sub> Co <sub>7.3</sub> Cr <sub>14.7</sub> Mo <sub>12.6</sub> C <sub>15.5</sub> B <sub>4.3</sub> Y <sub>1.9</sub> (low purity – open to air)	10	830	875	1438	45	2007 [81]
Fe <sub>52</sub> Mn <sub>2</sub> Cr <sub>19</sub> Mo <sub>2.5</sub> W <sub>1.7</sub> B <sub>16</sub> C <sub>4</sub> Si <sub>2.5</sub>						2007
Fe <sub>49.7</sub> Mn <sub>1.9</sub> Cr <sub>17.7</sub> Mo <sub>7.4</sub> W <sub>1.6</sub> B <sub>15.2</sub> C <sub>3.8</sub> Si <sub>2.4</sub>	C**	841	896	1611	55	[76,
		852	901	1463	49	77]
Fe <sub>71</sub> Mo <sub>5</sub> P <sub>12</sub> C <sub>10</sub> B <sub>2</sub>	3	701	733	1257	32	
Fe <sub>69</sub> Mo <sub>7</sub> P <sub>12</sub> C <sub>10</sub> B <sub>2</sub>	2.5	716	753	1263	37	
Fe <sub>69</sub> Cr <sub>2</sub> Mo <sub>5</sub> P <sub>12</sub> C <sub>10</sub> B <sub>2</sub>	3	710	744	1266	34	2007
Fe <sub>65</sub> Cr <sub>2</sub> Mo <sub>9</sub> P <sub>10</sub> C <sub>8</sub> B <sub>6</sub>	2.5	756	820	1288	64	[82]
Fe <sub>64</sub> Cr <sub>3</sub> Mo <sub>10</sub> P <sub>10</sub> C <sub>10</sub> B <sub>3</sub>	2.5	729	775	1288	46	
Fe <sub>68</sub> Cr <sub>3</sub> Mo <sub>10</sub> P <sub>10</sub> C <sub>7</sub> B <sub>2</sub>	2.5	735	778	1277	43	
Fe <sub>49</sub> Cr <sub>15</sub> Mo <sub>14</sub> C <sub>13</sub> B <sub>8</sub> Er <sub>1</sub>	4	861	914	1468	53	
Fe <sub>49</sub> Cr <sub>15</sub> Mo <sub>14</sub> C <sub>15</sub> B <sub>6</sub> Er <sub>1</sub>	6	857	901	1463	44	2007
Fe <sub>49</sub> Cr <sub>15</sub> Mo <sub>14</sub> C <sub>17</sub> B <sub>4</sub> Er <sub>1</sub>	4	849	891	1463	42	[63]
Fe <sub>44</sub> Cr <sub>10</sub> Mo <sub>12.5</sub> Mn <sub>11</sub> C <sub>15</sub> B <sub>6</sub> Y <sub>1.5</sub>	5	866	919	NA	53	2007 [75]

**Table 2.4 (Continued)**

$\text{Fe}_{68}\text{Cr}_3\text{Mo}_{10}\text{P}_6\text{C}_{10}\text{B}_3$	2	714	764		50	
$\text{Fe}_{66}\text{Cr}_3\text{Mo}_{10}\text{P}_8\text{C}_{10}\text{B}_3$	2	721	769		48	
$\text{Fe}_{64}\text{Cr}_3\text{Mo}_{10}\text{P}_{10}\text{C}_{10}\text{B}_3$	2	729	775		46	
$\text{Fe}_{62}\text{Cr}_3\text{Mo}_{10}\text{P}_{12}\text{C}_{10}\text{B}_3$	2	744	793	NA	49	2008
$\text{Fe}_{60}\text{Cr}_3\text{Mo}_{10}\text{P}_{14}\text{C}_{10}\text{B}_3$	2	775	836		61	[62]
$\text{Fe}_{63}\text{Cr}_3\text{Mo}_{10}\text{P}_{12}\text{C}_{10}\text{B}_2$	2	735	778		43	
$\text{Fe}_{63}\text{Cr}_3\text{Mo}_{10}\text{P}_{12}\text{C}_9\text{B}_3$	2	739	783		44	
$\text{Fe}_{63}\text{Cr}_3\text{Mo}_{10}\text{P}_{12}\text{C}_8\text{B}_4$	2	745	793		48	
$\text{Fe}_{74.5}\text{Mo}_{5.5}\text{P}_{12.5}\text{C}_5\text{B}_{2.5}$	3	702	728		26	2009 [83]
$\text{Fe}_{70}\text{Mo}_5\text{Ni}_5\text{P}_{12.5}\text{C}_5\text{B}_{2.5}$	4	696	733	NA	37	
$\text{Fe}_{68}\text{Mo}_5\text{Ni}_5\text{Cr}_2\text{P}_{12.5}\text{C}_5\text{B}_{2.5}$	6	699	743		44	
$\text{Fe}_{41}\text{Cr}_{15}\text{Co}_7\text{Mo}_{14}\text{C}_{16}\text{B}_5\text{Y}_2$	4	795	851	1483	56	
$\text{Fe}_{41}\text{Cr}_{15}\text{Co}_7\text{Mo}_{14}\text{C}_{13}\text{B}_8\text{Y}_2$	4	836	886	1488	50	2013 [66]
$\text{Fe}_{41}\text{Cr}_{15}\text{Co}_7\text{Mo}_{14}\text{C}_{11}\text{B}_{10}\text{Y}_2$	4	823	893	1436	70	
(Low purity industrial raw materials)						
*NA: Not Available      **C: Coating						

### 2.4.2. Effects of Alloying Elements

In order to design an amorphous steel alloy, the effects of alloying elements should be noted. Elemental additions on the desired properties can be summed as below:

- Fe, Zr, Ti and rare earth (RE) elements have large negative heats of mixing when alloyed with metalloids such as C, B and Si [84].
- Additions of metalloids to the BAS system and RE elements increase the GFA because of their large atomic size mismatches which increase the confusion of the structure. Additions of metalloids also decrease the liquidus temperature of the system and increase the  $T_{rg}$  of the system [11]. However, the elemental addition of RE should be optimized. For instance, Y should be

added in between 1at.% and 6at.%, otherwise crystalline product is stabilized rather than glassy phase [13, 85].

- Increase in  $T_g$  can be obtained by adding refractory metals such as Zr, Nb, Mo. Adding these refractory metals, form backbone structure with metalloids in the system which will increase the viscosity of the melt as well as the stability of the amorphous structure [11]. High  $T_g$  also means, higher temperature resistance and better GFA.
- Oxygen has a detrimental effect on amorphous alloys. It is unfavorable for GFA and it can trigger nucleation [86].
- Amorphous steels are paramagnetic Fe-based BMGs. So, one should consider the effects of alloying elements on magnetic properties while designing BAS system. When Ni is alloyed with the system, it is known that soft magnetic properties of the system are enhanced [87]. Furthermore, RE elements also shows magnetic behavior due to their incompletely filled inner f electron shells, which means the increase in the RE content of the alloy can be resulted with increase in magnetic properties [84]. So, adding Ni and excess amounts of RE should be avoided. In addition, Cr and Mn are diamagnetic elements and have a suppressing effect on ferromagnetic behavior.
- Refractory metals also increase the Young's modulus (E) of the BASs [11]. Since the bonds between Fe and B, addition of B increases the fracture strength of the BAS alloys.
- Addition of Cr and Mo increases the corrosion resistance of the system. However, high amounts of Mo are not favorable for corrosion resistance because the high contents of Mo prevent the dissolution of Cr during passivation.
- Also theoretical studies which were conducted before in NOVALAB [88] showed the effects of elemental additions on various binary systems and enthalpy of mixing and critical cooling rate to reach amorphous structure. Among the theoretically modeled binary systems, Fe-Mo system can be

easily distinguished by its more negative heat of mixing, and lower critical cooling rate values that is higher predicted glass forming ability.

### **2.4.3. Production Methods of Bulk Amorphous Steels**

#### **2.4.3.1. Copper Mold Casting**

This production route is one of the most popular and common way to fabricate BMGs. In this technique, molten alloy is poured into a copper mold which effectively solidifies the alloy due to the quick heat extraction by copper mold. The constituent materials of the BASs alloyed mainly with induction melting and then casted into copper mold with various shapes under Ar atmosphere. In this technique, controlling the temperature is important due to the change of viscosity with temperature. Therefore, the experiment result can vary with the conditions of the production.

#### **2.4.3.2. Suction Casting**

Another commonly used way of producing BASs is suction casting. The figure below explains this method basically. The alloy is prepared by arc melting. Then, the alloyed sample is re-melted to be casted into copper mold by pressure differential between main chamber and casting chamber. The advantageous part of this production method is that cooling rates can be controlled by adjusting the pressure difference between chambers.  $10^5\text{K/s}$  cooling rates can be reached by this production route which is enough to synthesize BASs.



**Figure 2.8** Image of arc melting device with suction casting unit

### **2.4.3.3. Centrifugal Casting**

This procedure was developed to produce various BMGs in Novel Alloys Design and Development Laboratory (NOVALAB) [25, 89]. It was inspired from jewelry usage which has the same method. The most important feature of this production technique is that alloy is produced by completely conventional route with almost same conditions in industry. This feature will definitely lower the cost of the BASs. Alloys are prepared first with arc melting and then by the help of BN coated alumina crucibles re-melted and casted into pre-cooled copper molds. This route is one of the most promising candidates for the mass production of BMGs commercially.

## **2.5. Glass Forming Ability and Parameters**

Synthesizing metallic glasses in an affordable and a consistent way, and producing them in mass quantities, glass forming abilities of BMGs should be increased. The term of glass forming ability (GFA) can be defined in simple terms as the ability of the alloy to transform into amorphous state. So as to determine the GFA of BMGs, lots of different parameters have been developed according to the thermal characteristics of the systems. This section will cover these parameters and their advantages.

### **2.5.1. Reduced Glass Transition Temperature ( $T_{rg}$ )**

Glass formed when the viscosity of the molten alloy increased once it was cooled from melt to a temperature below  $T_g$ . Turnbull [4] suggested consistent with the kinetics of crystal nucleation that,  $T_g/T_l$  could be a well indicator to define the GFA of the system. Since the only way to produce metallic glasses is melt spinning in the time when  $T_{rg}$  parameter was developed, it does not depend on diameter or the crystallization temperature of the sample.

Turnbull also established a 2/3 ratio for the complete suppression of the homogeneous nucleation of the crystalline phase which was based on the nucleation theory. However,  $T_{rg} \approx 0.40$  is shown as a minimum necessary value for an alloy to form glass [17].

### **2.5.2. Supercooled Liquid Region ( $\Delta T_x$ )**

Inoue [6] proposed that, as the  $\Delta T_x$ , which is the region between the  $T_g$  and the  $T_x$ , becomes wider, the glassy phase is more stable and shows more resistance to crystallization. Furthermore, he implied that an alloy having a wide  $\Delta T_x$  will have a lower critical cooling rate. However the Pd-based metallic glasses which have the

minimum cooling rate necessities with average width of  $\Delta T_x$  showed that this perception about GFA is not completely correct.

### 2.5.3. The $\gamma$ and $\gamma_m$ Parameters

These parameters were developed based on physical metallurgy and the information on TTT diagrams. Lu and Liu [90] consider the two kinds of stability of BMGs to develop  $\gamma$  parameter. First one is the thermodynamically stability of the BMGs, lower the  $T_l$  higher the stability of liquid, and the other one is the resistance to crystallization, determined by the value of the  $T_g$ . Combination of these two views gave the GFA as:

$$\gamma = \frac{T_x}{T_g + T_l} \quad (2.3)$$

Then, this criterion had been enhanced by including the stability of supercooled liquid region. As it was mentioned before, wider  $\Delta T_x$ , more stable liquid against crystallization obtained. In the light of this information Du et. al. [91] extended the parameter as:

$$\gamma_m = \frac{2T_x - T_g}{T_l} \quad (2.4)$$

Moreover, by plotting this parameter as a function of critical cooling rate ( $R_c$ ), they found a linear relationship:

$$\log_{10} R_c = 14.99 - 19.441\gamma_m \quad (2.5)$$

### 2.5.4. The $\alpha$ and $\beta$ Parameters

Again, considering the same requirements to determine  $\gamma$  and  $\gamma_m$  parameters, Mondal and Murty [92], derived the  $\alpha$  parameter by measuring the stability of the amorphous phase with respect to the glass transition and the stability of the liquid in relation with the liquidus temperature.

$$\alpha = \frac{T_x}{T_l} \quad (2.6)$$

In the same study, they also mentioned that by considering  $T_{rg}$ , another parameter could be derived:

$$\beta = \frac{T_x}{T_g} + \frac{T_g}{T_l} \quad (2.7)$$

### 2.5.5. The $\omega$ Parameter

Long et. al. [93] proposed another GFA parameter which covers the thermodynamic properties of BMG systems based on the analysis of the TTT diagrams of the glass former liquids using fragility concept. They claimed that this parameter is statistically one of the best criteria to determine the GFA and it could also be used for oxide glasses and cryoprotectants.

$$\omega = \frac{T_g}{T_x} - \frac{2T_g}{T_g + T_l} \quad (2.8)$$

### 2.5.6. Ideal Value of the GFA Parameters

**Table 2.5** Ideal values of the discussed GFA parameters

<b>Parameter</b>	<b>Ideal Value</b>
$T_{rg}$	1.0 [4]
$\Delta T_x$	0.0 [94]
$\gamma$	0.5 [90]
$\gamma_m$	1.0 [91]
$\alpha$	1.0 [92]
$\beta$	2.0 [92]
$\omega$	0.0 [93]

## 2.6. Crystallization Kinetics

Sample exposing to heating a temperature above glass transition and crystallization, nanocrystal nucleation and formation could be observed in metallic glasses. The mechanism behind the formation could be varied in different systems. By applying different perspectives in thermal analysis, different parameters such as activation energies or critical cooling rates could be found. In order to understand the mechanism behind the nucleation during the heating of metallic glasses and characterize these parameters, kinetic models were proposed.

### 2.6.1. Isochronal Crystallization Kinetics

The logic behind the isochronal crystallization kinetics is that the changes in the behavior of the obtained peaks from DSC with various heating and cooling rates are investigated and according to the observed shifts in these peaks, activation energies could be determined. The well-known approaches for isochronal crystallization kinetics are Kissinger and Ozawa methods.

According to Kissinger method [95]:

$$\ln\left(\frac{\beta}{T_p^2}\right) = \frac{-E}{RT_p} + A \quad (2.9)$$

where  $\beta$  is the heating rate (K/s),  $R$  is the universal gas constant,  $T_p$  is the peak temperature and  $A$  is the equation constant.

In this approach, activation energies of different phase transformation can be obtained from the slope of the  $\ln(\beta/T_p^2)$  versus  $1000/T_p$  graph.

Ozawa approach for isochronal crystallization kinetics [96, 97] is another popular way to calculate the activation energies:

$$\ln(\beta) = \frac{-1.0516E}{RT_p} + A \quad (2.10)$$

Again by calculating the slope of the  $\ln\beta$  versus  $1000/T_p$  curve, activation energies can be determined.

Many efforts were given also to calculate the critical cooling rate based on isochronal crystallization kinetics. Barandiaran and Colmenero [98] developed a relation to determine the critical cooling rate:

$$\ln R = \ln R_c - \frac{B}{(T_l - T_{xc})^2} \quad (2.11)$$

where  $R$  is cooling rate,  $T_l$  is the onset temperature of fusion and  $T_{xc}$  is onset temperature of solidification.

### 2.6.2. Isothermal Crystallization Kinetics

The main idea behind isothermal crystallization kinetics is: if metallic glass is heated up to the supercooled liquid region after an incubation time, it will start to crystallize. From Johnson-Mehl-Avrami approach, the mechanics of crystallization and the incubation time necessary to crystallization can be determined. Johnson-Mehl-Avrami relation [99, 100] is given below:

$$X = 1 - \exp[-k(t - \tau)^n] \quad (2.12)$$

where  $X$  is the volume fraction of crystals,  $\tau$  is the incubation time,  $k$  is the reaction constant and  $n$  is the Avrami exponent.

The Avrami exponent will give the mechanisms of nucleation and growth.



## CHAPTER 3

### EXPERIMENTAL PROCEDURE

#### 3.1. Raw Materials

In this thesis BAS samples were produced by using scrap cast irons. The weight percentages of the elements in this scrap cast iron are given in the Table 3.1.

**Table 3.1** The elements in the scrap cast iron and their weight percentages

Element	Wt.%	Element	Wt.%
Fe	92.770	Al	0.003
C	4.330	Ca	0.002
Si	2.090	V	0.016
Mn	0.400	B	0.001
P	0.050	Zn	0.005
S	0.059	Pb	0.003
Cr	0.060	As	0.005
Ni	0.090	Ti	0.016
Cu	0.210	Co	0.016
Mo	0.004	Zr	0.004
Sn	0.003		

Stated scrap cast iron is denoted as “M” in the alloy compositions. These cast iron scraps were alloyed with high purity elements obtained from Alfa Aesar. The purities of alloying elements are given in Table 3.2.

**Table 3.2** The purity grades of the elements used in the alloy preparation

<b>Element</b>	<b>Grade</b>
Mo	99.95%
Cr	99.20%
B	99.50%
Y	99.90%
Ti	99.70%
V	99.70%
Al	99.90%
Mn	99.90%

Alloys that are studied could be classified into three categories as:

- (i)  $M_{60}Cr_{13}Mo_{17}B_8Y_2$  as base alloy,
- (ii)  $M_{60}Cr_{13}Mo_{17-x}B_8Y_2X_x$  (X= Ti, V, Al and Mn)
- (iii)  $M_{60}Cr_{13}Mo_{17-x}B_8Y_2Mn_x$  (x=0-10)

Compositions of the BAS samples were selected according to the foreseeing of the high GFA and the thermal stability of the system from the information mentioned before (see Section 2.2.2). Because precision of the alloys are important for fabricating BMGs, all constituent materials were weighted up to forth decimal.

### **3.2. Production of the Samples**

Samples were firstly alloyed and homogenized in arc melting. Then rapid cooling rates were applied to obtain fully amorphous structure by centrifugal casting and suction casting. Because cast irons were in scrap form, the oxide layer in the surface was polished before melting to get rid of the detrimental effect of oxygen.

### **3.2.1. Arc Melting**

Designed compositions were prepared by alloying scrap cast irons with high purity constituent elements by Edmund Bühler arc melting under Zr-gettered argon atmosphere. To avoid any kind of contamination, copper mold was cleaned with special cleaning solution for metallic surface, acetone and alcohol before every experiment. Furthermore, oxygen in the chamber of arc melting device minimized by evacuation process by rotary and diffusion pump followed by high purity argon flushing for at least 3-4 times. The samples were re-melted for three to four times for complete homogeneity and each time they were rotated upside-down to ensure the homogeneity.

### **3.2.2. Rapid Solidification by Centrifugal Casting**

As it was stated in Section 2.4.4.3, centrifugal casting was firstly used to fabricate BMGs in NOVALAB. Samples were produced by completely conventional route. Pre-alloyed specimens were replaced into alumina crucibles, produced by the own resources of NOVALAB, and re-melted with induction melting with a controlled temperature chamber which was also controlled by evacuating the air and flushing with argon. After, the screened alloy was transformed into liquid form, arms of the commercially available Manfredi Neutromag Digital centrifugal casting device starts to rotate rapidly and molten alloy transferred into the precooled wedge-shaped copper mold (cavity dimensions of  $t$ mm – 16mm – 70mm where  $t$  varies between 1 and 3mm) by the help of centrifugal force. Specimens having variable thicknesses can be fabricated by this process (Figure 3.1.a).

### **3.2.3. Rapid Solidification Suction Casting**

Another rapid solidification technique that is used to synthesize the BAS samples is suction casting. The suction casting unit is equipped into Edmund Bühler Arc

Melting device. The same procedure in arc melting was followed for oxygen free atmosphere and homogenization of the alloys. However, final shapes of the specimens were given by a water-cooled copper mold with a cavity dimension of 3mm in diameter and 15cm in length. By suction casting, rod-shaped specimens were fabricated having 3mm-diameters (Figure 3.1.b).

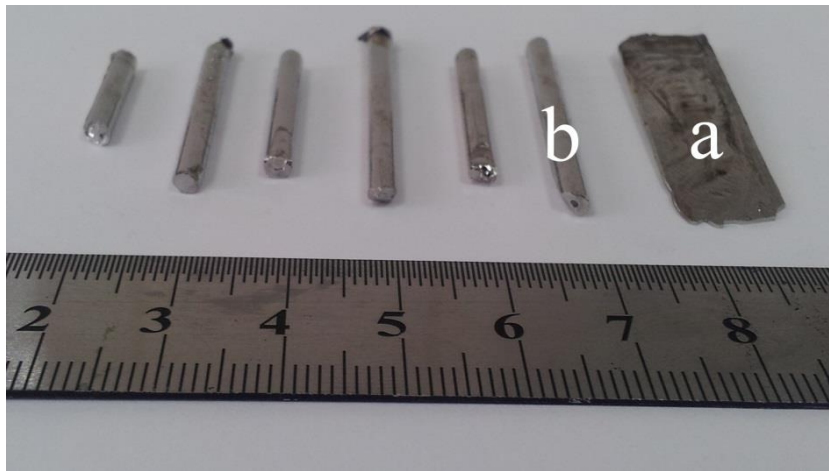


**Figure 3.1** The samples produced by a) centrifugal casting b) suction casting

### 3.3. Characterization Techniques

In this study, various characterization tools were operated to determine the structure of the samples, examine the microstructural evolution, resolve the thermal and magnetic characteristics and reveal the mechanical behavior of the BAS samples.

#### 3.3.1. X-Ray Diffractometry

Structures of the samples, whether they were amorphous or crystalline, were examined by X-Ray Diffraction (XRD) analysis by Rigaku D/MAX 2200 Diffractometer. Monochromatic Cu  $K_{\alpha}$  was used during the analysis in the diffraction angle ( $2\theta$ ) range of  $10-100^{\circ}$  with a scanning rate of  $2^{\circ}/\text{min}$  and step size

of  $0.02^\circ$ . The qualitative phase analyses of the samples which contain crystalline phases in their structures were performed by interpreting the XRD patterns.

### **3.3.2. Microstructural Investigation**

Microstructural characterizations of the samples were performed by FEI Quanta 400F field emission scanning electron microscope (SEM) equipped with energy dispersive spectroscopy (EDS). EDS was used to identify the composition of the alloy and the phases were presented in microstructure.

Each sample was prepared by firstly mounting a piece of it to the bakelite. Then, they were grinded with SiC abrasive papers and polished with diamond polisher. Polished samples were etched with Marble's Reagent, containing 10gr  $\text{CuSO}_4$ , 50ml HCl and 50ml water in the solution. This strong etchant was preferred because of the resistance of the samples to corrosion.

### **3.3.3. Differential Scanning Calorimetry**

Thermal characteristics of the BASs are one of the most important features of these kinds of materials. These critical thermal parameters are glass transition temperature ( $T_g$ ), crystallization temperature ( $T_x$ ), melting temperature ( $T_m$ ) and they were determined via SETSYS-16/18 high temperature differential scanning calorimeter (DSC) with a heating and a cooling rate of 40K/min under constant argon gas flow in a temperature range between 303-1673K. During the thermal analyses, 20-30mg of sample was used. These instruments were calibrated for a wide range of temperatures and scanning rates by using standard high purity elements of Al, Zn, Pb, Ag, Au and Ni.

Crystallization process of the bulk amorphous steels was characterized by both linear heating and cooling runs from 303K to 1673 K to acquire a set of DSC scans

with heating and cooling rates ranging from 5 to 99 K/min. Furthermore, isothermal crystallization analysis was also performed by DSC scans.

#### **3.3.4. Vibrating Sample Magnetometry**

ADE Magnetics Model EV9 Vibrating Sample Magnetometer (VSM) was used to determine the magnetic behavior of the synthesized samples. Magnetic field up to 1.8KOe was applied at room temperature and the behavior of the samples were observed with the intention of acquiring the magnetic parameters.

#### **3.3.5. Micro-Hardness Measurements**

Vickers microhardness measurements were performed on all produced and heat treated samples by an automated microhardness tester Shimadzu-2 Microhardness Tester with an indenter load of 1kgf. Reported averages of microhardness values were from at least eight measurements for each specimen.

#### **3.3.6. Corrosion Tests**

Corrosion resistances of the synthesized BASs were measured with subjecting selected specimens into extreme corrosive environments. Three different corrosive solutions were prepared and samples of pig iron, tool steel, stainless steel and bulk amorphous steel were subjected to these solutions for 15 days. Prepared solutions were:

- a) Highly acidic, 0.5M H<sub>2</sub>SO<sub>4</sub> solution with pH = 1.13
- b) Highly basic, 1M NaOH solution with pH = 14
- c) Neutral aggressive salt, 0.6M NaCl solution with pH = 7

The initial surface areas of the samples and the initial weights were measured before examinations. In every five days, observed weight losses were calculated to obtain the weight loss/gain per area.

## CHAPTER 4

### SYNTHESIS OF BULK AMORPHOUS STEELS IN AN ECONOMICAL AND CONVENTIONAL MANNER

#### 4.1. Introduction

Someone can think that BMGs will be the future of the materials owing to their unique properties. However, lots of improvements had to be done before adapting these promising materials. One of the problems that one should need to enhance is the cost of their fabrication. Since it needs lots of pure constituent elements to achieve stable liquid by ‘confusion’, its price will be very high to use commonly in industry. The elements used in bulk amorphous steel production are also high priced elements such as RE elements, Cr, B, etc. in their high purity forms. Another factor which increases the expense of the fabrication is the requirement of non-contaminated alloys. This requirement brings along another factor, the necessity of special production techniques with controlled atmosphere and rapid cooling rates. These two requirements prevent the BASs to be adapted into mass production.

The commercialization of these materials could only be actualized if the necessary cooling rate could be lowered and the fabrication expenses could be decreased. Increasing the glass forming ability of the system, in other words, stabilizing the liquid in the system will be resulted in reduced required cooling rates. Lowering cooling rates will be ensued more conventional, more common and less complex production techniques which will definitely decrease the manufacturing costs. The material expenses in the BAS fabrication could be reduced by using commercially available materials such as ferrous-alloys. Certainly, pure elements can also be used

to ‘confuse’ the system, but if the major part of the alloy system could be substituted by commercial grade materials, expense of the materials will show a rapid decline.

In the first part of this study, the motivation was the fabrication of economical BASs by substituting the major constituent elements with scrap cast iron with modifying of the BASs production route and replacing the complex and controlled processes with commercially available conventional centrifugal casting technique. With the knowledge from the previous simulation and experimental studies conducted in NOVALAB and from the inspiration from the published researches in literature, alloying additions to the scrap cast iron were determined.

#### **4.2. Design, Production and Characterization of Base Alloy**

The design of the BAS systems needs to consider limitations (see Section 2.2.2 and Section 2.4.2) such as:

- It should be synthesized from constituent elements with different atomic radius.
- The paramagnetic nature of BASs should be taken into account and elemental additions should be chosen with that sense.
- For enhanced GFA,  $T_g$  should be increased and  $T_l$  should be decreased. Critical thermal parameters can be boosted by adjusting the metalloids and refractory metal content in the system.
- For improvement of corrosion resistance, Cr and Mo addition have significant impact.

In addition, the theoretical calculations from previous studies in NOVALAB [88] suggest that among the theoretically modeled binary systems, Fe-Mo system can be easily distinguished by its more negative heat of mixing, and lower critical cooling rate values that is higher predicted glass forming ability.

Y has also an essential role on designing base BAS alloy composition. It offers lots of advantages than the other rare earth elements:

- It has high radius difference than the other constituent elements in BAS system.
- Lower cost when it compared to the same type elements (RE elements).
- Augment the GFA of the BAS systems.

Base alloy system was originated by combining previous studies (See Section 2.4.1) with mentioned concerns. This system contains scrap cast iron (denoted as M in alloy compositions) as Fe, C and Si source, Mo, Cr and Y.

Constituent elements were tuned with restrictions and the base alloy composition given as:  $M_{60}Cr_{13}Mo_{17}B_8Y_2$

Scrap pieces were first polished due to the oxide layer on it to get rid of the deteriorating effect of the oxygen on glass forming ability, and then homogenization of the alloy was done prior to conventional centrifugal casting by arc melting. As-prepared alloys casted into pre-cooled wedge shaped copper mold. As a result of the high viscosity of the molten alloy, the melting temperature could not be observed with bare eyes, but predicted as around 1500K. Shiny luster exhibited by amorphous phase was observed in the middle sections with 1.5 mm in thickness of the synthesized sample at initial macro examinations. For further confirmations of the amorphous phase, DSC and XRD analysis with SEM investigations were performed; these results were given in Figure 4.1 (a)-(c) respectively. DSC thermogram of the synthesized sample proved that glassy phase was existed in the structure which experience glass transition ( $T_g$ ) at 818K with extra ordinary supercooled liquid region ( $\Delta T_x = T_x - T_g$ ) near 120K and followed by three different crystallization events. However, broad and low intensity crystalline peaks, Fe-carbides, were encountered in XRD pattern of the same sample. The type of Fe-carbides crystallized still unclear because of the plentiful variations of Fe-carbides with close peak points. Nevertheless, the possible candidates were  $Fe_{23}C_6$  and  $Fe_2C$ . SEM results also showed dendrites were nucleated and tried to grow on the partially amorphous matrix but the rapid cooling rates prevent them to grow. The phase in the form of dendrite could not be labeled clearly, but it was confirmed with EDS analysis that it contained richer Mo than the matrix.

In summary, these promising results were boosted the motivation of the study and directly proved that the fabrication of the BASs could be succeeded by alloying cast iron scraps with conventional route.

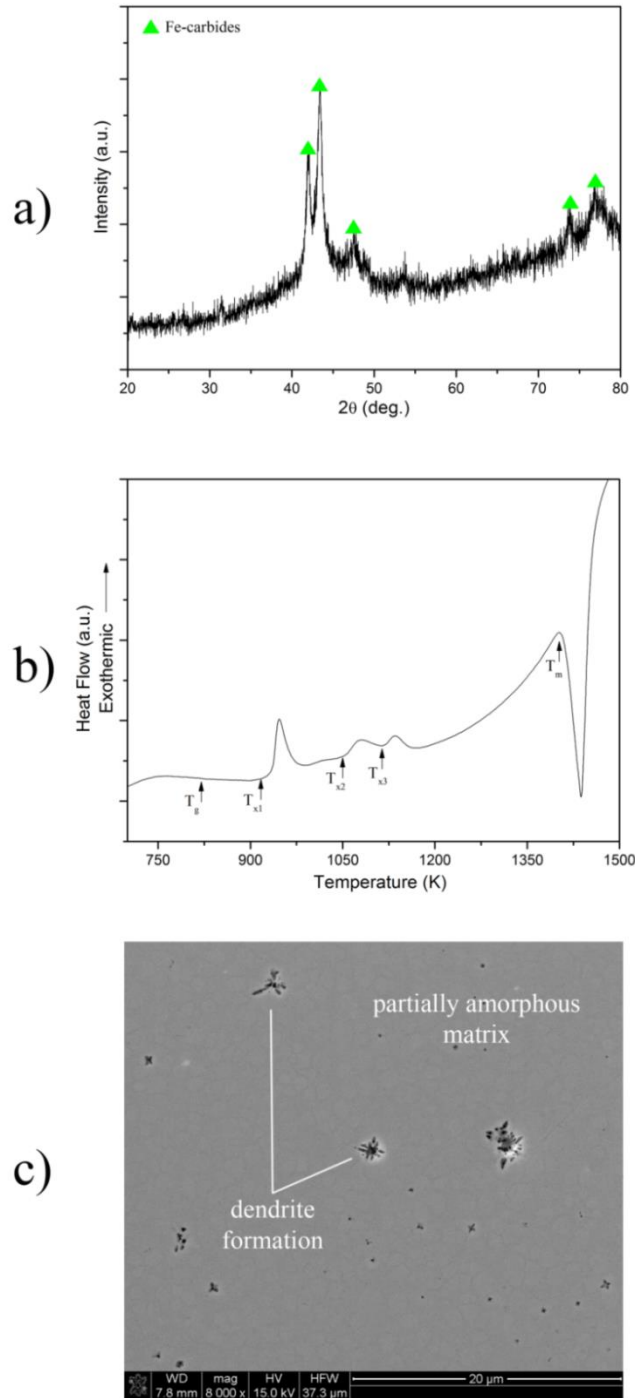


**Figure 4.1** a) XRD b) DSC c) SEM analysis of centrifugally casted base alloy

### 4.3. Carbide Destabilization by Alloying Element Addition

As discussed in Section 4.2, the characterization of base alloy showed that Fe-carbides phases in the structure prevented to achieve the fully amorphous structure in base alloy. If these crystalline phases could be destabilized by alloying additions, homogenous glassy structure could have been obtained. With basic approach, Ellingham diagram for carbide formation (Figure 4.2), could be a practical tool to determine the candidate elements.

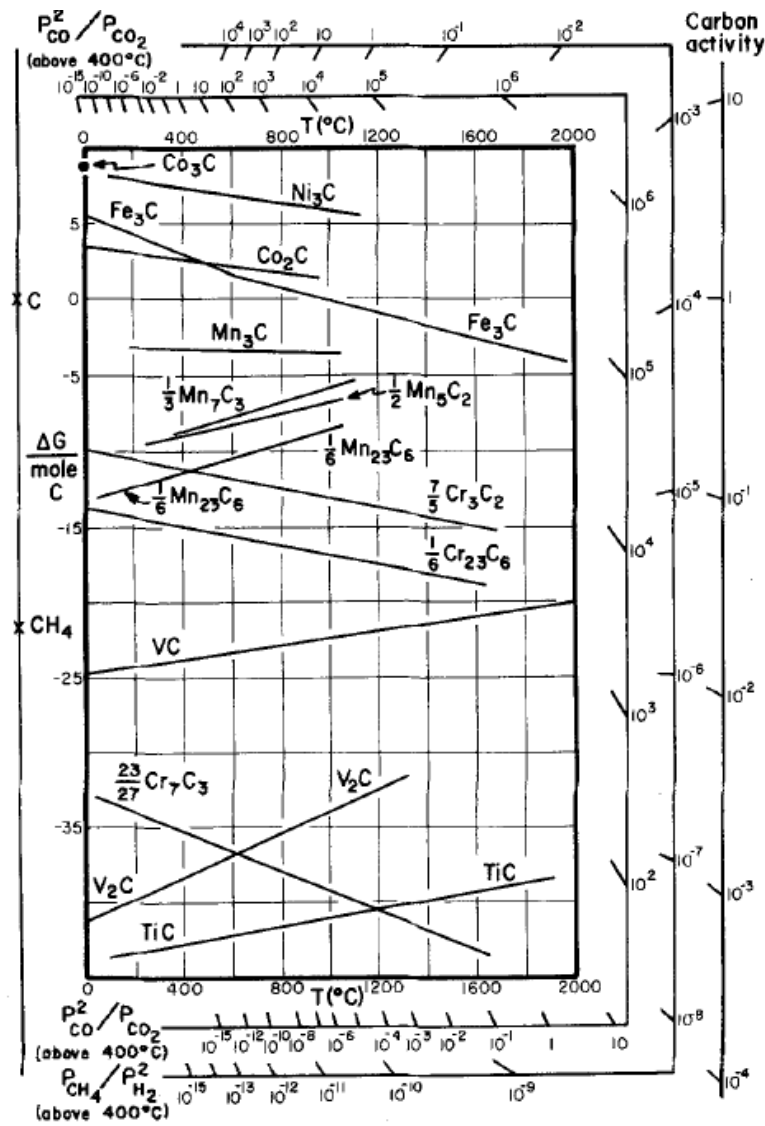


Figure 4.2 Ellingham Diagram for carbide formation [101]

Furthermore in 2012, Ande and Sluiter [102] published an article about the effect of common alloying additions to the stabilities of Fe-carbides. They simulated a supercell where alloying elements substituted with Fe atoms in all possible Fe-occupied Wyckoff sites. According to these simulation results, while Al, V, Ti and Mn destabilize the different Fe-carbides presented in the study by decreasing their formation enthalpies below zero, Mo seemed to stabilize these carbide phases.

Enhancing the GFA of the samples and destabilize the carbide phases presented in the structure, Ti, V, Al and Mn were added to the base alloy with same amount reduction of Mo. In order to see the effectiveness of these alloying additions, these elements were added only 3 at.% to the main composition. New compositions were presented as  $M_{60}Cr_{13}Mo_{17-x}B_8Y_2X_x$  ( $X= Ti, V, Al$  and  $Mn$ ) and where  $x=3$  for the first part of the study:

- $M_{60}Cr_{13}Mo_{14}B_8Y_2Ti_3$
- $M_{60}Cr_{13}Mo_{14}B_8Y_2V_3$
- $M_{60}Cr_{13}Mo_{14}B_8Y_2Al_3$
- $M_{60}Cr_{13}Mo_{14}B_8Y_2Mn_3$

Both conventional centrifugal casting and suction casting were used to synthesize these BAS alloy systems. All samples were fully characterized and the obtained results were compared with the base alloy.

It was found via XRD from the samples fabricated by conventional centrifugal casting having 1.5mm thickness with wedge form that after adding 3 at.% Ti and V to the base alloy (See Figure 4.3), some phases presented were destabilized but amorphous structure did not completely attained. Ti is an  $\alpha$ -Fe stabilizer, so as Ti was introduced to the alloy system, tendency to form  $\alpha$ -Fe was observed in XRD analysis [103]. Moreover, adding Ti to the base alloy also cause TiC formation. However, addition of Al showed that amorphous phase was stabilized almost completely, only a little fraction of crystalline phases were appeared. The sample which contains 3at% Mn showed the characteristic XRD pattern of a glassy sample.

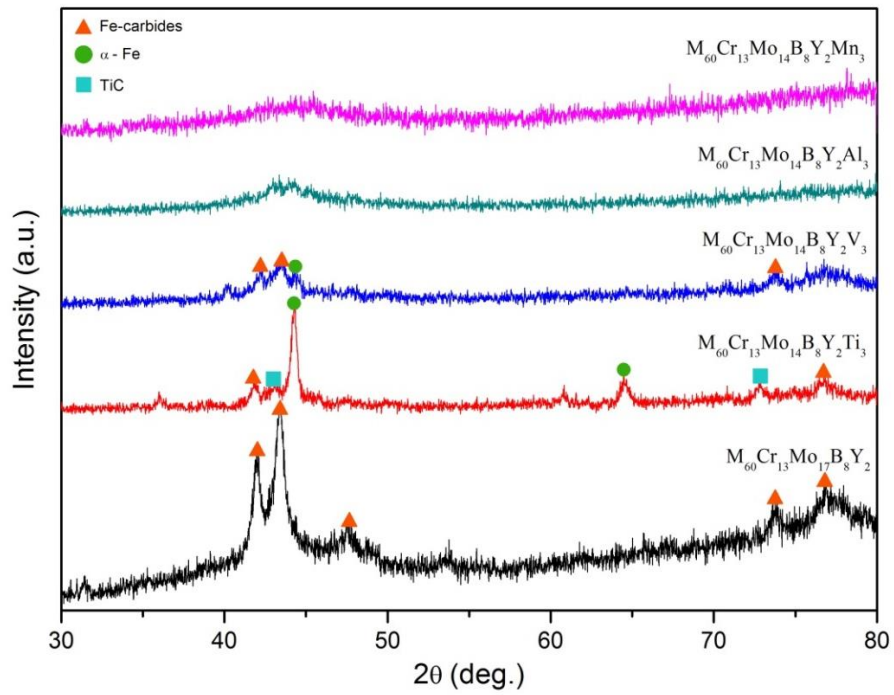


**Figure 4.3** XRD patterns of base alloy and elemental additions

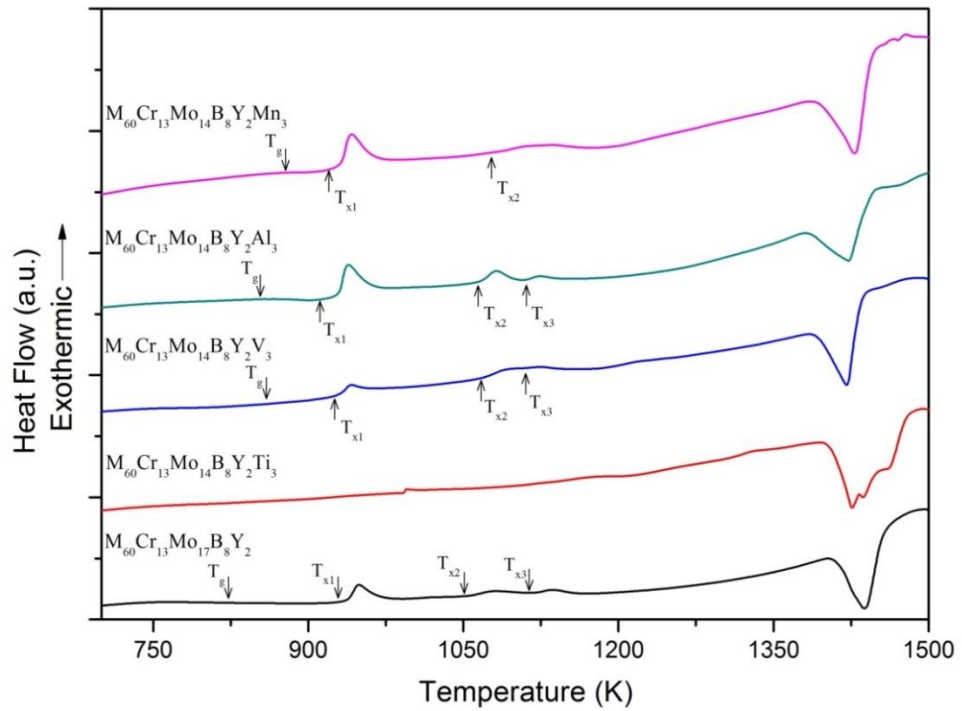


**Figure 4.4** DSC plots of base alloy and elemental additions

All samples were heated up to 1673 K via DSC. The critical thermal parameters such as glass transition temperature ( $T_g$ ), crystallization temperature ( $T_x$ ), supercooled liquid region ( $\Delta T_x$ ) and liquidus temperature ( $T_l$ ) were determined. The samples that involved glassy phase in its structure exhibit glass transition followed by supercooled liquid region and exothermic peaks due to the crystallization. Fig. 4.4 clearly indicates that Al, Mn and V added samples had glassy phase in their structure similar to the base composition. Additions of Ti deteriorated the glass forming ability and became an unsuccessful attempt to preserve the amorphous structure.

Another important fact is that the crystallization trends of the samples were also changed. Three different crystallization events were observed in the base alloy. However with the addition of Ti, no amorphous structure was detected, in other words crystallization was not even noticed. Additions of Al and V to the base alloy did not change the crystallization trend, they retained mentioned three crystallizations while heating. Even 3at.% addition of Mn changed the crystallization characteristic of the base alloy. While the samples without Mn showed successive stepwise transformation from metastable undercooled liquid to equilibrium crystalline phases, when Mn introduced this successive crystallization steps united into two events and simultaneous precipitation was observed in one step. It can be interpreted as the compositional requirements for the formation of critical nuclei was not satisfied and the critical nucleus size may not be achieved (increase in confusion of the system) [26]. So the thermal stability and glass forming ability of the system was increased. Critical temperatures were given in Table 4.1.

Even with a small amount of alloying addition, around 30-40K increments were observed on  $T_g$ , which showed the resistance to crystallization was increased for these samples. However, since the crystallization temperature was almost same for all elemental additions, supercooled liquid region became narrower. Even if there was a decrease in supercooled liquid region, around 60-90K width  $\Delta T_x$ , which is not a usual value for Fe-based BMGs obtained. Crystallization temperatures and liquidus temperatures did not change drastically with elemental addition.

**Table 4.1** Critical thermal parameters of samples  $M_{60}Cr_{13}Mo_{14}B_8Y_2X_3$ 

Alloys	$T_g$ (K)	$T_{x1}$ (K)	$T_{x2}$ (K)	$T_{x3}$ (K)	$T_1$ (K)	$\Delta T_x$ (K)
Base alloy	818	936	1057	1120	1456	118
X = Ti	-	-	-	-	1475	-
X = V	844	931	1089	1114	1451	87
X = Al	842	902	1066	1111	1448	60
X = Mn	859	929	1087	-	1441	70

By combining theoretical GFA parameters with experimental facts, best alloy system or systems could be decided. Six different mentioned GFA parameters (see Section 2.5) were calculated and given in Table 4.2. Base alloy showed high GFA in accordance to the calculations due to its extraordinarily high super cooled liquid region but it was known by the experiments which showed partially amorphous structure in all attempts. Samples with Ti addition showed no glassy phase; consequently GFA could not be calculated. From basic approach,  $T_{rg}$ , Al and Mn added samples showed higher GFA. Furthermore, the samples with Mn addition preponderate in all other specimens by both experimentally and theoretically. Another remarkable performance was obtained from the samples contained Al in their composition. On most of the GFA parameters, these samples ranked second place after Mn added ones.

Up to that point, additions of Al and Mn were improved the thermal characteristics, GFA and the fraction of the glassy phase in the structure by both theoretical and experimental considerations.

**Table 4.2** GFA parameters of base alloy and alloy systems of  $M_{60}Cr_{13}Mo_{14}B_8Y_2X_3$

Alloys	$T_{rg}$	$\gamma$	$\gamma_m$	$\alpha$	$\beta$	$\omega$
Base alloy	0.561	0.412	0.724	0.643	1.706	0.155
X = Ti	-	-	-	-	-	-
X = V	0.581	0.406	0.702	0.642	1.685	0.171
X = Al	0.582	0.394	0.664	0.623	1.652	0.198
X = Mn	0.596	0.404	0.693	0.645	1.678	0.178

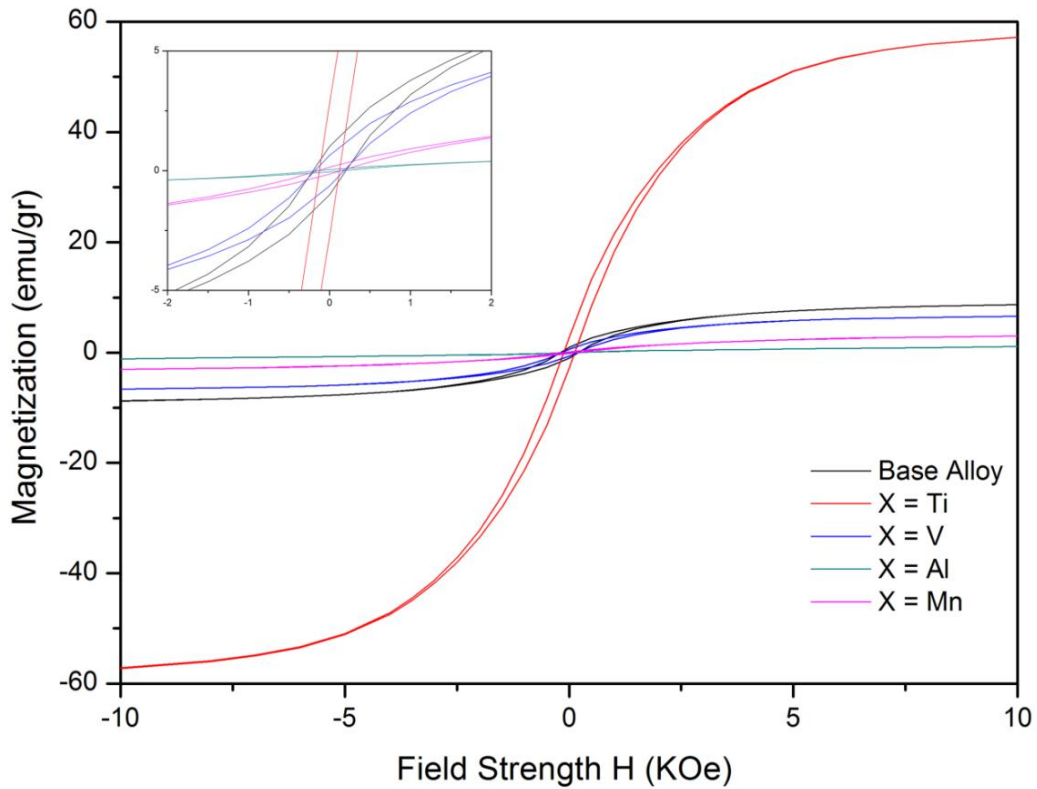


**Figure 4.5** Hysteresis loops of base alloy and  $M_{60}Cr_{13}Mo_{14}B_8Y_2X_3$  alloy systems

The magnetic performances of the fabricated samples are also important because BAS are known as non-ferromagnetic BMG systems at room temperature. Since they have been developed in a totally conventional route, the success of the production could also be understood by the magnetic characteristic of the samples.

To understand the magnetic behavior of the samples, the room temperature magnetic measurements were conducted by VSM. The stabilization of  $\alpha$ -Fe phase in Ti added samples showed the effect on hysteresis loops. These samples behaved as soft magnets with 9.86 kA/m coercive field ( $H_c$ ) and 58.90 emu/gr saturation magnetization ( $M_s$ ). Base alloy itself and V addition to it showed similar ferromagnetic response.

The behavior could be seen from the amplified view in Figure 4.5 and it is neither hard magnetic nor soft magnetic.  $M_s$  and  $M_r$  values were much lower than Ti added sample, however they comprise an area under hysteresis loops due to trapped domains caused by rapid cooling rates. Mn and Al added samples showed almost perfect paramagnetism with low  $M_r$ ,  $M_s$  and near zero squareness which is another proof of their amorphous natures.

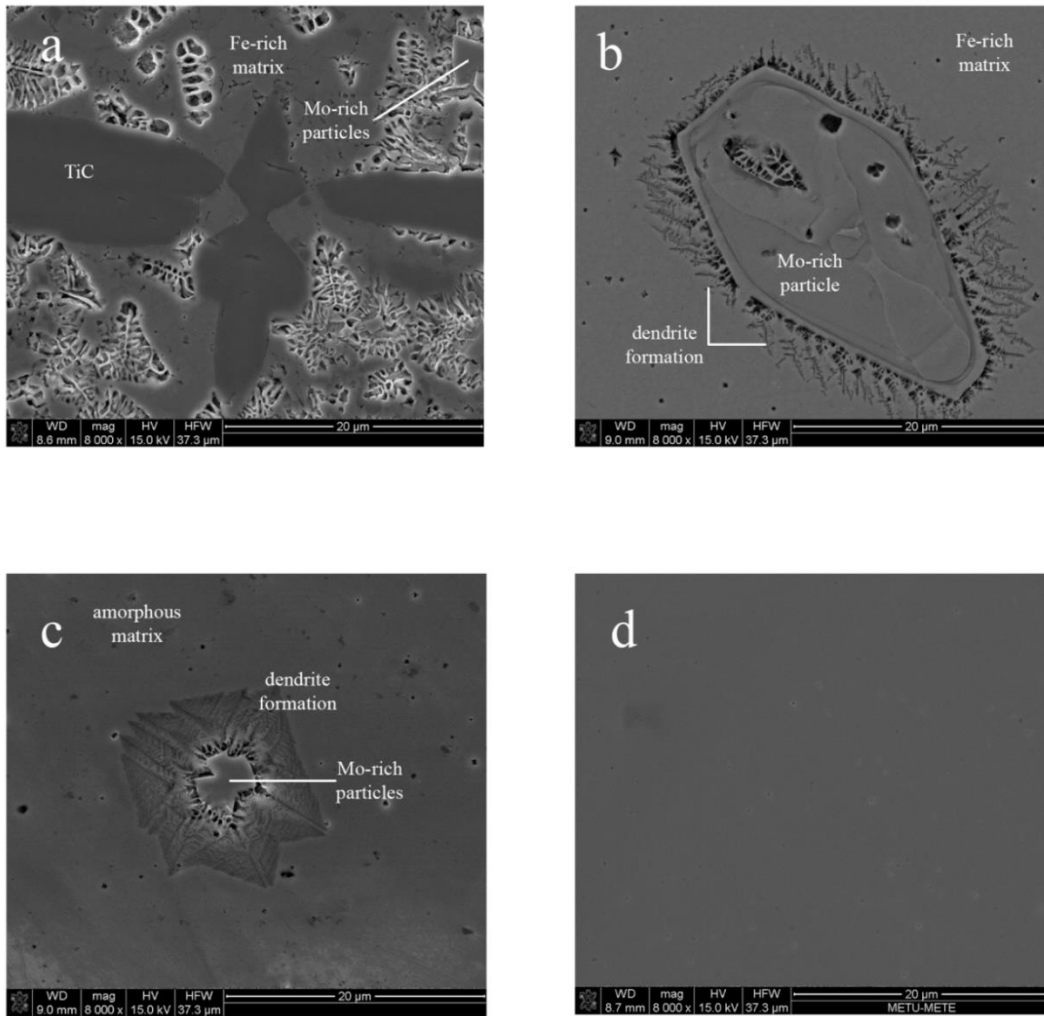


**Figure 4.6** SEM micrographs  $M_{60}Cr_{13}Mo_{14}B_8Y_2X_3$  alloy system taken from the 1.5 thickness of the wedge shape forms. These images belongs to a)  $X = Ti$  b)  $X = V$  c)  $X = Al$  and d)  $X = Mn$

Figure 4.6 shows the microstructural evaluation of the centrifugally casted alloy systems. When 3at% Ti was introduced to the alloy system (a), microstructure completely changed compared to the base alloy (see Figure 4.1) in same cooling rates. TiC formation was observed and also faceted particles which contain much higher Mo content than the matrix resolved by EDS scans. In the case of V and Al

addition, same Mo-rich particles were observed. As it can be seen from (b) and (c) dendrites started to grow from these Mo-rich faceted particles. These particles were observed all samples that contains crystalline phase in its structure. Moreover, early stages of dendrite formation can also be seen from these micrographs. According to these images, it could be assumed that Mo-rich faceted particles were formed before dendrites began to grow then followed by a dendrite growth on itself. Nevertheless, detailed examination and investigations were not completely performed because microstructural examination was not one of the main scopes of this study. Finally, samples having fully amorphous structure which are formed by addition of Mn (d) showed no contrast in SEM images. There were neither nucleated particles nor formed dendrites, the only thing that can be seen from the micrographs was the etch pits formed in the process of the sample preparation.

In summary, for the first time, BASs productions were achieved with scrap precursors by commercially available conventional centrifugal casting method. All analysis indicated that addition of Al and Mn to the promising base alloy with subtracting same amount of Mo succeeded to form amorphous phase in the samples with enhanced glass forming ability and higher resistance to crystallization. In addition, these samples showed almost no ferromagnetic behavior in the magnetic measurements which is another important point to consider while fabricating BASs.

In the light of this information, to reach more attainment with better thermal characteristics and GFA both experimentally and theoretically, more Al and Mn were added to the base alloy with the same approach. The effects of these promising alloying candidates were investigated much further.

#### **4.4. Effect of Al and Mn**

Due to reasons discussed in Section 4.2 and 4.3 and to choose the best alloying candidate, more additions of Al and Mn to the current base alloy

( $M_{60}Cr_{13}Mo_{17}B_8Y_2$ ) alloy composition are determined via suction casting method in order to ensure the increase in GFA and thickness of the amorphous structure.

Two sets of new alloy composition with totally six samples were prepared. New alloy system sets were presented as  $M_{60}Cr_{13}Mo_{17-x}B_8Y_2Al_x$  and  $M_{60}Cr_{13}Mo_{17-x}B_8Y_2Mn_x$  where  $x = 3, 6$  and  $9$  individually. All of these alloys were formed in shape of rods with 3mm in diameter. XRD patterns of these alloy systems could be seen in Figure 4.7. While Al added samples showed  $\alpha$ -Fe peaks in XRD pattern, 6 and 9 at.% additions of Mn maintain the characteristic amorphous halo shaped patterns. However Fe-carbide peaks were observed in 3 at.% Mn addition. Previously investigated samples of 3at.% Mn addition were taken from the middle section of the centrifugally casted specimens (1.5mm thickness). Because the specimen thicknesses were increased in suction casting case, the cooling rate might be insufficient for this sample to produce fully amorphous structure. Another important point of this analysis which should be emphasized is that as the Al content of the alloy increased,  $\alpha$ -Fe phase became more stable. Similarly in the case of Ti addition to base alloy (See Section 4.3), Al is another  $\alpha$ -Fe solid solution phase stabilizer in Fe-based alloys [103].

As mentioned in the previous section, samples containing Mn maintain their two crystallization events in their DSC thermogrammes. Even though alloys containing 3at.% Mn showed crystal peaks in the XRD, all of the samples showed clear glass transition followed by two crystallizations.

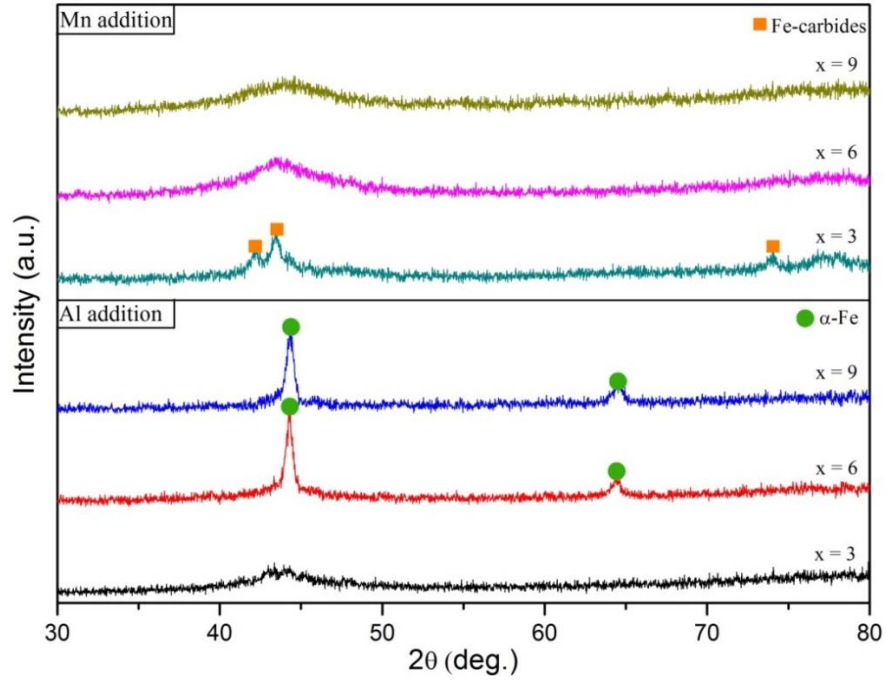


**Figure 4.7** XRD diffractograms of suction casted  $M_{60}Cr_{13}Mo_{17-x}B_8Y_2Al_x$  and  $M_{60}Cr_{13}Mo_{17-x}B_8Y_2Mn_x$  alloys where  $x = 3, 6$  and  $9$  individually

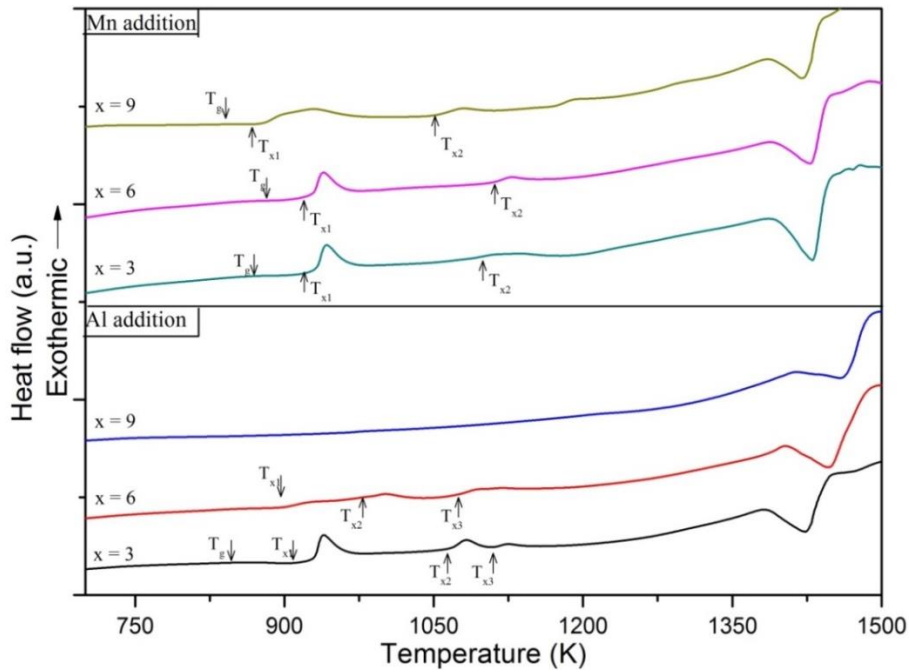


**Figure 4.8** DSC thermograms of suction casted  $M_{60}Cr_{13}Mo_{17-x}B_8Y_2Al_x$  and  $M_{60}Cr_{13}Mo_{17-x}B_8Y_2Mn_x$  alloys where  $x = 3, 6$  and  $9$  individually

**Table 4.3** Critical temperatures for  $M_{60}Cr_{13}Mo_{17-x}B_8Y_2Al_x$  and  $M_{60}Cr_{13}Mo_{17-x}B_8Y_2Mn_x$  alloys

Alloys	$T_g$ (K)	$T_{x1}$ (K)	$T_{x2}$ (K)	$T_{x3}$ (K)	$T_1$ (K)	$\Delta T_x$ (K)
x=3 Al	842	902	1066	1111	1448	60
x=6 Al	-	907	1011	1083	1470	-
x=9 Al	-	-	-	-	1476	-
x=3 Mn	859	929	1087	-	1441	70
x=6 Mn	875	925	1125	-	1432	50
x=9 Mn	851	876	1049	-	1428	25

**Table 4.4** GFA parameters of  $M_{60}Cr_{13}Mo_{17-x}B_8Y_2Al_x$  and  $M_{60}Cr_{13}Mo_{17-x}B_8Y_2Mn_x$  alloys

Alloys	$T_{rg}$	$\gamma$	$\gamma_m$	$\alpha$	$\beta$	$\omega$
x=3 Al	0.582	0.394	0.664	0.623	1.653	0.198
x=6 Al	-	-	-	0.617	-	-
x=9 Al	-	-	-	-	-	-
x=3 Mn	0.596	0.404	0.693	0.645	1.678	0.178
x=6 Mn	0.611	0.401	0.681	0.646	1.668	0.188
x=9 Mn	0.596	0.384	0.631	0.613	1.625	0.225

While Al as alloying element affected the samples adversely, addition of Mn produced fully amorphous and thicker samples with improved thermal characteristics. One of the highest glass transition among all bulk amorphous steel systems was obtained by adding 6at.% Mn to the base alloy. According to the Table 4.3, addition of Mn increased the  $T_g$  around 20K with almost same  $T_x$  up to 6at.% Mn addition. Naturally, up to that point supercooled liquid region became narrower. However, with further addition of Mn to the base alloy resulted in a decrease both  $T_g$ ,  $T_x$ , and  $\Delta T_x$ . It is clear that decrease of the  $T_x$  is much higher than the  $T_g$  which directly affected the  $\Delta T_x$  in a bad way. This depletion of  $T_x$  could be a marker about

the alteration of the crystallization mode and the product. Furthermore, addition of Al and Mn did not affect the liquidus temperature immensely, this temperature varied between 1428 and 1476K.

GFA parameters were also calculated and tabulated in Table 4.4. Due to unclear glass transition of sample including 6at.% Al, its GFA parameters could not be able to be calculated. According to Turnbull's criterion, as  $T_g/T_x$  ratio became closer to 2/3, liquid become very sluggish that it can only crystallize in a narrow temperature range [4]. Remarkable performance was obtained from the samples containing Mn in their composition and these additions gave very close  $T_{rg}$  values near mentioned critical value. On most of the GFA parameters, alloy with 6at.% Mn showed unexpected and unusual implementation.

Considering the previous studies on amorphous steels, the samples produced by cast iron scraps showed improved glass forming ability and thermal stability. For instance, when the production from pure constituent elements were the case according to the Ponnambalam et. al. study[44],  $Fe_{50}Mn_7Cr_{10}Mo_{10}Yb_2C_{15}B_6$  samples showed a  $T_g$  around 833K with  $\Delta T_x \sim 40K$ , on the other hand when the industrial constituent additions considered, according to a recent study by Tsai et. al.[66],  $Fe_{41}Cr_{15}Mo_{14}C_{(21-x)}B_xY_2Co_7$  ( $x=5-10$ ) samples showed  $T_g$  between  $\sim 783-833K$  with  $\Delta T_x \sim 55-80K$ . When Mn added samples compared with these examples, one of the highest  $T_g$  with high  $\Delta T_x$  achieved which is 850-875K and 25-70K respectively.

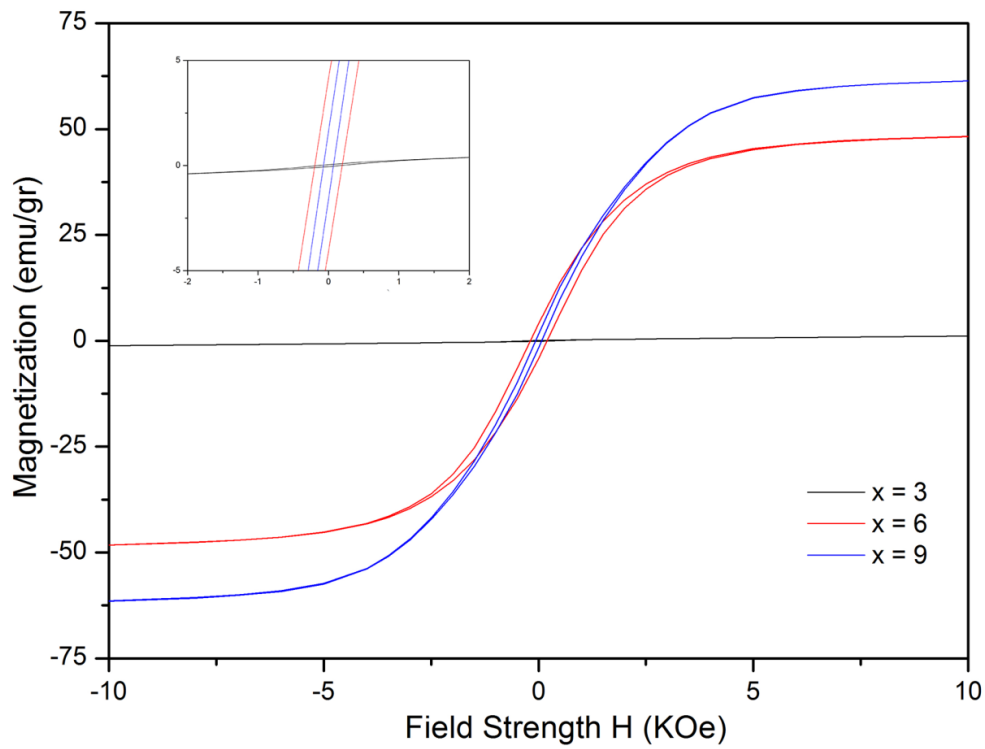


**Figure 4.9** Hysteresis loops of  $M_{60}Cr_{13}Mo_{17-x}B_8Y_2Al_x$  alloy systems

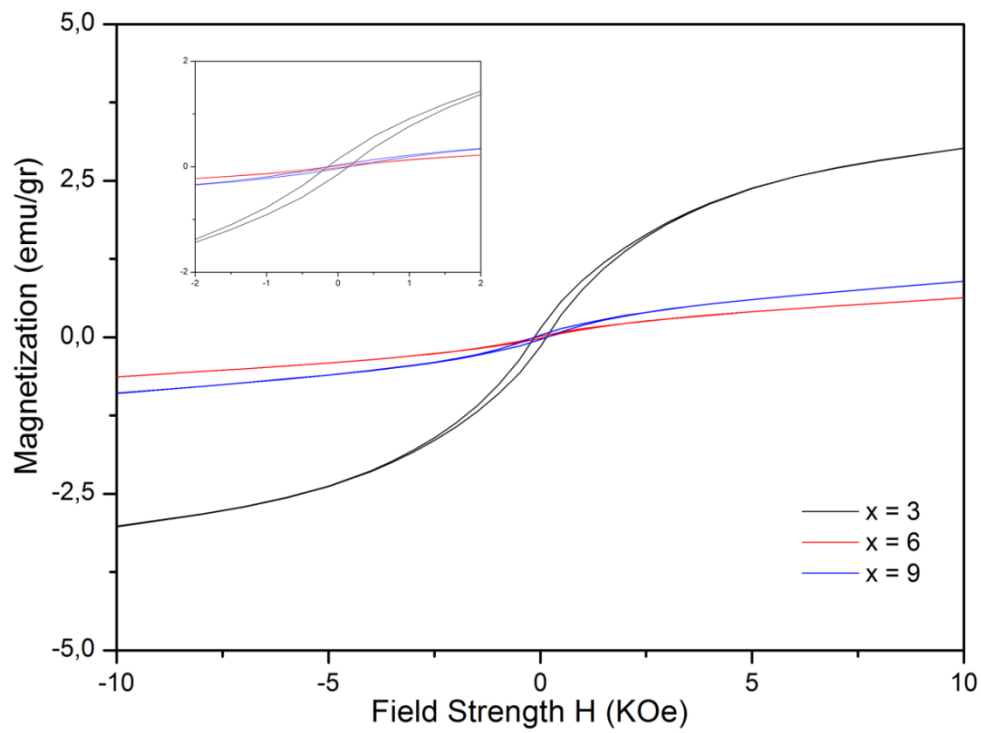


**Figure 4.10** Hysteresis loops of  $M_{60}Cr_{13}Mo_{17-x}B_8Y_2Mn_x$  alloy systems

To characterize the magnetic behavior of the samples, room temperature magnetic measurements were conducted. The stabilization of  $\alpha$ -Fe phase in 6at.% and 9at.% Al added samples behaved as soft magnets with 15.45 kA/m and 5.61 kA/m  $H_c$  and  $M_s$  of 49.20 emu/gr and 62.50 emu/gr respectively. Due to higher amount of  $\alpha$ -Fe phase in higher Al contents, better soft magnetic properties were obtained. The effect of Al on magnetic behavior can be seen in Figure 4.9.

Since increase in Mn content of the system affected GFA well and improved the fraction of amorphous structure, no magnetic response was observed for 6at.% and 9at.% Mn addition both by VSM measurements and Fe-Nd-B magnets. As it can be seen from the Figure 4.10, while samples contained 3at.% Mn showed a little magnetic behavior due to its partially crystalline nature, this behavior was almost vanished in further additions with near zero squareness values.

Because micrographs of the alloys containing 3at.% Al and 3at.% Mn were given in the previous section, micrographs only 6at.% and 9at.% additions of each elements are given in Figure 4.11. As discussed in the previous section of this chapter, the Mo-rich particles were again encountered in crystalline samples. Addition of Al more than 3at.% clearly shattered the amorphous structure. Although the phases presented in images (a) and (b) could not be completely identified, it was obvious that there was no trace of amorphous structure. Since the increase in Al content gradually vanished the amorphous structure, differences between these two images could be understood. While dendrites were not able to grow completely in (a), dendrite formations were completed in (b). Different sizes of particle were another expected difference between these two images.

Fully amorphous structures were obtained with additions of Mn to the base alloy and it was also confirmed by the SEM analysis by obtaining no contrast images (c) and (d).

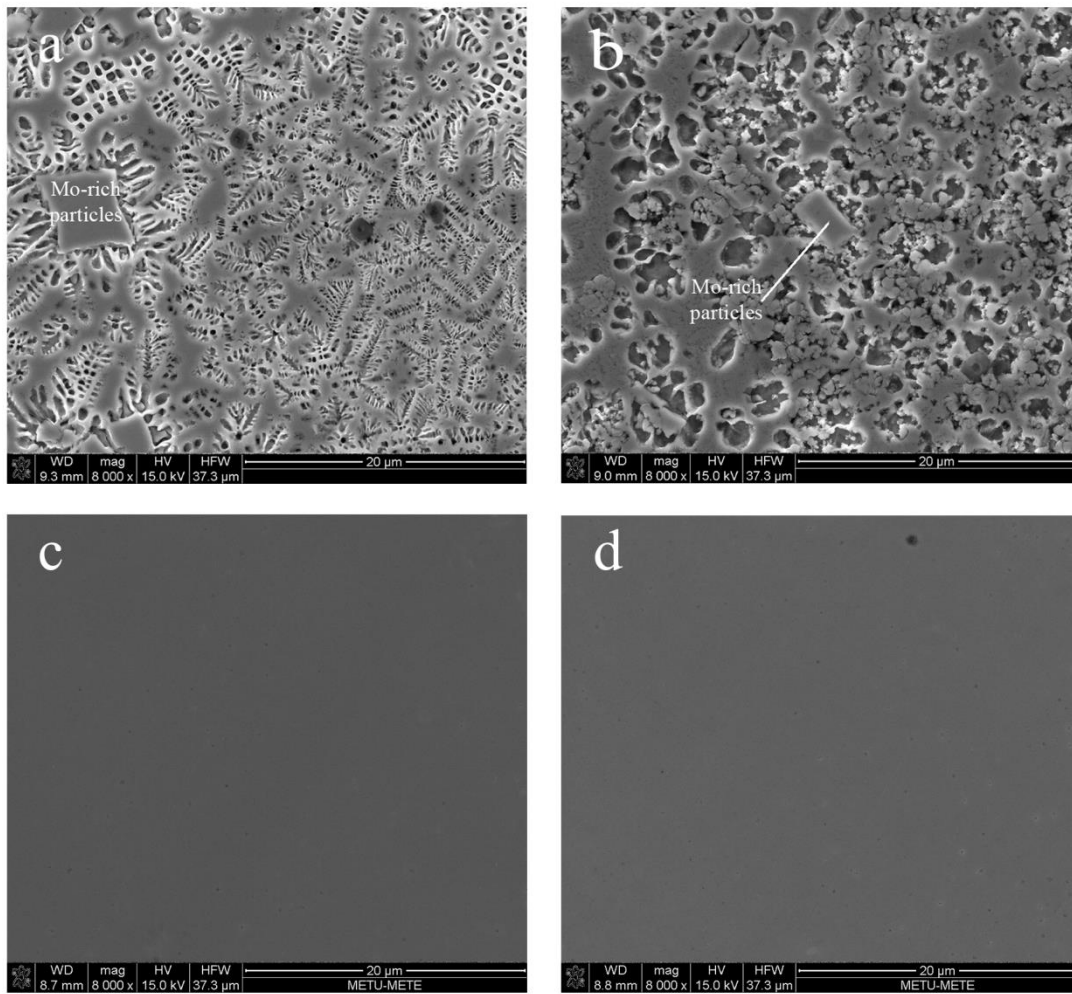


**Figure 4.11** SEM micrographs of produced BAS systems with compositions of a)  $M_{60}Cr_{13}Mo_{11}B_8Y_2Al_6$  b)  $M_{60}Cr_{13}Mo_8B_8Y_2Al_9$  c)  $M_{60}Cr_{13}Mo_{11}B_8Y_2Mn_6$  d)  $M_{60}Cr_{13}Mo_8B_8Y_2Mn_9$  at 8000 magnification

## CHAPTER 5

### IDENTIFYING THE BEST MANGANESE CONTENT FOR ENHANCED PROPERTIES OF BULK AMORPHOUS STEELS PRODUCED BY SCRAP CAST IRONS

#### 5.1. Introduction and Aim

In the previous chapter, BAS fabrication has succeeded by alloying scrap cast irons with pure elements with conventional production routes. Although, manufactured base alloy composition contained crystalline carbide phases in it, these carbides were destabilized by substituting Mo with Ti, V, Al and Mn. Not all gave the enhanced structure and thermal characteristics; however, even with small amounts of Al and Mn addition, the alloy reached to fully amorphous state. In order to find the best alloying addition to the base alloy, further additions have been made. While increment in Al content resulted in stabilized  $\alpha$ -Fe phase, which had a detrimental effect on amorphous structure, same increment in the Mn case caused improvement on both amorphous nature and the thermal characteristics.

In this chapter, the effect of Mn will be investigated to promote the properties of BASs by microalloying method. Thus, it is aimed to optimize the Mn content of the base alloy ( $M_{60}Cr_{13}Mo_{17}B_8Y_2$ ) and characterize this optimized BAS system in details. The optimization will be verified based on the comparison of theoretical glass forming ability parameters and experimental facts. Furthermore, as distinct from the previously operated characterization methods, further investigations such as corrosion measurements, kinetic analysis and mechanical testing will be applied to determine, understand and solve the specific characteristics of this optimized alloy system.

## 5.2. Production Route and Microalloying

Wide range of compositions were prepared and fabricated by suction casting. To observe the detailed effect of Mn, microalloying of Mn to the base alloy with an increment of 1 at.% per sample with the same amount of reduction in Mo. Prepared alloys could be denoted as  $M_{60}Cr_{13}Mo_{17-x}B_8Y_2Mn_x$  where x varies between 0 and 10. Same conditions and techniques were applied for the production and the characterization of the samples. The illustrative images of the samples having 3mm in diameter were given in Figure 5.1.



**Figure 5.1**  $M_{60}Cr_{13}Mo_{17-x}B_8Y_2Mn_x$  samples fabricated by suction casting

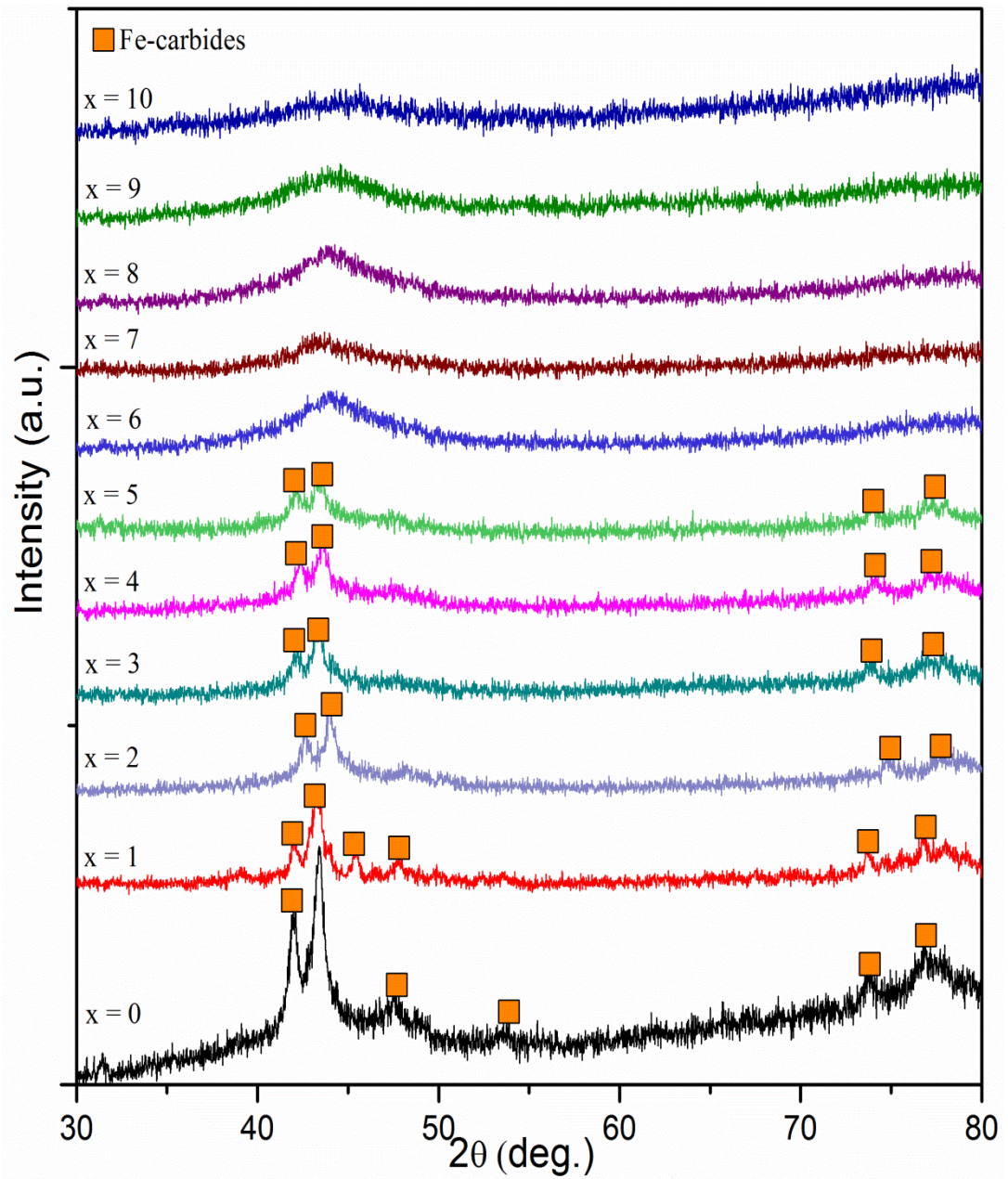


**Figure 5.2** XRD diffractogrammes of the  $M_{60}Cr_{13}Mo_{17-x}B_8Y_2Mn_x$  alloy system where  $x$  varies from 0 to 10.

First examinations conducted by XRD and their comparative results are given in Figure 5.2. The systems which contained Mn up to 5 at.% showed crystalline peaks which belongs to Fe-carbides in this analysis. However, as the content of the Mn increased among these samples, the intensities of these Fe-carbide peaks showed a decline. Moreover, some of the phases presented in base alloy became weaker and finally vanished in 5.at% addition of Mn. After that critical compositional limit, 6at.% to 10at.% Mn addition, the peaks detected were completely vanished and characteristic amorphous humps were obtained in the XRD analysis.

It is early to said that the optimum Mn composition lies between 6 to 10 at.%, nevertheless in accordance with macroexaminations of the samples and the XRD results, it would not be an incorrect hypothesis.

### **5.3. Effect of Mn Addition on Thermal Characteristics**

Thermal parameters and critical temperatures are one of the most effected aspects of BAS with alloying addition. Therefore, effect of microalloying of Mn to the base alloy should be investigated in detail. Same procedure with the previous sections was applied to the all alloy systems and the heating and the cooling curves are given in Figure 5.3, 5.4 and 5.5. In accordance with the heating thermogrammes of the samples, the crystallization temperatures were almost same up to 6.at% Mn addition. After that point, crystallization temperatures showed a great decline which could be interpreted as the alteration of the crystallization mode; in other words, the crystal product of this exothermic reaction was changed. While the  $T_x$  of the samples containing Mn up to 6at.% differ between 925 to 935K, the samples contained higher contents of Mn showed crystallization around 850-860K. These changes could be seen more detailed in Figure 5.4 which is the magnified view of Figure 5.3.

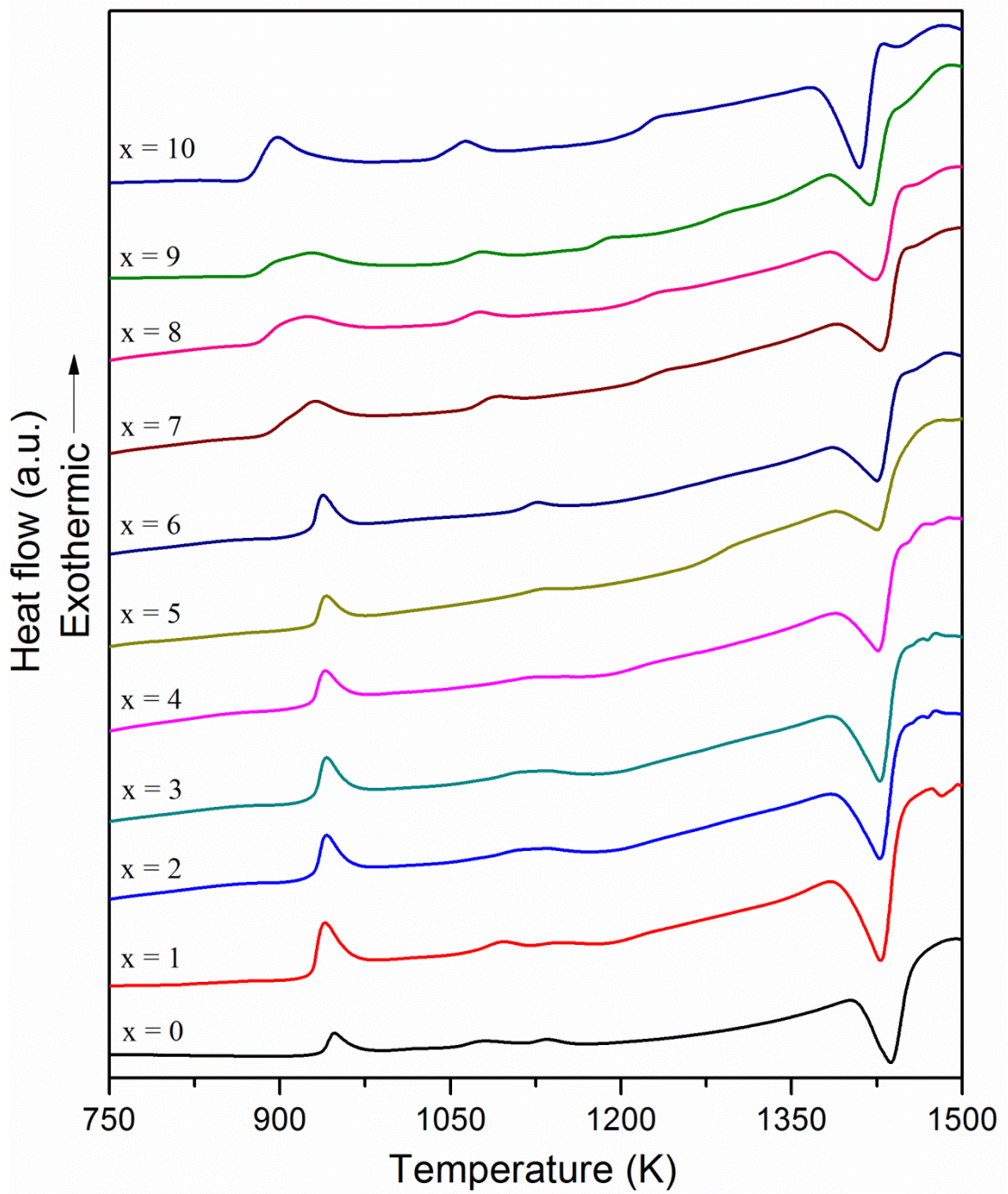


**Figure 5.3** Heating DSC thermogrammes of the  $M_{60}Cr_{13}Mo_{17-x}B_8Y_2Mn_x$  alloy system where  $x$  varies from 0 to 10

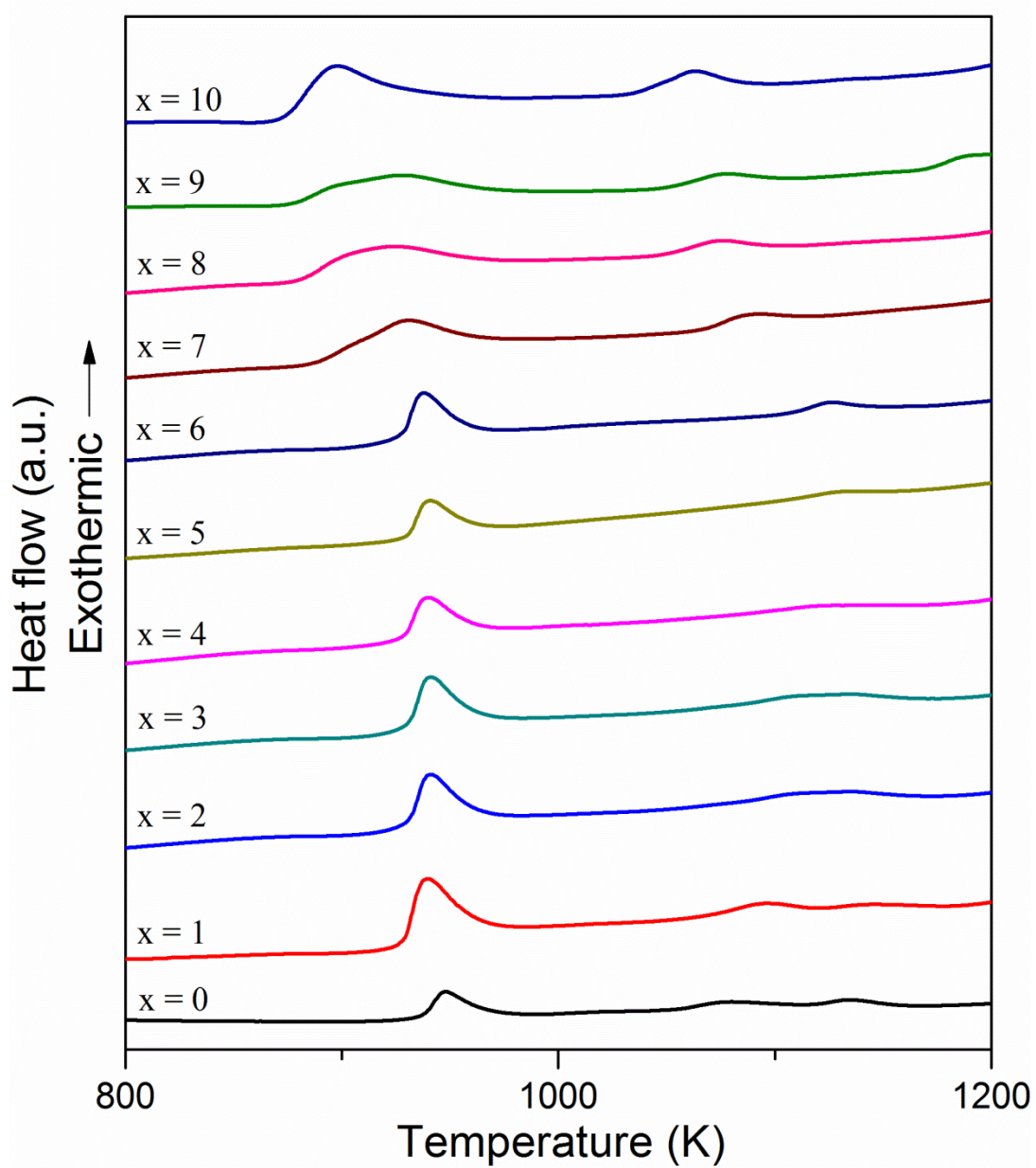


**Figure 5.4** Magnified view of heating DSC thermogrammes of the  $M_{60}Cr_{13}Mo_{17-x}B_8Y_2Mn_x$  alloy system where  $x$  varies from 0 to 10.

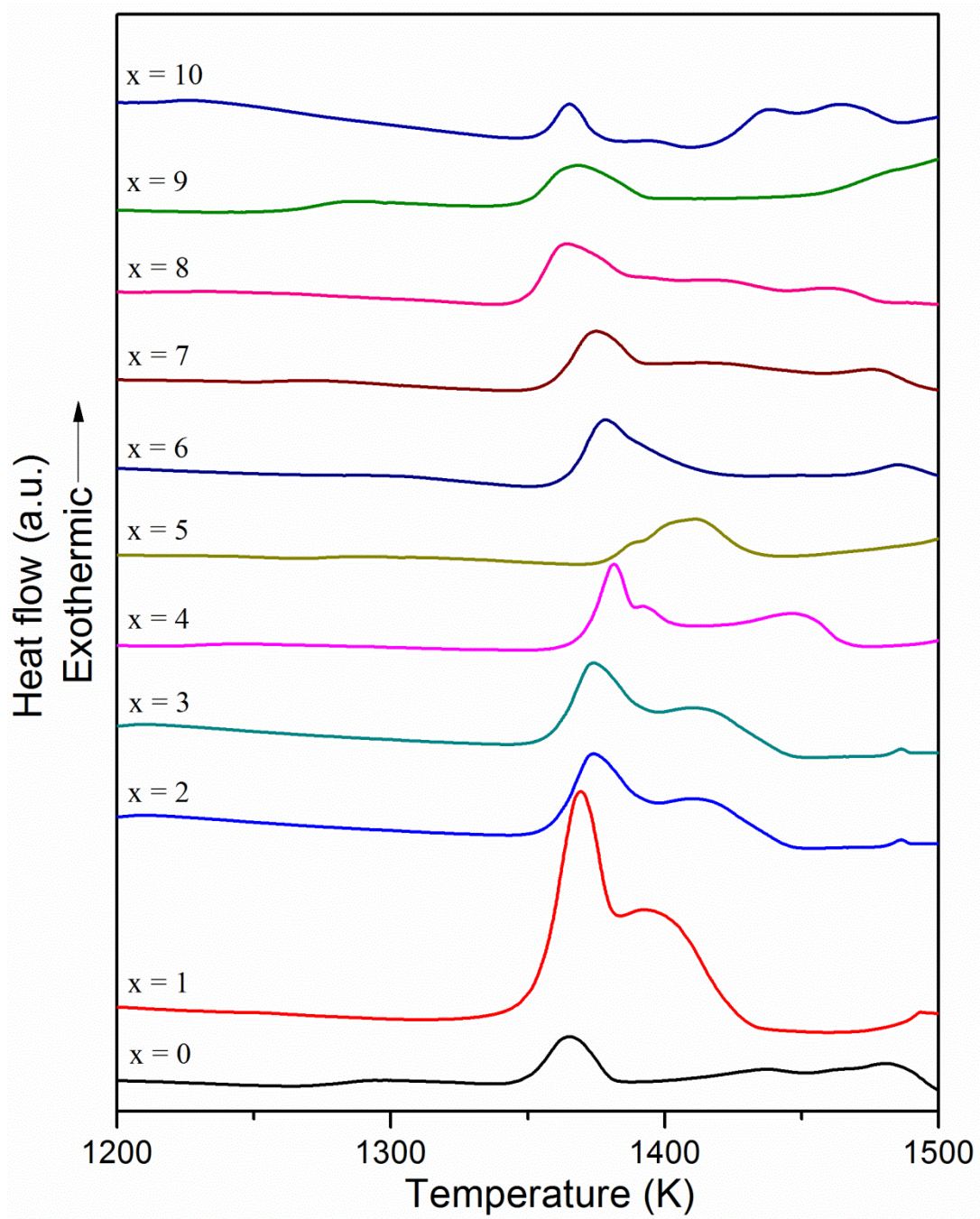


**Figure 5.5** First cycle of the cooling curves of the  $M_{60}Cr_{13}Mo_{17-x}B_8Y_2Mn_x$  alloy system where  $x$  varies from 0 to 10.

The glass transition trends of the samples were also changed with the addition of Mn. As the content of the Mn was increased,  $T_g$  showed a great improvement up to sample with 6at.% Mn in its composition. After this point,  $T_g$  began to reduce with a slower pace than 0-6at% Mn interval. Consequently, the reduction in the supercooled liquid region is a natural phenomenon in this case. Due to the increase in  $T_g$  and decrease in crystallization temperature, this liquid like behavior region became narrower. The variations of  $T_g$ ,  $T_x$  and  $\Delta T_x$  were summarized in Figure 5.6.

When the cooling thermogrammes were analyzed, all samples showed a melting temperature around 1350K. As this melting peak was observed in all samples, it could be labeled as eutectic temperature. This eutectic temperature was followed by a liquidus temperature according to the Figure 5.5. Because of the complexity of the composition, neither crystallization products nor the solidifying phase in eutectic reaction could be able to identified completely. It could be easily seen from the figure that with varying Mn content, these liquidus temperatures were also changed. Complete liquid form of the samples were observed at temperatures between 1400 and 1470K.

There is also variation of the cooling behavior of the samples from their equilibrium structures; however, this behavior was not investigated in detail in order not to change the scope of this study..

Critical temperatures of the microalloyed samples are given in Table 5.1.

**Table 5.1** Critical temperatures of the  $M_{60}Cr_{13}Mo_{17-x}B_8Y_2Mn_x$  alloy system where  $x$  varies from 0 to 10

Alloy	$T_g$ (K)	$T_{x1}$ (K)	$T_{x2}$ (K)	$T_l$ (K)	$\Delta T_x$ (K)
x = 0	818	936	1057	1456	118
x = 1	821	926	1066	1433	105
x = 2	846	928	1076	1439	82
x = 3	859	929	1087	1441	70
x = 4	861	927	1098	1457	66
x = 5	872	924	1110	1441	52
x = 6	875	925	1125	1432	50
x = 7	863	887	1065	1401	24
x = 8	855	879	1048	1397	24
x = 9	851	876	1049	1428	25
x = 10	849	874	1056	1467	25

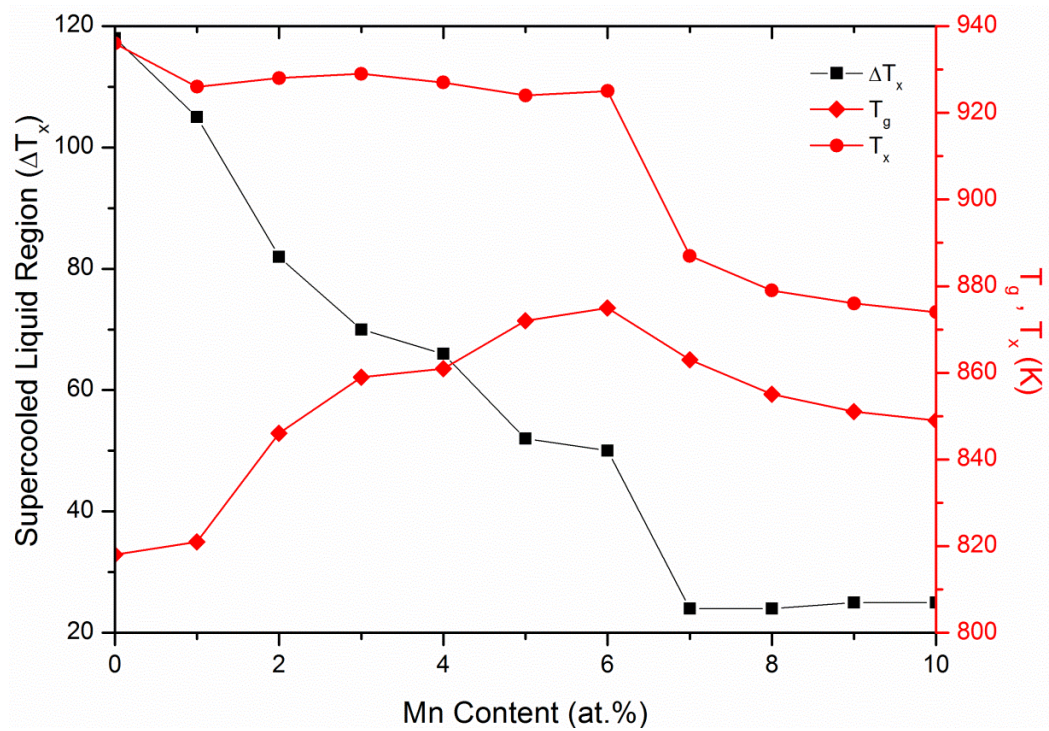


**Figure 5.6** Change of  $T_g$ ,  $T_x$  and  $\Delta T_x$  with Mn content of the base alloy

**Table 5.2** Glass forming ability parameters of the  $M_{60}Cr_{13}Mo_{17-x}B_8Y_2Mn_x$  alloy system where x varies from 0 to 10

<b>Alloy</b>	<b>T<sub>rg</sub></b>	<b>γ</b>	<b>γ<sub>m</sub></b>	<b>α</b>	<b>β</b>	<b>ω</b>
x = 0	0.562	0.412	0.724	0.643	1.706	0.154
x = 1	0.573	0.411	0.719	0.646	1.701	0.158
x = 2	0.588	0.406	0.702	0.645	1.685	0.171
x = 3	0.596	0.404	0.693	0.645	1.678	0.178
x = 4	0.591	0.400	0.682	0.636	1.668	0.186
x = 5	0.605	0.399	0.677	0.641	1.665	0.190
x = 6	0.611	0.401	0.681	0.646	1.668	0.187
x = 7	0.616	0.392	0.650	0.633	1.644	0.211
x = 8	0.612	0.390	0.646	0.629	1.640	0.213
x = 9	0.596	0.384	0.631	0.613	1.625	0.225
x = 10	0.579	0.377	0.613	0.596	1.608	0.238

The differences in the critical temperatures naturally affected the GFA parameters. Table 5.2 shows the values of the mentioned GFA parameters. When the Turnbull's criterion was considered, the best alloy with the highest GFA parameter was the sample with 7at.% addition of Mn. Due to the reduction of supercooled liquid region, highest GFA parameters were obtained from base alloy; however, prodigious differences were not observed in the other specimens.

Although the theoretical calculations of the GFA were not directly indicated the sample containing 7at.% Mn in its system, the experimental results showed that 7at.% addition of Mn gave the best results, amorphous phase was also observed even in the slowly cooled samples.

#### 5.4. Effect of Mn addition on Magnetic Properties

It was mentioned before that BASs should be non-ferromagnetic alloy systems. Furthermore, one should check the ferromagnetic behavior of the produced samples. In this study, the first examinations of the alloys were done by Fe-Nd-B magnet, and then these alloys were subjected to controlled magnetic field. According to the acquired magnetic response, hysteresis loops were generated.

B-H Loops of the produced samples can be seen in Figure 5.7 and more detailed loop can be seen in Figure 5.8 which is the magnified view of the 5.7. As it was mentioned before,  $M_{60}Cr_{13}Mo_{17-x}B_8Y_2Mn_x$  BAS systems contain  $x = 5$  or lower values had crystals in their structure. These crystals made alloy systems behave as ferromagnets. However, as the fraction of the crystals lowered in samples with higher Mn contents, the magnetic response also decreased and after critical composition, 6at.% Mn limit, the response became weaker and in the 7at.%Mn addition fully paramagnetic behavior was observed as expected. After that the optimum point, magnetic response again was gathered from the specimens.

All samples showed low  $M_s$  and  $M_r$  values in magnetic characterization. While the obtained  $M_s$  vary between 1 to 10 emu/gr in samples which contain crystal, after the critical limit  $x = 6$  at.% Mn, the best samples showed  $M_s$  lower than 1 emu/gr. Another important parameter,  $M_r$ , showed values lower than 1 emu/gr for all samples. With the reduction of all crystal fraction in the structure,  $M_r$  values also decreased and at the optimum value (7 at.% Mn) reached a value of almost zero which was another point to prove that this composition was completely paramagnetic. Another important parameter to understand the magnetic behavior of the samples is squareness which explains the shape of the hysteresis loops. The same trend obtained by remnant and saturation magnetizations was observed. While the squareness was 0.107 in base alloy, this value was decreased as the Mn contents of the systems were increased and showed no squareness in optimized 7.at.% Mn added composition. The variation of these parameters according to the content of Mn can be seen in Figure 5.9.

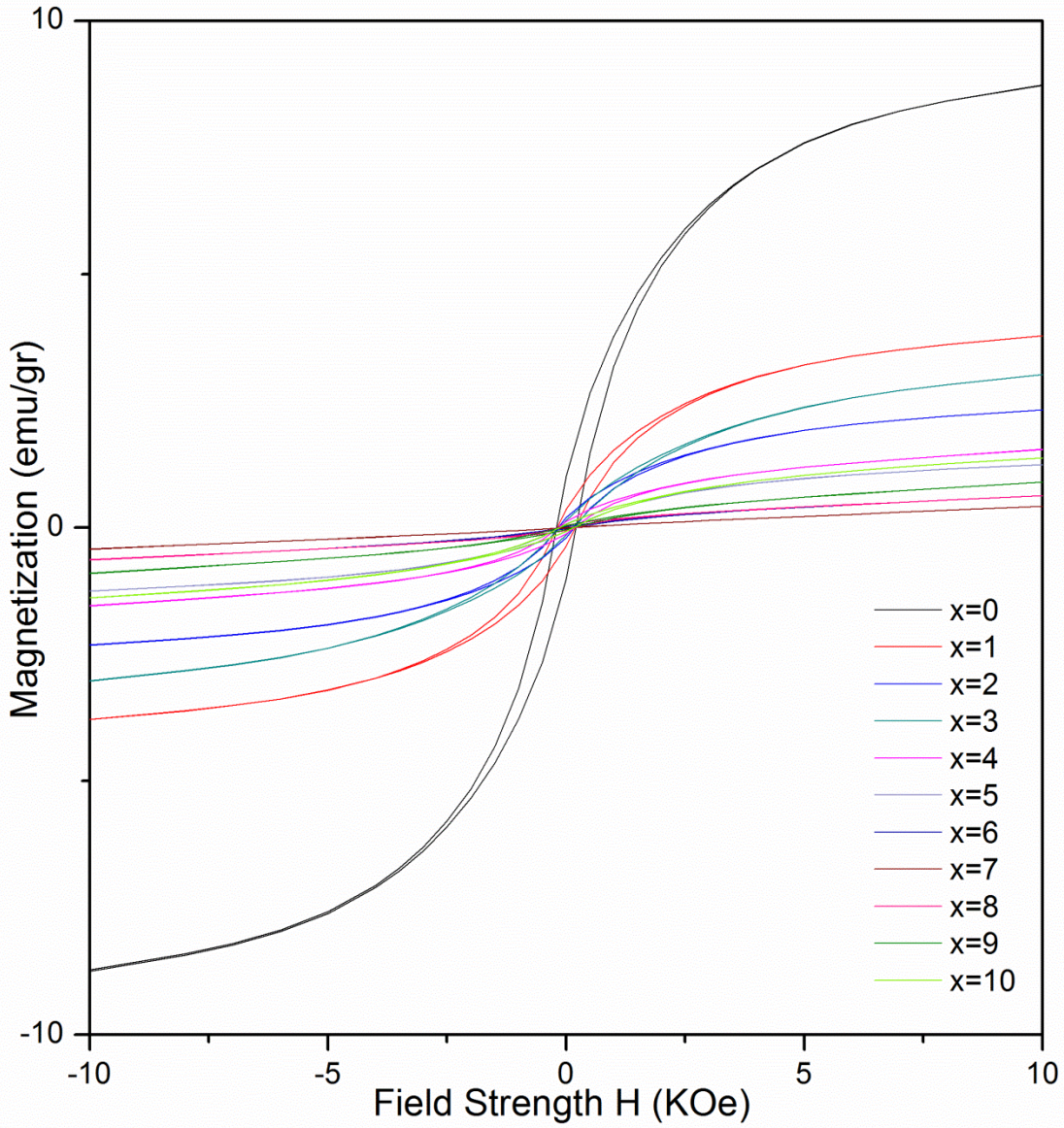


**Figure 5.7** Hysteresis loops of the  $M_{60}Cr_{13}Mo_{17-x}B_8Y_2Mn_x$  alloy system where x varies from 0 to 10

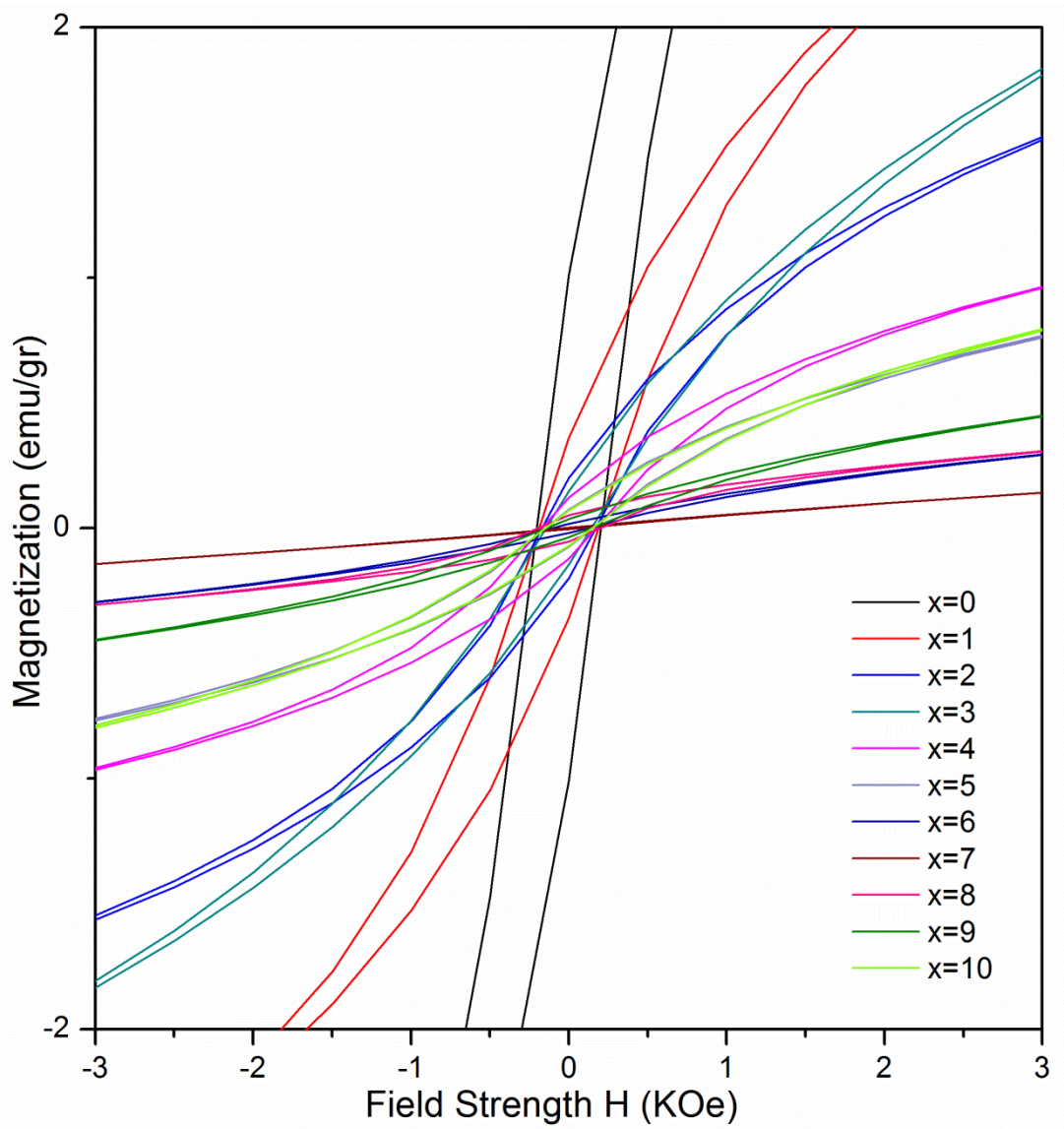


**Figure 5.8** Magnified view of the hysteresis loops of the  $M_{60}Cr_{13}Mo_{17-x}B_8Y_2Mn_x$  alloy system where x varies from 0 to 10

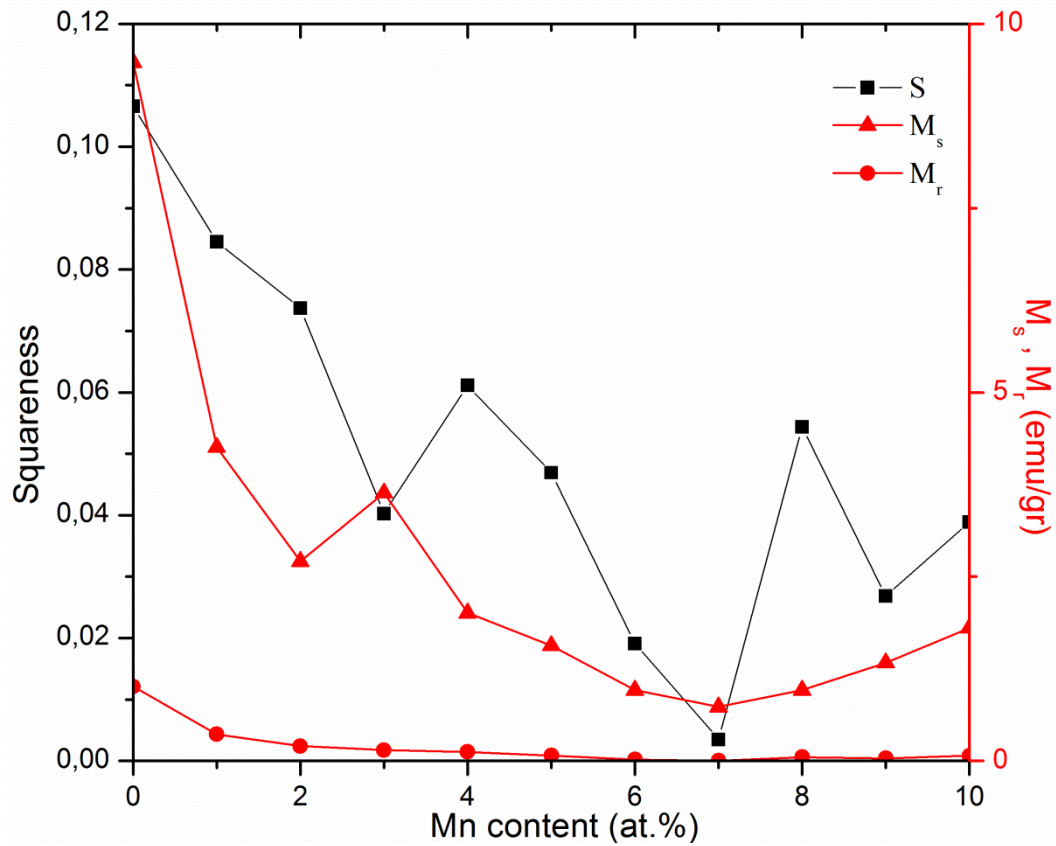


**Figure 5.9** Variation of the  $M_r$ ,  $M_s$  and the Squareness parameters with Mn content

### 5.5. Near Equilibrium Solidification and Microstructural Investigation

In order to support the fact that 7at.% Mn addition to the base alloy enhance the GFA, microstructural investigations were also conducted. Since the systems contained lots of constituent elements, alloying additions to the scrap cast iron and scrap cast iron itself, the complex crystal structures and the phases predicted to be observed. To investigate these complex phases presented in BAS alloy systems, heat treatment was applied. The reason is that the equilibrium structure of the alloy systems also indicates the stability of both liquid and the crystal phases. Representative and critical alloy compositions were chosen for equilibrium microstructure examination.

$M_{60}Cr_{13}Mo_{17}B_8Y_2$  (base alloy) and  $M_{60}Cr_{13}Mo_{17-x}B_8Y_2Mn_x$  alloy systems where  $x=3, 7, 10$  were subjected to heating in controlled Ar atmosphere. The temperature increased around 1500K where all alloys were liquefied and left in the furnace for furnace cooling.

These slowly cooled samples first were examined with XRD to determine the phases and the changes in the phases with addition of Mn. Then the remaining samples were mounted and prepared for the metallographic investigations. Figure 5.10 shows the data obtained from XRD.

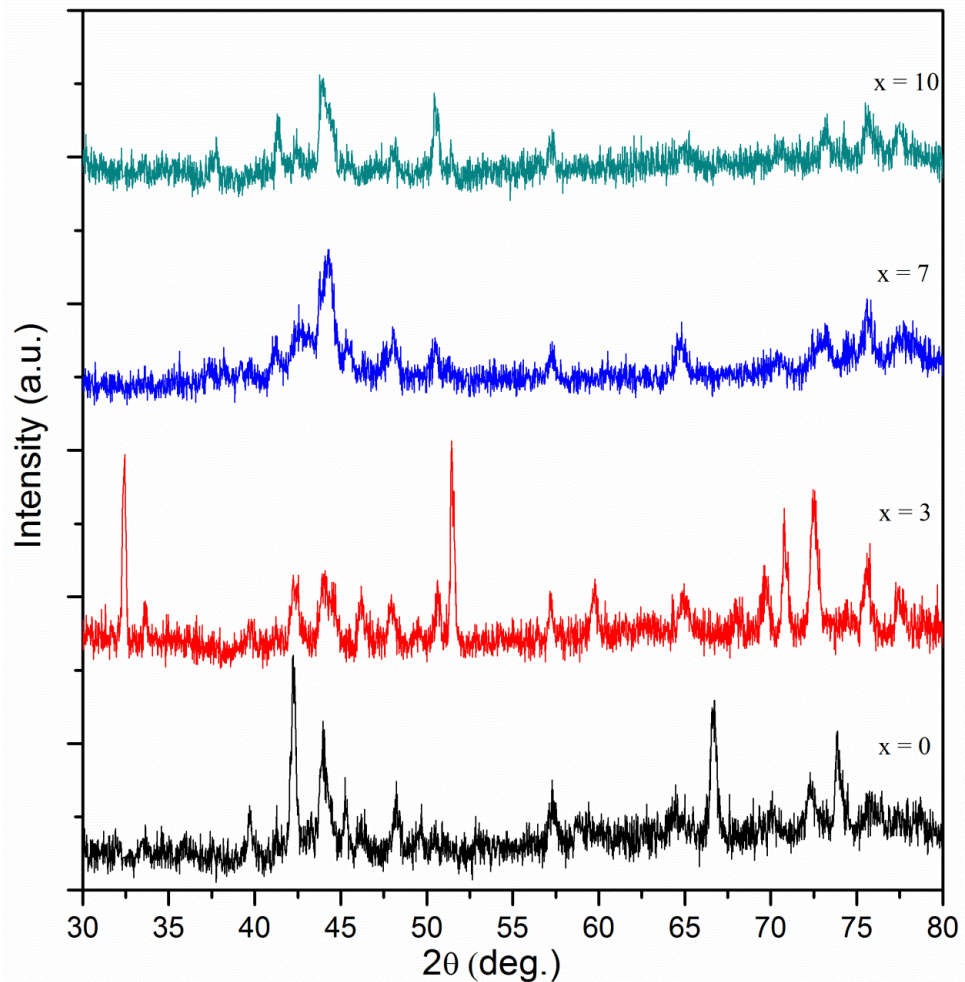


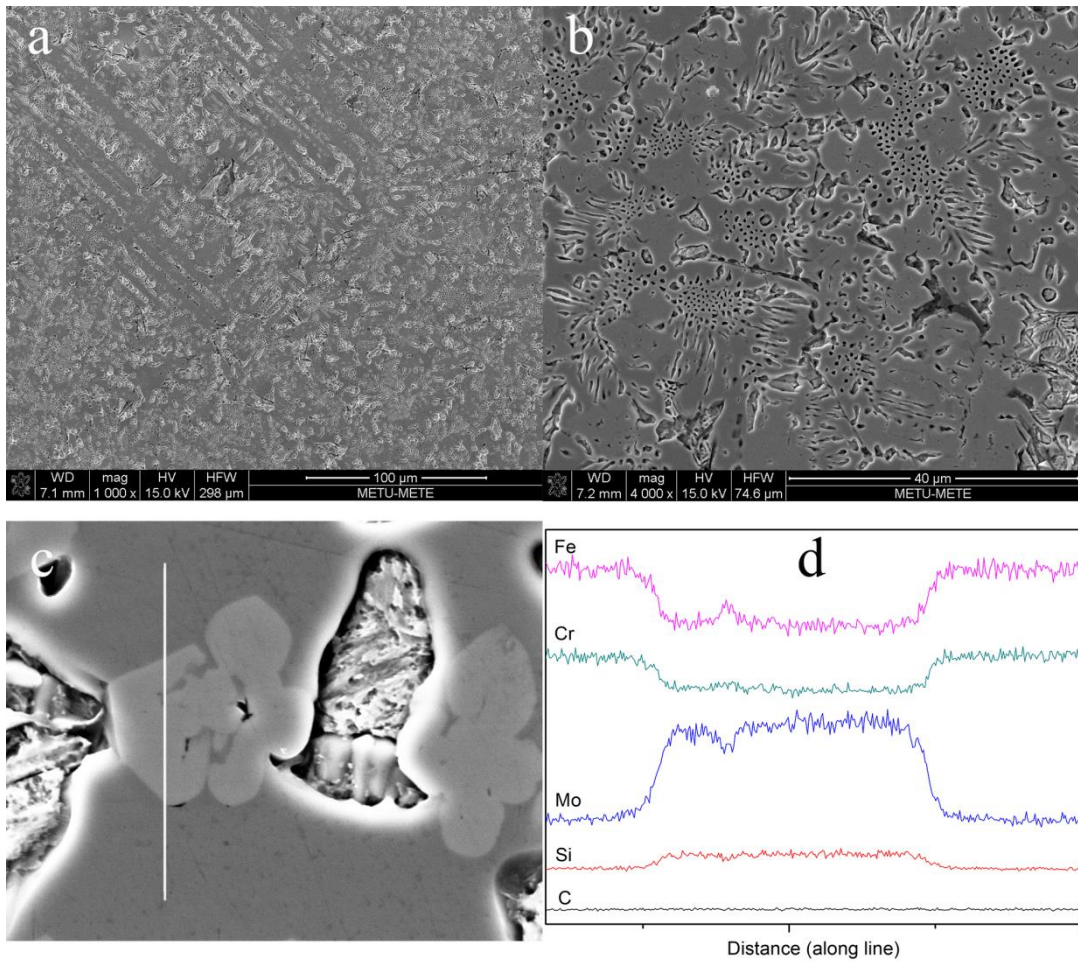
**Figure 5.10** XRD diffractograms of heat treated  $M_{60}Cr_{13}Mo_{17}B_8Y_2$  (base alloy) and  $M_{60}Cr_{13}Mo_{17-x}B_8Y_2Mn_x$  alloy systems where  $x=3, 7, 10$

The phases presented in given diffractogrammes could not be clearly identified. However, some candidate phases were specified. The possible phases presented in these specimens were  $\alpha$ -Fe,  $\gamma$ -Fe,  $\text{Cr}_{0.49}\text{Fe}_{0.51}$ ,  $\text{Mo}_3\text{Si}$ ,  $\text{Mo}_5\text{Si}_3$ ,  $\text{Mo}_{0.5}\text{Fe}_{0.3}\text{Si}_{0.2}$  and  $\text{Mo}_3\text{Fe}_3\text{C}$ . Due to these complex phases, the peaks obtained from the diffraction data could not be labeled.

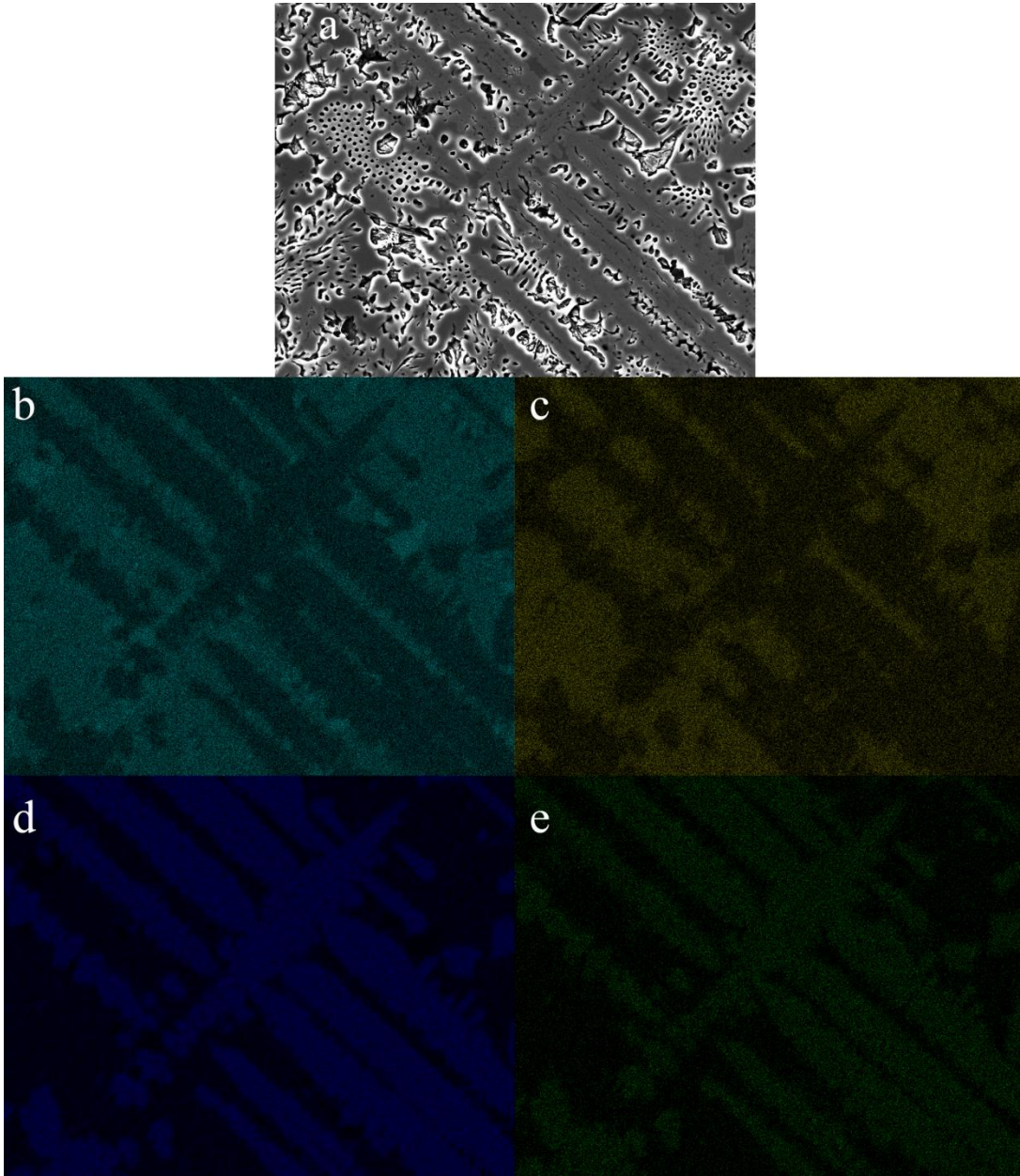
Furthermore, the phases were presented in base alloy maintain their existence in 3at.% Mn addition. However when the 7at.% Mn added sample and the further additions were investigated, some of the presented phases in base alloy were disappeared. In other words, structures of the BAS systems were simplified. The simplification of the solidification mechanisms indicated that liquid was fewer tendencies to form crystal structure. It was shown before the existence of eutectic and peritectic points in the system stabilizes the liquid than the solid [25, 89]. With the purpose of ascertain the change in microstructure observed in the XRD analysis, samples investigated with SEM. To determine the phases, line EDS scans and EDS mappings were applied.

Figure 5.11 revealed the microstructure of the base alloy comprises a eutectic phase mixture with two phase matrix. These phases could not be identified completely; however, EDS scans showed that this two phase matrix were consisted of generally Fe-Cr rich but there were Mo-Si rich areas on this Fe-Cr rich matrix. In accordance with Figure 5.11 (c) and (d), the darker areas were richer in terms of Fe and Cr while lighter zones on the matrix involved higher Mo and Si content. Figure 5.12 showed that Mo-Si rich zones placed between eutectics while Fe-Cr regions were found near eutectics. These Mo-Si zones might also be faceted intermetallic phases.

The transformation mechanism was unclear; yet it is assumed that the transformation could be actualized according to the quaternary phase diagram of the mentioned elements.



**Figure 5.11** Microstructural investigation of the heat treated base alloy system ( $M_{60}Cr_{13}Mo_{17}B_8Y_2$ ). a) SEM micrograph at 1000 magnification b) SEM micrograph at 4000 magnification c) EDS line scan zone of base alloy d) line scan results of the micrograph (c)



**Figure 5.12** EDS mapping observations of the base alloy a) Mapping micrograph of base alloy and results according to b) Fe, c) Cr, d) Mo, e) Si

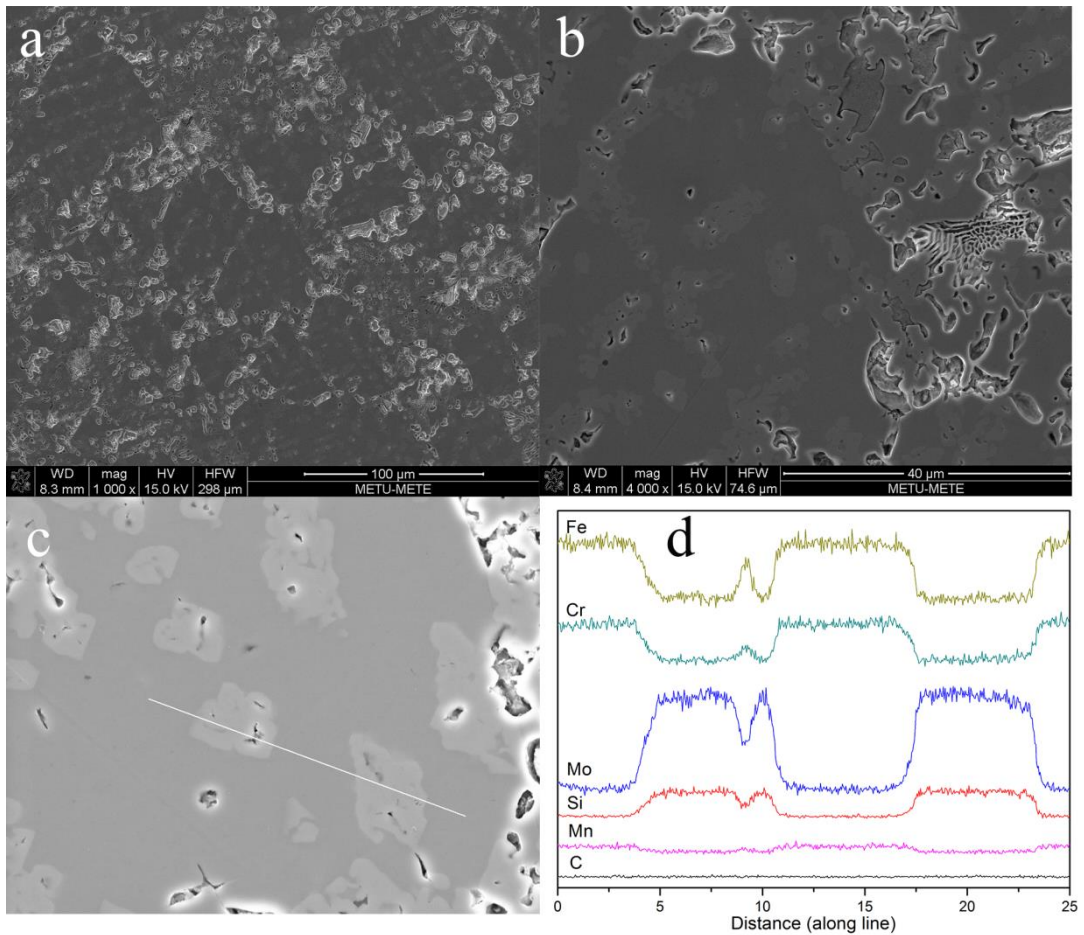


**Figure 5.13** Microstructural investigation of the heat treated 3at% Mn added system ( $M_{60}Cr_{13}Mo_{17}B_8Y_2Mn_3$ ). a) SEM micrograph at 1000 magnification b) SEM micrograph at 4000 magnification c) EDS line scan zone of base alloy d) line scan results of the micrograph (c).

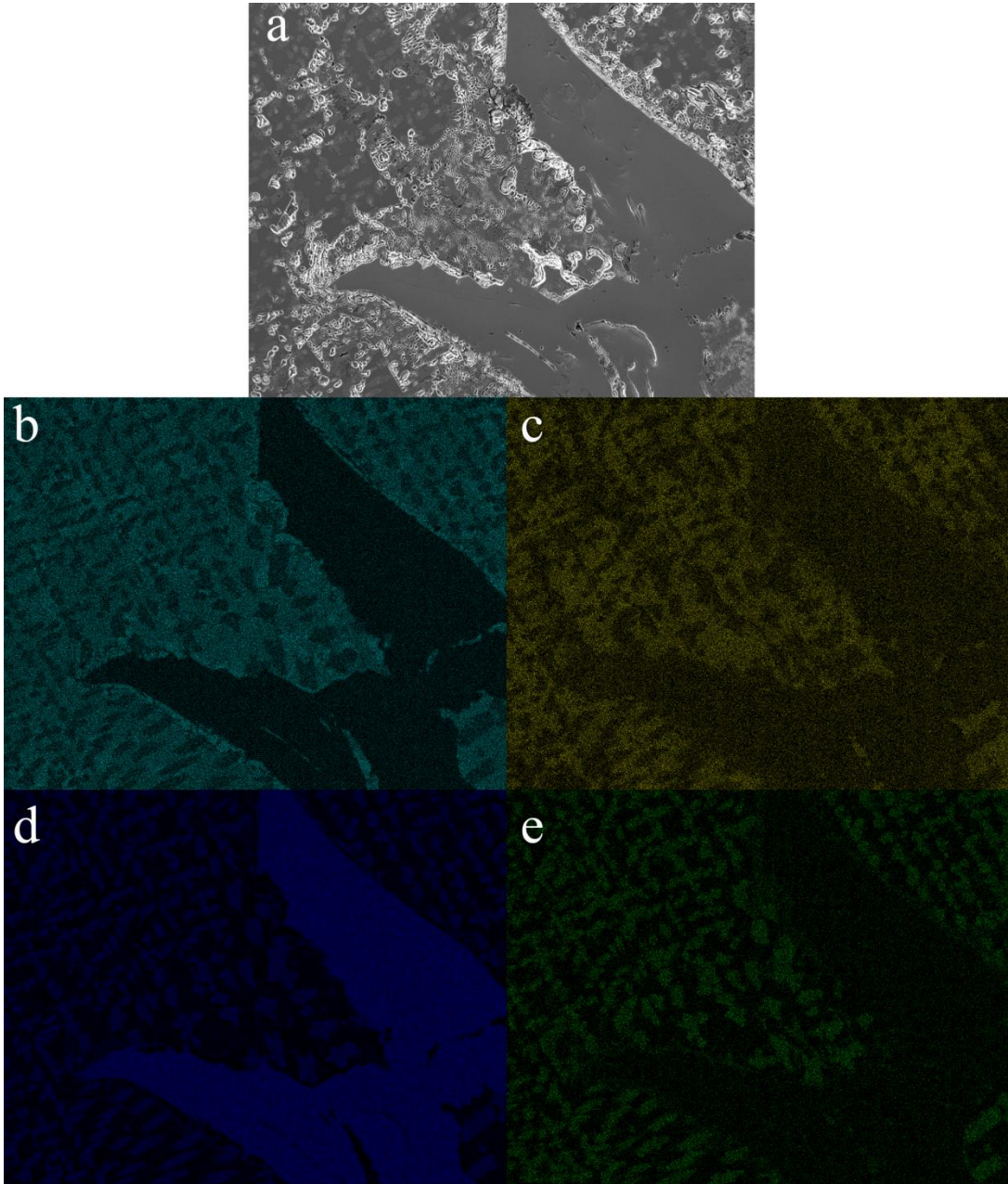


**Figure 5.14** EDS mapping observations of the system containing 3at.% Mn  
a) Mapping micrograph of base alloy and results according to b) Fe, c) Cr, d) Mo, e)  
Si

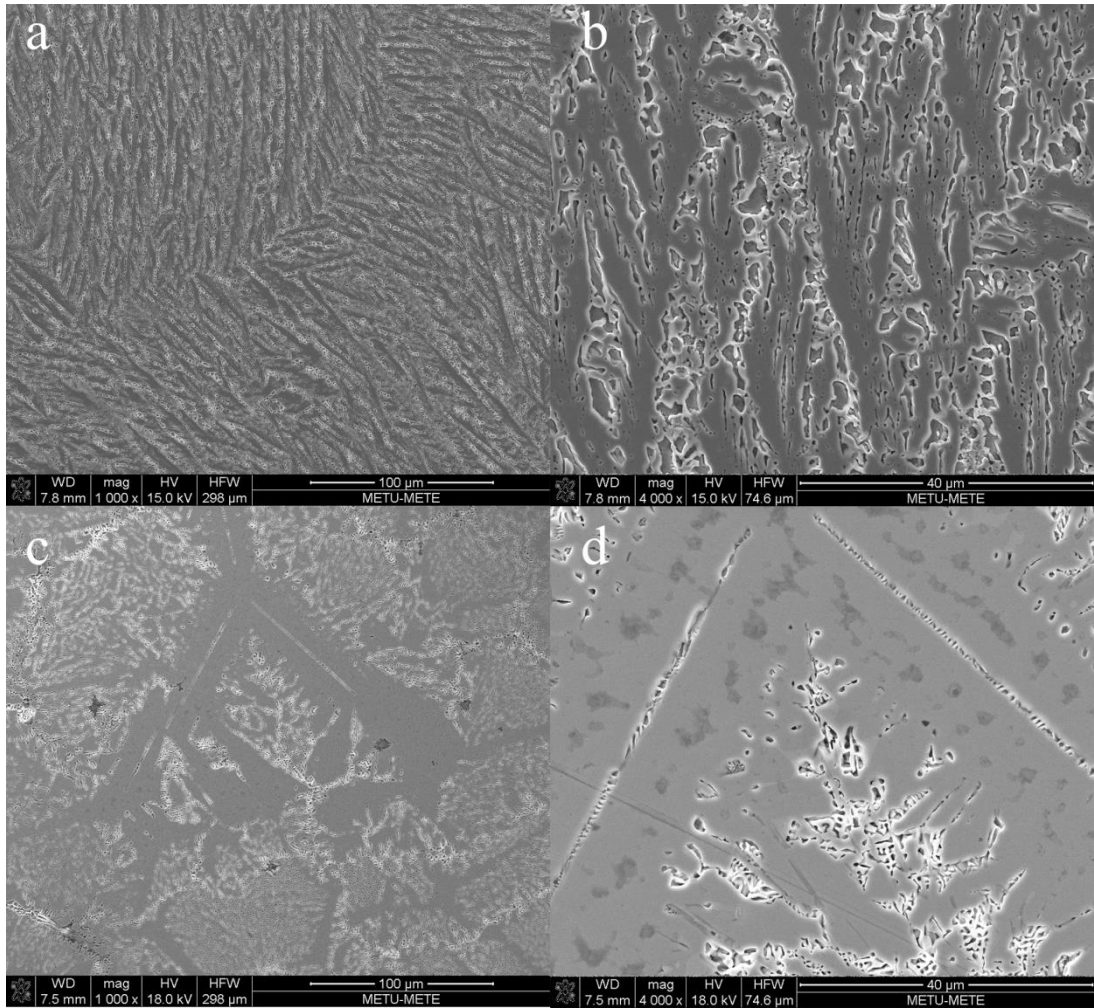


**Figure 5.15** SEM micrographs of system containing 7 at.% Mn a) 1000 magnification b) 4000 magnification and system containing 10at.% Mn c) 1000 magnification d) 4000 magnification

Addition of 3at.% Mn to the base alloy did not affect the microstructure. The same structures observed in base alloy were also spotted in this BAS system. The eutectic phase mixture and the two phase matrix were again observed and the EDS showed that obtained results were almost same. Line scan results in Figure 5.13 proved that the lighter colored part of the matrix involves higher Mo and Si content as it mentioned. Figure 5.14 also shows the faceted intermetallic phases which were comprised high contents of Mo in their structure. These mentioned systems, base alloy and 3at.% Mn addition to it, were consisted of high complexity structures.

The equilibrium microstructures of systems containing 7 and 10at% Mn in their compositions are given in Figure 5.15. Although they contain eutectic phase mixture as other specimens, the mentioned phase change in matrix was not encountered in SEM analysis.

In Figure 5.15 (a), system which claimed to be the best glass former among other samples, 7at.% Mn addition to the base alloy, is presented. According to the SEM micrographs and EDS line and mapping analysis, this sample showed only eutectic structure. Matrix did not involve two phases, as it can be seen there was a uniform matrix in this specimen.

In Figure 5.15 (b), the micrographs of the system with 10at.% Mn content can be seen. As it can be seen from the figure, eutectic phase mixture was again observed in the micrographs. Although it seem like there were two matrix phases in the structure, EDS results proved that the dark regions on the images were only etch stains. There is no difference in elemental analysis between dark and bright regions. Despite the fact that, addition of Mn 7 and 10 at.% to the base alloy gave similar results in EDS, the microstructures of these samples showed great difference.

The important point of this analysis is that, as the Mn content of the system increased up to 7at.% Mn limit, the complex to simple microstructural transition was observed. As mentioned before, as microstructures became simpler, the stabilization of the liquid became easier. In the light of this information, one could assume that,

7at.% Mn addition to the base alloy showed the simplest microstructure with respect to both XRD and SEM analysis and this composition had the highest GFA.

### 5.6. Effect of Mn addition on Mechanical Properties

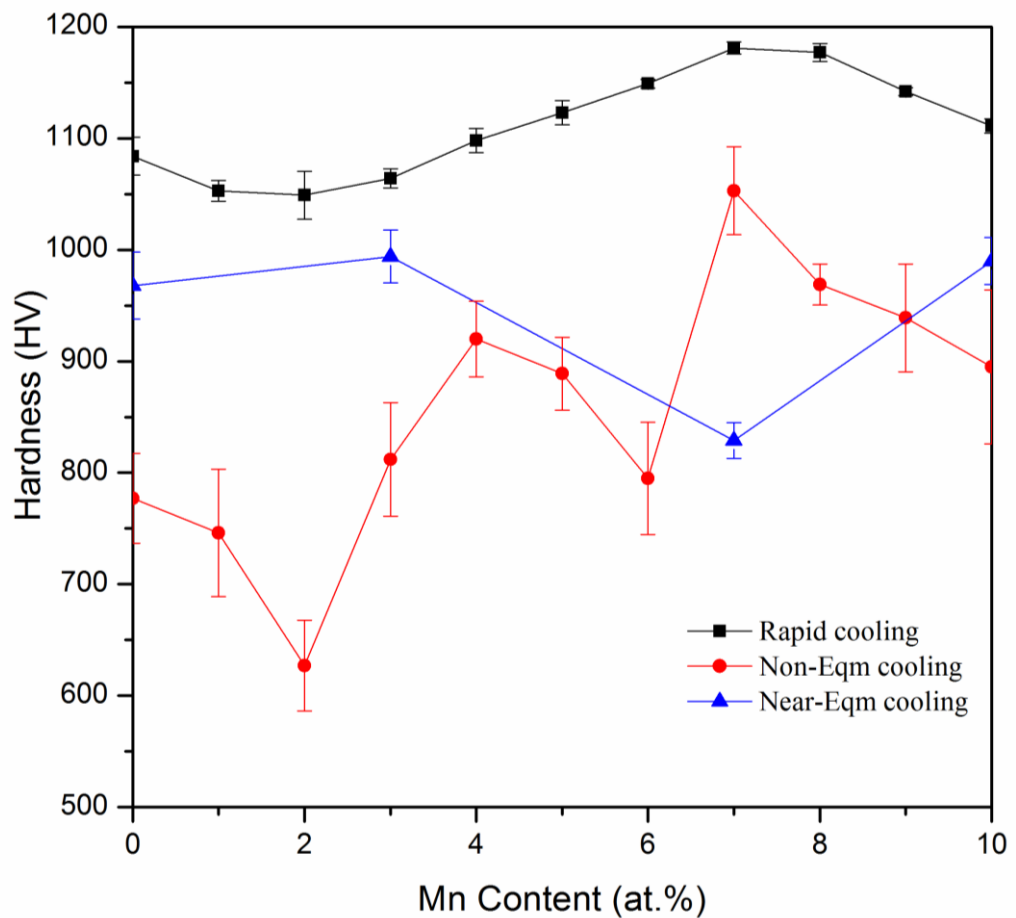


**Figure 5.16** Hardness distributions with respect to Mn content of the system of heat treated, as-cast and rapidly cooled specimens

Figure 5.16 shows the hardness distribution with respect to the Mn content of the systems. As it is expected, rapidly solidified samples had the highest hardness values among other specimens. According to the figure, specimens with partially crystalline structures showed lower hardness values than the full amorphous samples. Moreover, as the fraction of the amorphous structure increased, the homogeneity of

the sample surface is also increased, which resulted in low errors in these samples. However, addition of Mn had not a high influence on hardness of the samples. The values vary between 1050 and 1180 HV.

When the as-cast samples were investigated, it could be seen that the sample containing 7 at.% Mn had the highest hardness values among others. This is because the mentioned sample involved amorphous phases in the matrix even in as-cast form. Therefore, the hardness value as high as 1050HV was reached. In addition, the samples which could form fully amorphous structures showed higher hardness than the specimens which could not reach fully glassy phase. Because of the non-equilibrium condition of the specimens, high errors were obtained.

Interesting results were obtained from the heat treated samples of the synthesized BAS samples. As it can be seen from Figure 5.16, contrary to the expectations, the heat treated samples showed higher hardness values than the non-equilibrium cooled specimens. The hardness of the samples strongly depends on the volume fraction and the size of the existing phases. Although the reason behind this situation is still unclear, two assumptions might be appropriate:

- The phase with low hardness might be transformed to the high hardness phase via unclear phase transformation during heat treatment [104].
- Nucleated high hardness phase might grow during the heat treatment and dominate the structure of the samples.

Furthermore, as it was discussed in the previous section, only the sample containing 7at.% Mn in its composition showed simple microstructure. This simplicity of the microstructure was the origin of the low hardness values among the other heat treated specimens. In addition, because of the homogeneous distribution of the microstructures of the heat treated samples, relatively low error values were obtained.

## 5.7. Identifying the best Alloy System

In the previous chapter, it was discussed and specified that the best alloying addition to the  $M_{60}Cr_{13}Mo_{17}B_8Y_2$  BAS composition was Mn. With the addition of Mn, fully glassy phase was obtained with enhanced thermal and magnetic characteristics. In this chapter, the effects of Mn on various properties of BASs were investigated via microalloying technique. Analysis of the obtained results from various characterization methods indicated that the best amount of Mn addition with the same amount of subtraction of Mo was found to be 7 at.%. In this section, detailed investigations were performed.

### 5.7.1. Critical Temperatures and Glass Forming Ability

Considering the previous studies on amorphous steels,  $M_{60}Cr_{13}Mo_{10}B_8Y_2Mn_7$  samples showed unexpected performance in terms of thermal characteristics. For instance, when the production from pure constituent elements were the case according to the Fang et. al. study [75],  $Fe_{44}Cr_{10}Mo_{12.5}Mn_{11}C_{15}B_6Y_{1.5}$  samples showed a  $T_g$  around 866K with  $\Delta T_x \sim 50K$ , on the other hand when the industrial constituent additions were considered, according to a recent study by Tsai et. al.[66],  $Fe_{41}Cr_{15}Mo_{14}C_{(21-x)}B_xY_2Co_7$  ( $x=5-10$ ) samples showed  $T_g$  between  $\sim 783-833K$  with  $\Delta T_x \sim 55-80K$ .  $M_{60}Cr_{13}Mo_{10}B_8Y_2Mn_7$  samples had one of the highest  $T_g$  with expected  $\Delta T_x$  which is 863K and 25K respectively.

This sample also showed high GFA parameters. The highest  $T_{rg}$  among all Mn additions had achieved with addition of 7at.% Mn to the base alloy. Furthermore, this specimen showed great performance with respect to the other GFA parameters. All critical temperatures of amorphous alloys and various GFA parameters can be found in Table 5.3.

**Table 5.3** Critical temperatures and GFA parameters of the  $M_{60}Cr_{13}Mo_{10}B_8Y_2Mn_7$  BASs

$M_{60}Cr_{13}Mo_{10}B_8Y_2Mn_7$	
$T_g$ (K)	863
$T_x$ (K)	887
$\Delta T_x$ (K)	24
$T_{rg}$	0.616
$\gamma$	0.392
$\gamma_m$	0.650
$\alpha$	0.633
$\beta$	1.644
$\omega$	0.211

### 5.7.2. Crystallization Kinetics

Crystallization kinetics is also an important aspect to reach GFA and the mechanism behind the phase transformations. To investigate the thermal characteristics further and characterize alloy in detail kinetics must be comprehended. However, there are insufficient studies about the crystallization kinetics of bulk amorphous steels. This is another fact to motivate to examine the synthesized sample in isochronal condition.

For this purpose two different approaches were applied. DSC scans with different heating rates were compared. According to these results, as the heating rate is increased, increase in the sensitivity of the thermogrammes was observed with shift in peaks. These shifts were taken into account in Kissinger and Ozawa approaches to the isochronal crystallization kinetics. In the case of high heating rates such as, 99 K/s, 80 K/s and 60 K/s, curves did not follow the shifting trends; as a result, these rates were not taken into consideration.

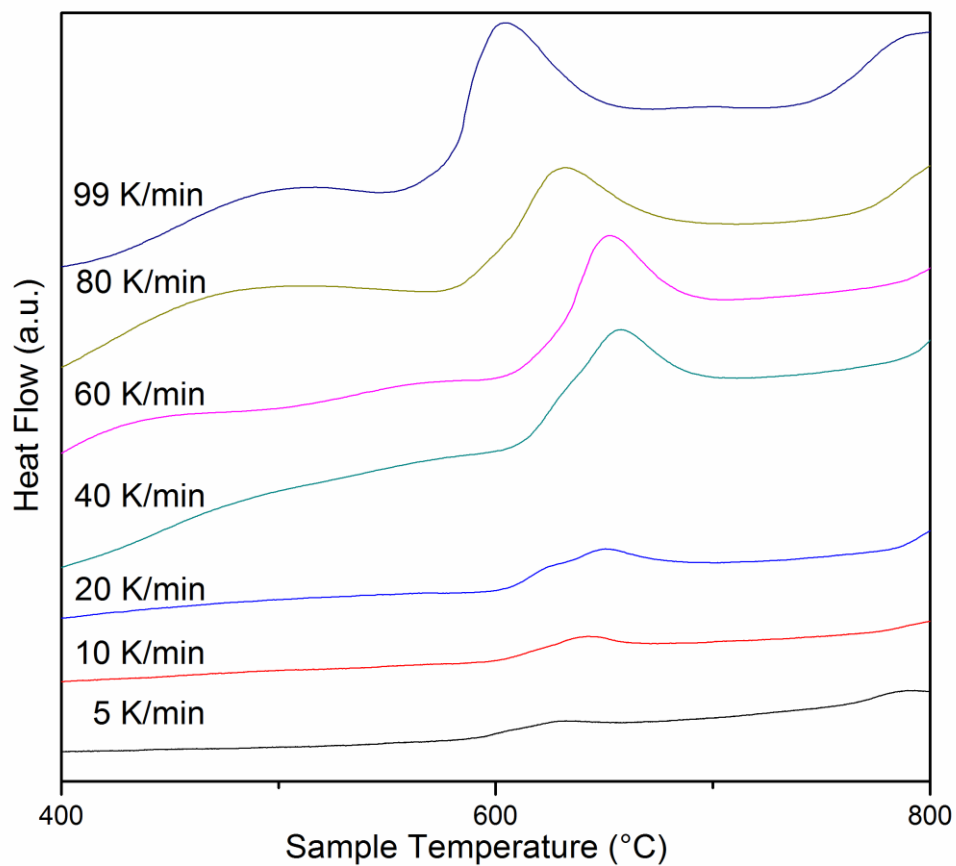


**Figure 5.17** DSC thermogrammes of heating rates of 5 K/min up to 99 K/min

**Table 5.4** Critical temperatures at 5 K/min, 10 K/min, 20 K/min and 40 K/min

Scan Rate (K/min)	$T_g$ (K)	$T_x$ (K)	$T_p$ (K)
5	838	860	900
10	846	868	911
20	852	876	919
40	862	886	928

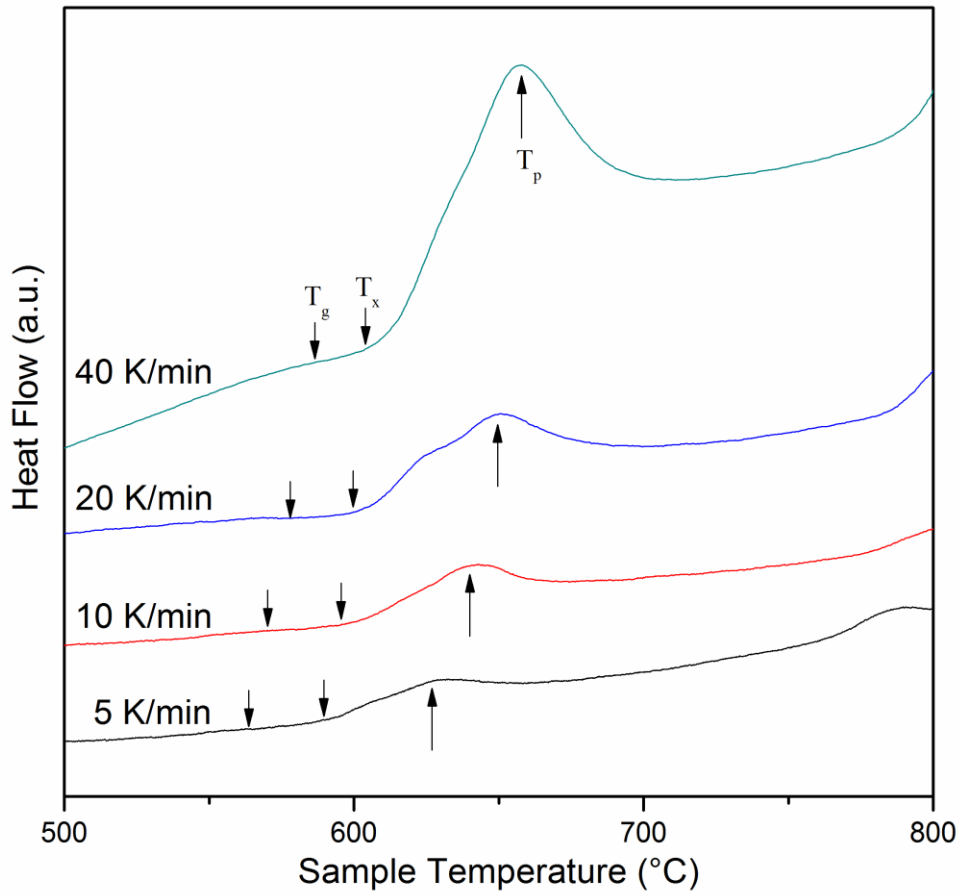


**Figure 5.18** DSC thermogrammes of heating rates of 5 K/min up to 40 K/min

According to the obtained values of  $T_g$  and  $T_p$ , given in Table 5.4, Kissinger plots were constituted. From the slope of these plots activation energy which indicates the energy barrier that atoms should overcome to change their present structures were calculated.

These Kissinger plots can be seen in Figure 5.19 and the calculated activation energies for glass transition and crystallization can be seen in Table 5.5.

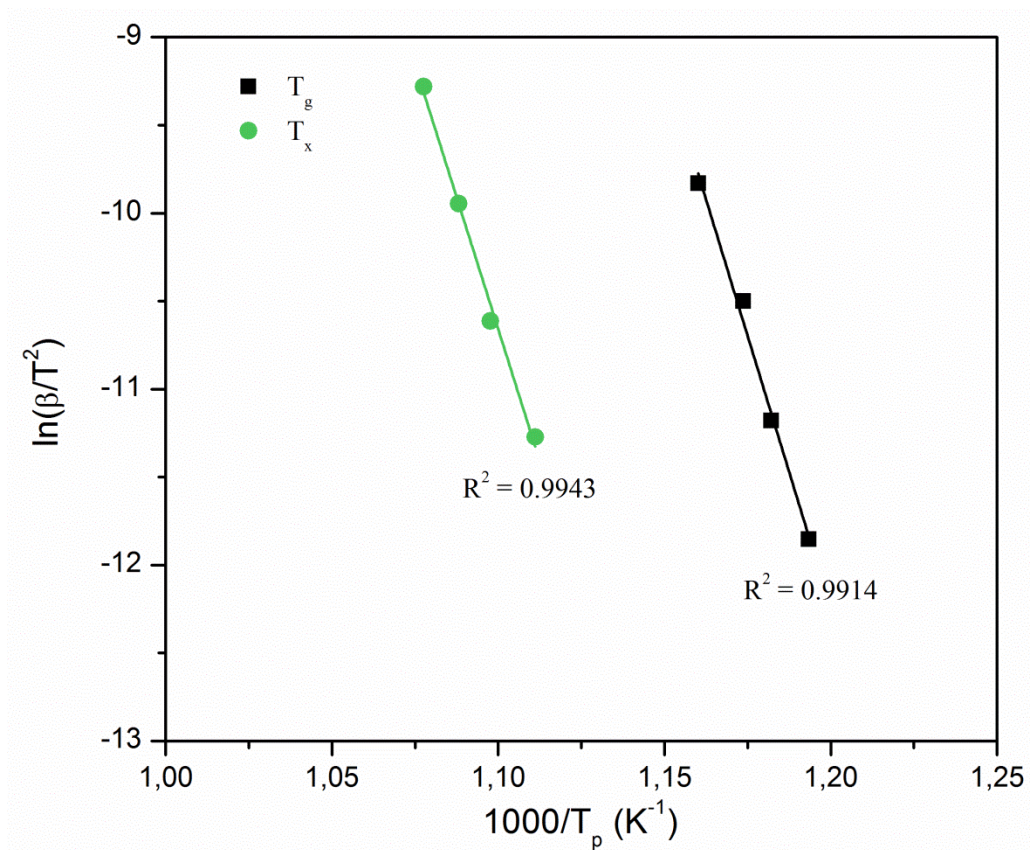


**Figure 5.19** Kissinger plot of  $M_{60}Cr_{13}Mo_{10}B_8Y_2Mn_7$  bulk amorphous steel

**Table 5.5** Activation energies for glass transition and crystallization calculated from Kissinger plots

Transition	Activation Energy (kJ/mol)
Glass transition	515.2
Crystallization	498.8

Extremely high values of the activation energy barrier for glass transition and relatively lower activation energy for crystallization showed that BAS composition,  $M_{60}Cr_{13}Mo_{10}B_8Y_2Mn_7$ , had a high thermally stable amorphous nature.

To confirm the results obtained from Kissinger approach, Ozawa method was also applied to the mentioned BAS system. The agreement between these two approaches showed that calculated activation energy values were consistent.

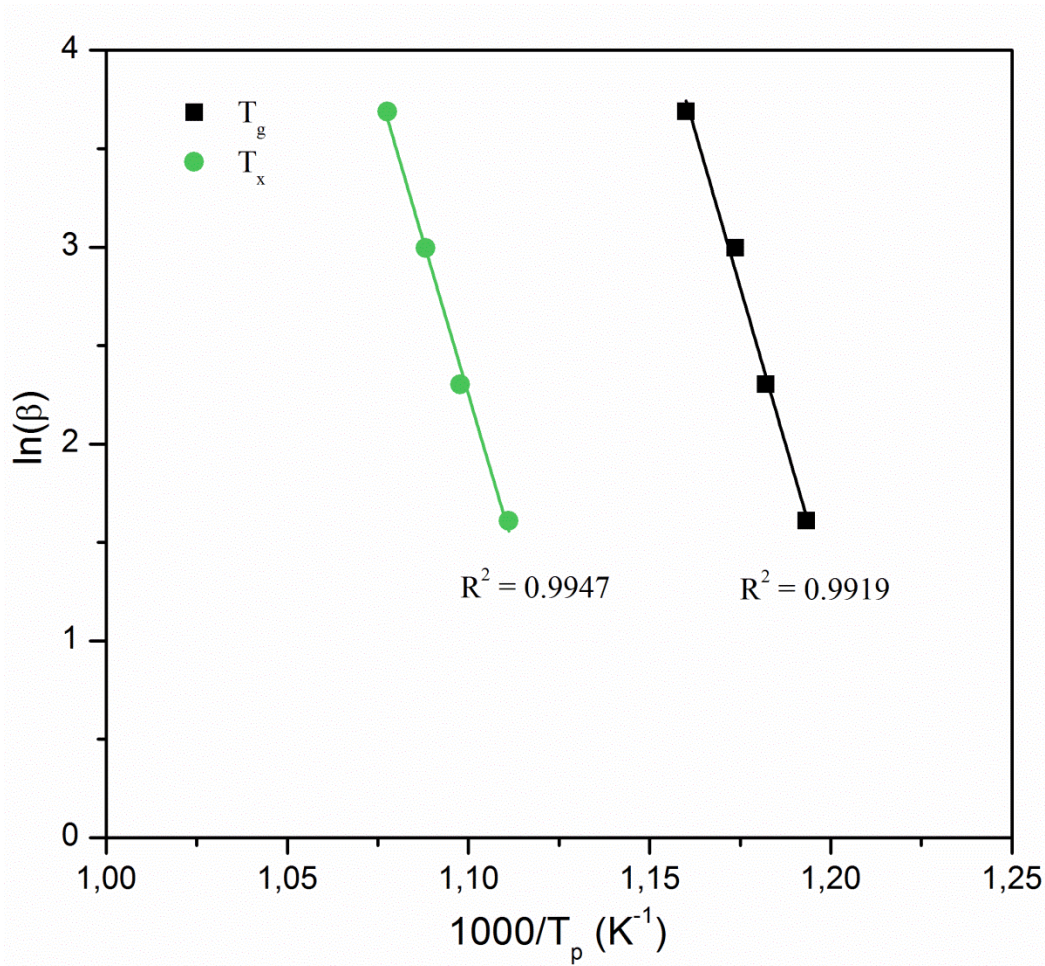


**Figure 5.20** Ozawa plot of  $M_{60}Cr_{13}Mo_{10}B_8Y_2Mn_7$  bulk amorphous steel

**Table 5.6** Activation energies for glass transition and crystallization calculated from Kissinger plots

Transition	Activation Energy (kJ/mol)
Glass transition	529.3
Crystallization	503.9

Barandiaran-Colmenero approach [98] was also used to determine the critical cooling rate for bypassing the nucleation. In this approach, thermogrammes with 5 K/min, 10 K/min and 20 K/min were used to calculate the critical cooling rate.

**Table 5.7** Critical temperatures at different heating rates

Scanning Rate (K/min)	T <sub>l</sub> (K)	T <sub>xc</sub> (K)
5	1400	1385
10	1399	1378
20	1400	1371

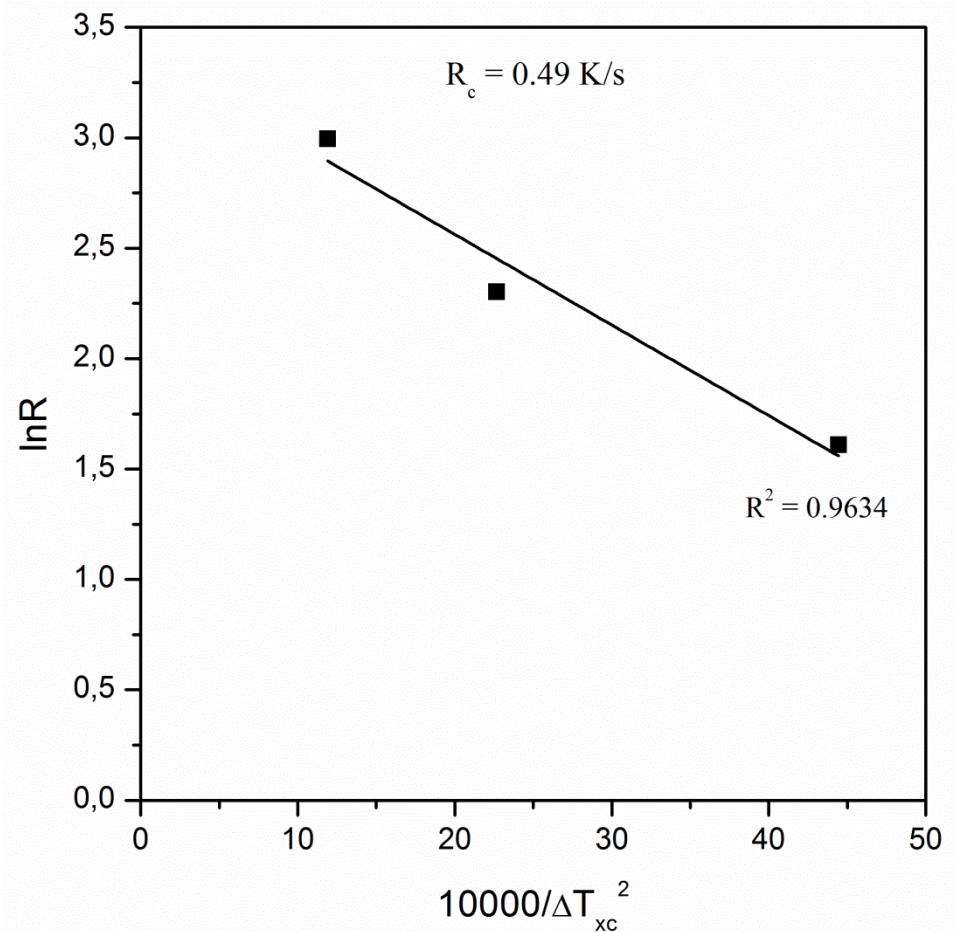


**Figure 5.21** Barandiaran-Colmenero plot of M<sub>60</sub>Cr<sub>13</sub>Mo<sub>10</sub>B<sub>8</sub>Y<sub>2</sub>Mn<sub>7</sub> BAS sample

From the values given in Table 5.7,  $\ln R$  vs  $10000/\Delta T_{xc}^2$  plot was constructed. According to this plot, the intersection point of the line at  $\ln R$  axis gave the natural logarithm of the critical cooling rate.  $R_c$  was calculated as 0.49 K/s which is exceptionally low when the case was Fe-based bulk amorphous alloys. This low  $R_c$  showed that  $M_{60}Cr_{13}Mo_{10}B_8Y_2Mn_7$  is an easy glass forming alloy system.

With same manner necessity of cooling rate for eutectic suppression was calculated.

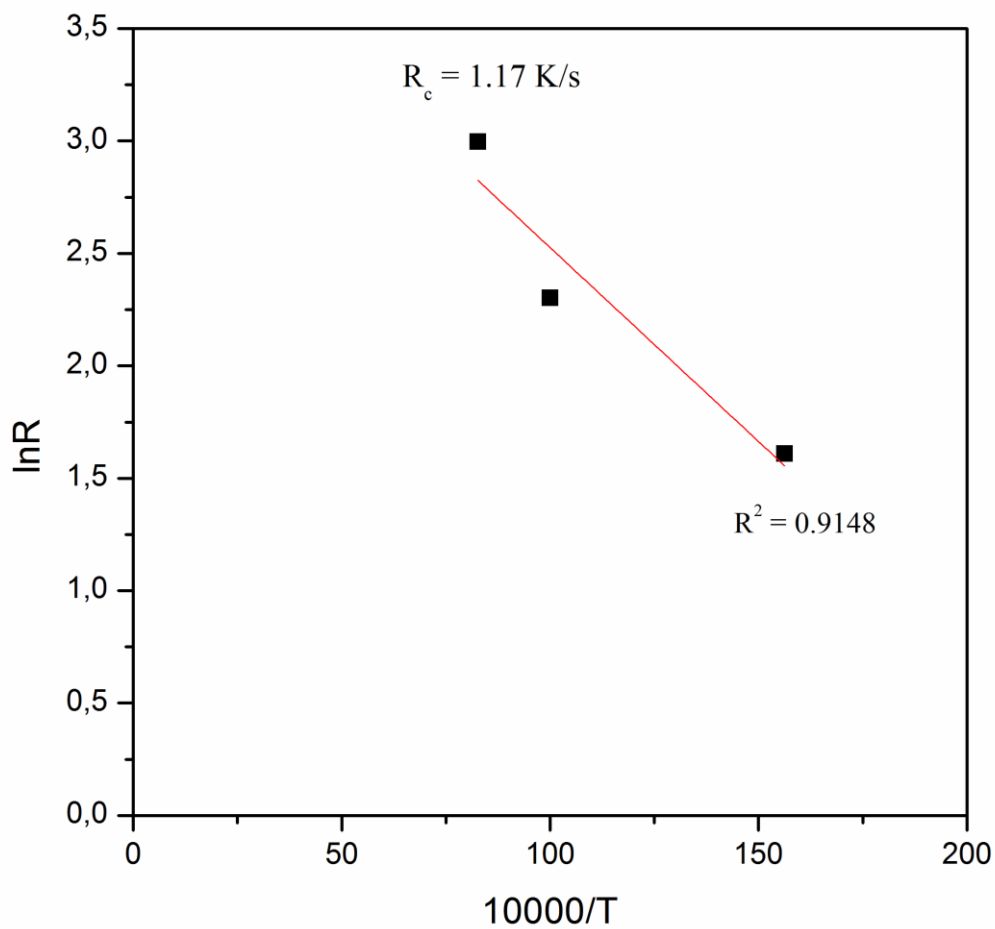


**Figure 5.22** Barandiaran-Colmenero plot for eutectic suppression of  $M_{60}Cr_{13}Mo_{10}B_8Y_2Mn_7$  BAS sample

### 5.7.3. Corrosion Studies

In order to evaluate the corrosion resistance of  $M_{60}Cr_{13}Mo_{10}B_8Y_2Mn_7$  BAS sample, immersion corrosion tests were applied. Before every test, the surfaces of the samples were polished until mirror like shiny surfaces were obtained.

Immersion tests involved three different extreme environments which were very acidic 0.5M  $H_2SO_4$  solution (pH=1.13), very basic 1M NaOH solution (pH=14) and neutral aggressive 0.6M NaCl salt solution (pH=7). BAS sample's performances were compared with the scrap pig iron which was used for the production of BAS, AISI 316 stainless steel and 1.2080 Tool Steel. The steel samples were chosen according to their carbon and alloying element, especially chromium, content in their compositions. Furthermore, the corrosion measurements of the crystalline counterpart of the BAS (near equilibrium solidified samples) could not be done due to its extreme brittleness leading to handling the sample while in preparation step.

All samples exposed to these extreme environments for 15 days and in each 5 day weight change of the specimens were investigated and weight losses were calculated according to the initial surface area of the samples. Figure 5.22, 5.23 and 5.24 show the behavior of the samples in different solutions.

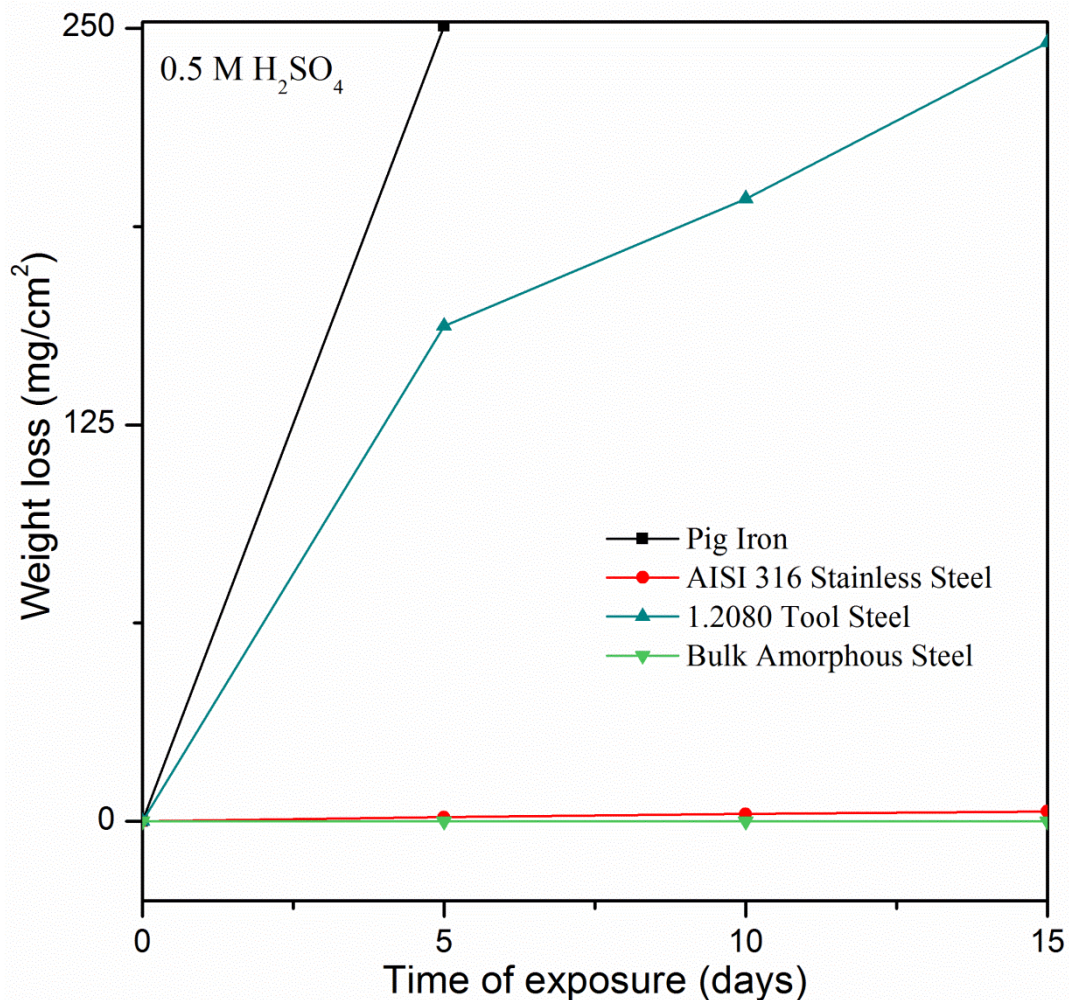


**Figure 5.23** Weight loss measurements of different samples in 0.5M H<sub>2</sub>SO<sub>4</sub> solution

The behaviors of the samples in highly acidic solution are given in Figure 5.22. While the pig iron sample decomposed immediately in acidic solution, 1.2080 tool steel lost lower weight at the initial stage. However, at the end of the 15 days, tool steel lost weight as much as pig iron sample.  $M_{60}Cr_{13}Mo_{10}B_8Y_2Mn_7$  showed no significant weight change in highly acidic solution. Furthermore, weight losses of the AISI 316 stainless steel were at low levels at the end of 15 days.

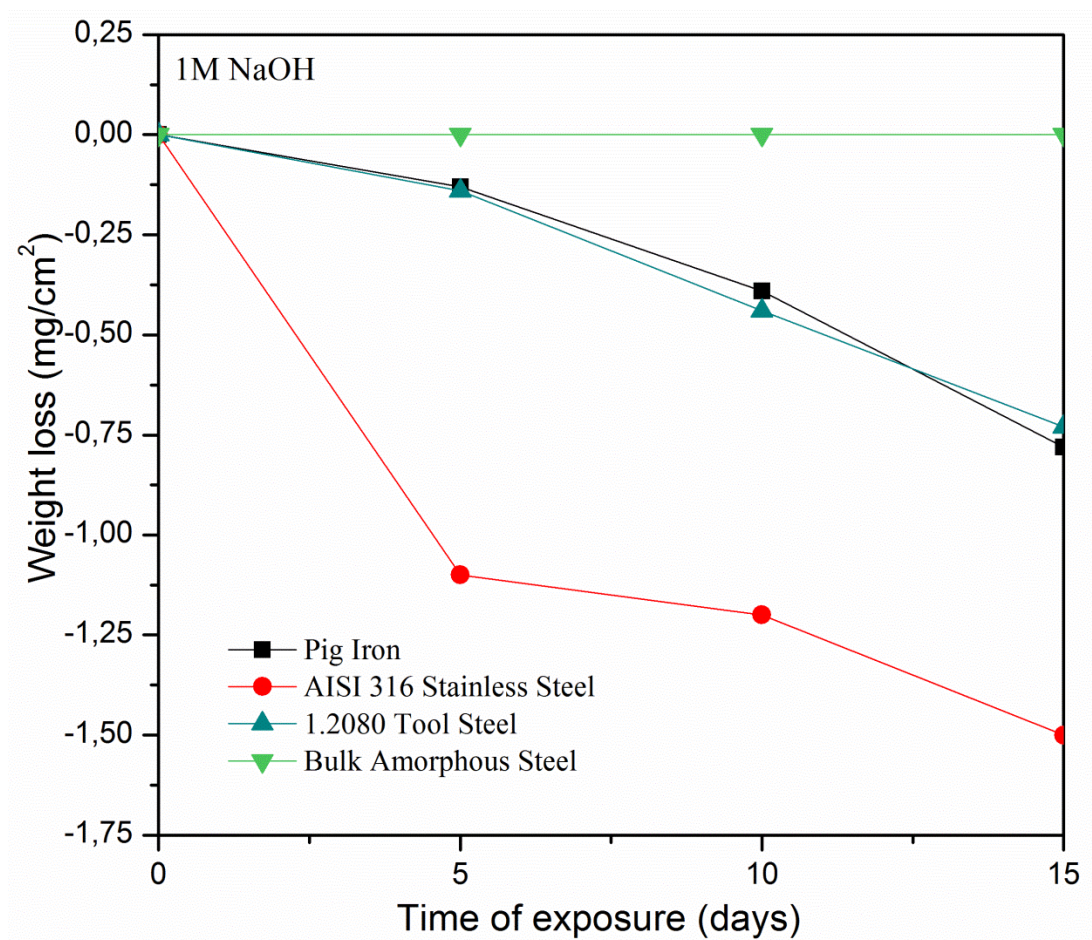


**Figure 5.24** Weight loss measurements of different samples in 1M NaOH solution

Behaviors of the samples in high pH environment were much more different than the acidic solution. According to Figure 5.23, low weight changes were observed in 1M NaOH solution. As it was detected in acidic solution, no change in weight was noticed in  $M_{60}Cr_{13}Mo_{10}B_8Y_2Mn_7$  BAS system. However, other samples showed weight gain contrary to the  $H_2SO_4$  solution. Most weight gain was spotted in AISI 316 stainless steel with  $1.5 \text{ mg/cm}^2$ . Pig iron and 1.2080 tool steel showed no significant weight gain during the stay in 15 days of basic solution.

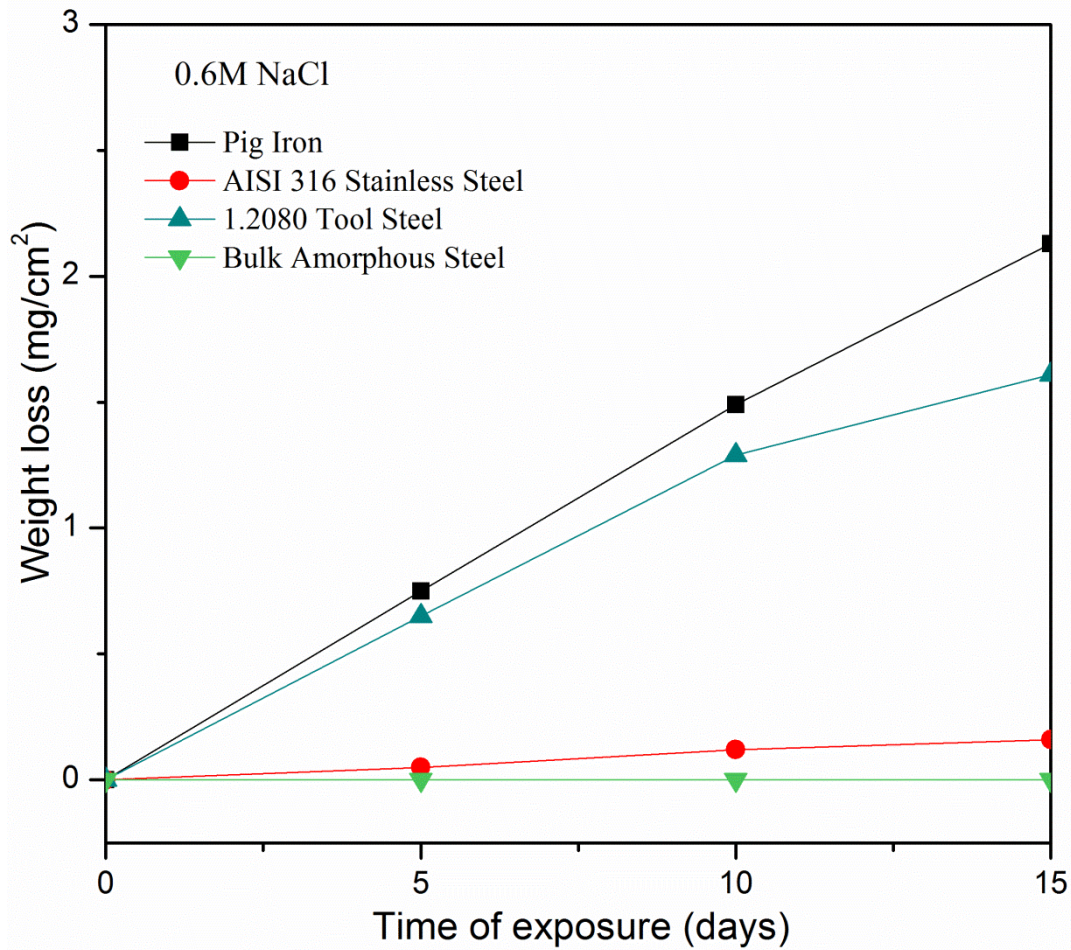


**Figure 5.25** Weight loss measurements of different samples in 1M NaOH solution

0.6M NaCl solution also affected the specimen in 15 days. Weight losses were observed in pig iron and 1.2080 tool steel in the order of 2 mg/cm<sup>2</sup>. Although weight losses seemed low, salt solution affected the surfaces of the samples. As it was expected, orange colored, highly oxidized layers were observed in mentioned specimens. Due to this oxide layer, no significant weight losses were countered in this examination. As in the other extreme environments,  $M_{60}Cr_{13}Mo_{10}B_8Y_2Mn_7$  showed no change during 15days while insignificant weight loss was observed in AISI 316 stainless steel.

#### 5.7.4. Mechanical Properties

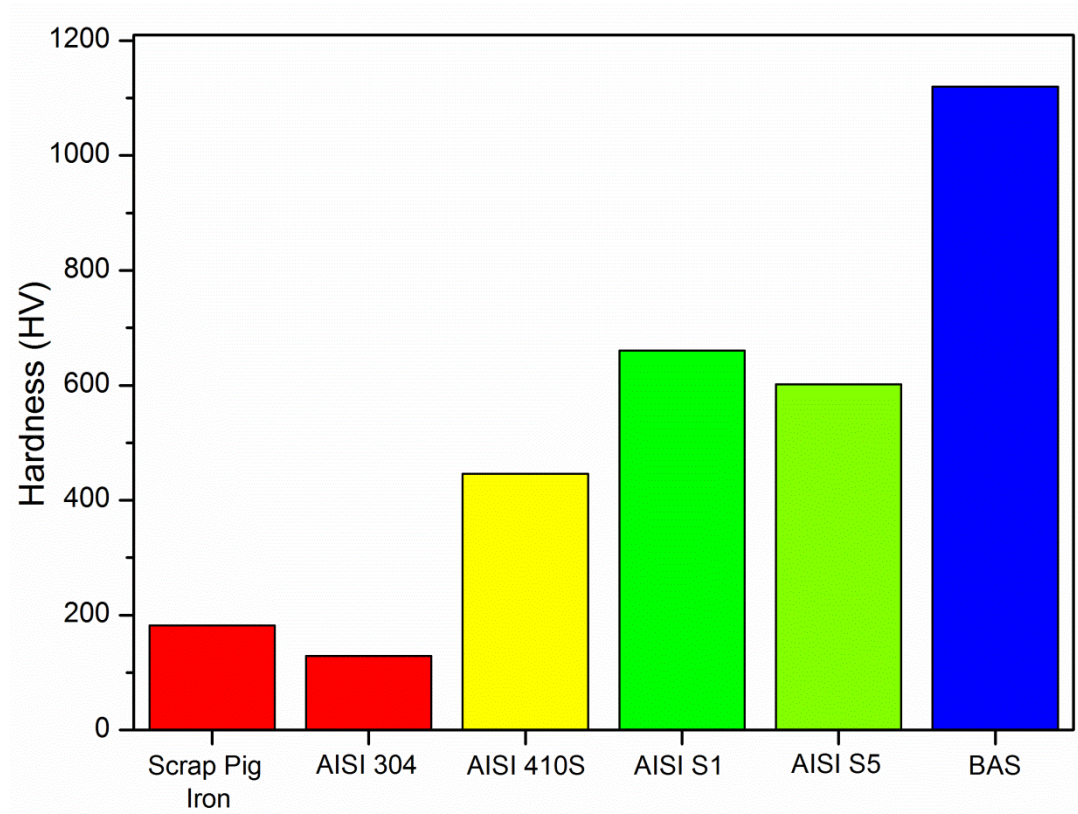


**Figure 5.26** Comparison of hardness values of  $M_{60}Cr_{13}Mo_{10}B_8Y_2Mn_7$  with conventional materials [105]

In Figure 5.25, the hardness values of the  $M_{60}Cr_{13}Mo_{10}B_8Y_2Mn_7$  sample are given with commercially available materials. It is obvious that glassy structure had a huge lead in HV when it is compared to conventional steels. Closest sample were AISI S1 tool steel with approximately 700HV while BAS had hardness values around 1180HV. Another important aspect is that amorphous alloys in this study showed extreme hardness than conventional steels. Microhardness values are comparable with previous studies about amorphous steels. For instance, Tsai et. al.[66] found microhardness around 1200Hv and 1150Hv reported from Hess et. al.[65].



## CHAPTER 6

### CONCLUSIONS

The aim of this study was to synthesize bulk amorphous steels from scrap precursors by conventional method to decrease the production costs of BAS and adapt the conditions in industry. In addition, after achieving a successfully production of the first alloy, performances of the samples tried to be enhanced by alloying different elemental additions. In order to achieve these goals, theoretical background obtained from the previous studies was combined with the knowledge from published literature which led to the successful design of the BAS systems.

In the first part of the study, bulk amorphous steel alloy was designed and developed by considering the necessities and the limitations to form glassy alloys.

- For the first time, bulk amorphous steels were produced by alloying scrap cast irons as Fe and C source with pure constituent elements; Cr, Mo, B, Y.
- High  $T_g$  (818K) with extremely wide supercooled liquid region (~120K) was observed in synthesized base alloy,  $M_{60}Cr_{13}Mo_{17}B_8Y_2$ . Preliminary results showed that, iron carbides were the dominant phase in this BAS sample.
- Addition elements such as Ti, V, Al and Mn were chosen because of their iron carbide destabilizer natures, and their effects were investigated. Analysis results showed that best alloying addition to reach fully amorphous state and enhanced thermal stability was Al and Mn addition to the base alloy.
- Additional investigations were applied to determine the best alloying element addition to the base alloy with same amount of Mo substitution. These results indicated that, as the Al content of the system increased,  $\alpha$ -Fe stabilization with vanishing the amorphous phase was observed. On the other hand, as the Mn content in the system was increased, the amorphous phase

became more stable and thermal characteristics were enhanced. So best alloying addition for the improvement of the amorphous structure and the thermal stability of the system determined as Mn.

In the second part, effects of Mn addition to base alloy were investigated in detail by microalloying method. In this method eleven different compositions were prepared and synthesized based on  $M_{60}Cr_{13}Mo_{17-x}B_8Y_2Mn_x$  where x varies from 0 to 10.

- While DSC thermogrammes showed that all samples contained glassy phase in their structures, XRD results indicated that after 5at.% Mn addition, specimens reached the fully amorphous state.
- By considering both experimental results and theoretical parameters, optimized Mn content determined as 7at.%. This system could be classified as one of the best BAS composition with respect to thermal characteristics.
- Fully amorphous state of this BAS was confirmed with XRD, DSC and VSM. This system behaved as a perfect paramagnet and showed  $T_g$  near 870K with relatively low  $\Delta T_x$  ( $=25K$ ), but superior GFA. Even in slowly cooled part of the sample, amorphous phase was observed.
- $M_{60}Cr_{13}Mo_{10}B_8Y_2Mn_7$  BAS system showed very high resistance to corrosion in different extreme conditions, high glass forming ability with low necessity of cooling rate among Fe-based BMGs and BAS systems and high hardness compared to conventional steels.

#### Recommendations For Future Studies:

- i. Compression tests can be applied to the optimized BAS sample to characterize the behavior compressive load. To characterize even further, nanoindentation hardness tests might be used to determine specific properties such as Poisson's ratio, Young's modulus and fracture strength.
- ii. In-situ X-ray measurements and synchrotron studies could be a useful tool to determine the phases nucleated in crystallization events and to understand

the crystallization mechanism and the phase transformations behind these systems.

- iii. Isothermal crystallization kinetics is another tool to reveal the mechanism behind the crystallization. Avrami exponent and the nucleation mechanism could be solved by applying this method.
- iv. Magnetic monitoring approach might be used to characterize the magnetic behavior of the nucleated and transformed phases.



## REFERENCES

- [1] W. Klement, R. Willens, P. Duwez, Non-crystalline structure in solidified gold–silicon alloys, *Nature*, (1960).
- [2] A.L. Greer, Metallic glasses, *Science*, 267 (1995) 1947-1953.
- [3] H. Chen, D. Turnbull, Evidence of a glass–liquid transition in a gold–germanium–silicon alloy, *The Journal of Chemical Physics*, 48 (1968) 2560-2571.
- [4] D. Turnbull, Under what conditions can a glass be formed?, *Contemporary physics*, 10 (1969) 473-488.
- [5] T. Zhang, A. Inoue, T. Masumoto, Amorphous Zr-Al-TM (TM= Co, Ni, Cu) alloys with significant supercooled liquid region of over 100 K, *Mater. Trans. JIM*, 32 (1991) 1005-1010.
- [6] A. Inoue, Stabilization of metallic supercooled liquid and bulk amorphous alloys, *Acta materialia*, 48 (2000) 279-306.
- [7] A. Inoue, A. Takeuchi, Recent development and application products of bulk glassy alloys, *Acta Materialia*, 59 (2011) 2243-2267.
- [8] A. Drehman, A. Greer, D. Turnbull, Bulk formation of a metallic glass: Pd<sub>40</sub>Ni<sub>40</sub>P<sub>20</sub>, *Applied Physics Letters*, 41 (1982) 716-717.
- [9] H. Kui, A.L. Greer, D. Turnbull, Formation of bulk metallic glass by fluxing, *Applied Physics Letters*, 45 (1984) 615-616.

- [10] A. Inoue, Y. Shinohara, J.S. Gook, Thermal and magnetic properties of bulk Fe-based glassy alloys prepared by copper mold casting, *Materials transactions-JIM*, 36 (1995) 1427-1433.
- [11] V. Ponnambalam, S.J. Poon, G.J. Shiflet, V.M. Keppens, R. Taylor, G. Petculescu, Synthesis of iron-based bulk metallic glasses as nonferromagnetic amorphous steel alloys, *Applied Physics Letters*, 83 (2003) 1131-1133.
- [12] V. Ponnambalam, S.J. Poon, G.J. Shiflet, Fe-based bulk metallic glasses with diameter thickness larger than one centimeter, *Journal of Materials Research*, 19 (2004) 1320-1323.
- [13] Z. Lu, C. Liu, J. Thompson, W. Porter, Structural amorphous steels, *Physical Review Letters*, 92 (2004) 245503.
- [14] H. Chen, D. Turnbull, Formation, stability and structure of palladium-silicon based alloy glasses, *Acta Metallurgica*, 17 (1969) 1021-1031.
- [15] D. Turnbull, M.H. Cohen, Free-volume model of the amorphous phase: glass transition, *The Journal of Chemical Physics*, 34 (1961) 120-125.
- [16] H. Chen, Thermodynamic considerations on the formation and stability of metallic glasses, *Acta Metallurgica*, 22 (1974) 1505-1511.
- [17] C. Suryanarayana, A. Inoue, *Bulk metallic glasses*, CRC Press, 2011.
- [18] C.A. Angell, Formation of glasses from liquids and biopolymers, *Science*, 267 (1995) 1924-1935.
- [19] W.-H. Wang, C. Dong, C. Shek, *Bulk metallic glasses*, *Materials Science and Engineering: R: Reports*, 44 (2004) 45-89.

- [20] R. Busch, W. Liu, W. Johnson, Thermodynamics and kinetics of the Mg<sub>65</sub>Cu<sub>25</sub>Y<sub>10</sub> bulk metallic glass forming liquid, *Journal of applied physics*, 83 (1998) 4134-4141.
- [21] A. Inoue, Recent progress of Zr-based bulk amorphous alloys, (1996).
- [22] A.L. Greer, Confusion by design, *Nature: International weekly journal of science*, 366 (1993) 303-304.
- [23] O. Senkov, D. Miracle, Effect of the atomic size distribution on glass forming ability of amorphous metallic alloys, *Materials Research Bulletin*, 36 (2001) 2183-2198.
- [24] O. Senkov, D. Miracle, A topological model for metallic glass formation, *Journal of non-crystalline solids*, 317 (2003) 34-39.
- [25] M.K. Pehlivanoglu, M.V. Akdeniz, A.Ş. Bor, Structural characterization of iron-based bulk metallic glass alloys produced by centrifugal casting, *Chemical Engineering Communications*, 190 (2003) 925-935.
- [26] J. Eckert, N. Mattern, M. Zinkevitch, M. Seidel, Crystallization behavior and phase formation in Zr-Al-Cu-Ni metallic glass containing oxygen, *Materials Transactions, JIM(Japan)*, 39 (1998) 623-632.
- [27] H. Chen, J. Krause, E. Coleman, Elastic constants, hardness and their implications to flow properties of metallic glasses, *Journal of Non-Crystalline Solids*, 18 (1975) 157-171.
- [28] A. Inoue, K. Ohtera, K. Kita, T. Masumoto, New amorphous Mg-Ce-Ni alloys with high strength and good ductility, *Japanese journal of applied physics*, 27 (1988) L2248.

- [29] A. Inoue, K. Ohtera, K. Kita, T. Masumoto, New amorphous alloys with good ductility in Al-Ce-M (M= Nb, Fe, Co, Ni or Cu) systems, Japanese journal of applied physics, 27 (1988) L1796.
- [30] A. Inoue, T. Zhang, T. Masumoto, Al--La--Ni Amorphous Alloys With a Wide Supercooled Liquid Region, Materials transactions, JIM, 30 (1989) 965-972.
- [31] A. Peker, W.L. Johnson, A highly processable metallic glass: Zr<sub>41</sub>. 2Ti<sub>13</sub>. 8Cu<sub>12</sub>. 5Ni<sub>10</sub>. 0Be<sub>22</sub>. 5, Applied Physics Letters, 63 (1993) 2342-2344.
- [32] A. Inoue, N. Nishiyama, T. Masumoto, Preparation of bulk glassy Pd<sub>40</sub>Ni<sub>10</sub>Cu<sub>30</sub>P<sub>20</sub> alloy of 40 mm in diameter by water quenching, Materials Transactions, JIM, 37 (1996) 181.
- [33] T. Shen, Y. He, R. Schwarz, Bulk amorphous Pd–Ni–Fe–P alloys: preparation and characterization, Journal of materials research, 14 (1999) 2107-2115.
- [34] A. Inoue, W. Zhang, T. Zhang, K. Kurosaka, High-strength Cu-based bulk glassy alloys in Cu–Zr–Ti and Cu–Hf–Ti ternary systems, Acta Materialia, 49 (2001) 2645-2652.
- [35] W. Zhang, A. Inoue, Thermal stability and mechanical properties of Cu-Hf-Al base bulk glassy alloys with a large supercooled liquid region of over 100 K, Mater. Trans, 44 (2003) 2346-2349.
- [36] F. Guo, S.J. Poon, G.J. Shiflet, Metallic glass ingots based on yttrium, Applied Physics Letters, 83 (2003) 2575-2577.
- [37] J. Schroers, W.L. Johnson, Highly processable bulk metallic glass-forming alloys in the Pt–Co–Ni–Cu–P system, Applied physics letters, 84 (2004) 3666-3668.

- [38] J. Schroers, B. Lohwongwatana, W.L. Johnson, A. Peker, Gold based bulk metallic glass, *Applied physics letters*, 87 (2005) 061912-061912-061913.
- [39] A. Inoue, T. Zhang, T. Itoi, A. Takeuchi, New Fe-Co-Ni-Zr-B amorphous alloys with wide supercooled liquid regions and good soft magnetic properties, *Materials Transactions, JIM*, 38 (1997) 359-362.
- [40] A. Inoue, W. Zhang, New Fe-based amorphous alloys with large magnetostriction and wide supercooled liquid region before crystallization, *Journal of applied physics*, 85 (1999) 4491-4493.
- [41] T. Shen, R. Schwarz, Bulk ferromagnetic glasses prepared by flux melting and water quenching, *Applied Physics Letters*, 75 (1999) 49-51.
- [42] H. Koshiba, A. Inoue, A. Makino, Fe-based soft magnetic amorphous alloys with a wide supercooled liquid region, *Journal of applied physics*, 85 (1999) 5136-5138.
- [43] S. Joseph, G.J. Shiflet, V. Ponnambalam, V.M. Keppens, R. Taylor, G. Petculescu, Synthesis and Properties of High-Manganese Iron-Based Bulk Amorphous Metals as Non-Ferromagnetic Amorphous Steel Alloys, in: *MRS Proceedings*, Cambridge Univ Press, 2002, pp. CC1. 2.
- [44] V. Ponnambalam, S.J. Poon, G.J. Shiflet, Fe-Mn-Cr-Mo-(Y, Ln)-C-B (Ln=Lanthanides) bulk metallic glasses as formable amorphous steel alloys, *Journal of materials research*, 19 (2004) 3046-3052.
- [45] L. Xing, J. Eckert, W. Löser, S. Roth, L. Schultz, Atomic ordering and magnetic properties in Nd<sub>57</sub>Fe<sub>20</sub>B<sub>8</sub>Co<sub>5</sub>Al<sub>10</sub> solids, *Journal of Applied Physics*, 88 (2000) 3565-3569.

- [46] A. Inoue, T. Zhang, A. Takeuchi, W. Zhang, Hard magnetic bulk amorphous Nd-Fe-Al alloys of 12 mm in diameter made by suction casting, *Materials Transactions, JIM(Japan)*, 37 (1996) 636-640.
- [47] B.C. Wei, Y. Zhang, Y.X. Zhuang, D.Q. Zhao, M.X. Pan, W.H. Wang, W.R. Hu, Nd 65 Al 10 Fe 25-x Co x (x= 0, 5, 10) bulk metallic glasses with wide supercooled liquid regions, *Journal of Applied Physics*, 89 (2001) 3529-3531.
- [48] A. Inoue, Bulk amorphous alloys with soft and hard magnetic properties, *Materials Science and Engineering: A*, 226 (1997) 357-363.
- [49] A. Inoue, T. Zhang, H. Koshiba, A. Makino, New bulk amorphous Fe-(Co, Ni)-M-B (M= Zr, Hf, Nb, Ta, Mo, W) alloys with good soft magnetic properties, *Journal of applied physics*, 83 (1998) 6326-6328.
- [50] T. Shen, R. Schwarz, Bulk ferromagnetic glasses in the Fe-Ni-P-B system, *Acta materialia*, 49 (2001) 837-847.
- [51] F. Spaepen, A microscopic mechanism for steady state inhomogeneous flow in metallic glasses, *Acta metallurgica*, 25 (1977) 407-415.
- [52] A. Argon, Plastic deformation in metallic glasses, *Acta metallurgica*, 27 (1979) 47-58.
- [53] P. Steif, F. Spaepen, J. Hutchinson, Strain localization in amorphous metals, *Acta Metallurgica*, 30 (1982) 447-455.
- [54] C.A. Schuh, T.C. Hufnagel, U. Ramamurty, Mechanical behavior of amorphous alloys, *Acta Materialia*, 55 (2007) 4067-4109.

- [55] J. Lewandowski, A. Greer, Temperature rise at shear bands in metallic glasses, *Nature Materials*, 5 (2005) 15-18.
- [56] H. Leamy, T. Wang, H. Chen, Plastic flow and fracture of metallic glass, *Metallurgical Transactions*, 3 (1972) 699-708.
- [57] Y. Kawamura, T. Shibata, A. Inoue, T. Masumoto, Workability of the supercooled liquid in the Zr<sub>65</sub>Al<sub>10</sub>Ni<sub>10</sub>Cu<sub>15</sub> bulk metallic glass, *Acta materialia*, 46 (1998) 253-263.
- [58] G. Wang, S. Fang, X. Xiao, Q. Hua, J. Gu, Y. Dong, Microstructure and properties of Zr<sub>65</sub>Al<sub>10</sub>Ni<sub>10</sub>Cu<sub>15</sub> amorphous plates rolled in the supercooled liquid region, *Materials science & engineering. A, Structural materials: properties, microstructure and processing*, 373 (2004) 217-220.
- [59] Y. Kawamura, T. Nakamura, K.B. Kim, Superplasticity in Pd<sub>40</sub>Ni<sub>40</sub>P<sub>20</sub> metallic glass, in: *Materials science forum*, Trans Tech Publ, 1999, pp. 349-354.
- [60] J. Schroers, N. Paton, Amorphous metal alloys, *Advanced materials & processes*, (2006) 61.
- [61] X. Gu, S.J. Poon, G.J. Shiflet, Mechanical properties of iron-based bulk metallic glasses, *Journal of materials research*, 22 (2006) 344-351.
- [62] X. Gu, S.J. Poon, G.J. Shiflet, M. Widom, Mechanical properties, glass transition temperature, and bond enthalpy trends of high metalloid Fe-based bulk metallic glasses, *Applied Physics Letters*, 92 (2008) 161910-161910-161913.
- [63] X. Gu, S.J. Poon, G.J. Shiflet, Effects of carbon content on the mechanical properties of amorphous steel alloys, *Scripta materialia*, 57 (2007) 289-292.

[64] M. Iqbal, J. Akhter, H. Zhang, Z. Hu, Synthesis and characterization of bulk amorphous steels, *Journal of Non-Crystalline Solids*, 354 (2008) 3284-3290.

[65] P.A. Hess, S.J. Poon, G. Shiflet, R.H. Dauskardt, Indentation fracture toughness of amorphous steel, *Journal of materials research*, 20 (2005) 783-786.

[66] P. Tsai, A. Xiao, J. Li, J. Jang, J. Chu, J. Huang, Prominent Fe-based bulk amorphous steel alloy with large supercooled liquid region and superior corrosion resistance, *Journal of Alloys and Compounds*, 586 (2013) 94-98.

[67] W. Zhang, A. Inoue, Thermal and magnetic properties of Fe-Co-Ln-B (Ln= Nd, Sm, Tb or Dy) amorphous alloys with high magnetostriction, *Materials Transactions, JIM(Japan)*, 40 (1999) 78-81.

[68] T. Itoi, A. Inoue, High-frequency permeability of (Fe, Co, Ni) 62Nb8B30 amorphous alloys with a wide supercooled liquid region, *Applied physics letters*, 74 (1999) 2510-2512.

[69] S. Pang, T. Zhang, K. Asami, A. Inoue, New Fe-Cr-Mo-(Nb, Ta)-CB glassy alloys with high glass-forming ability and good corrosion resistance, *Materials transactions-JIM*, 42 (2001) 376-379.

[70] S. Pang, T. Zhang, K. Asami, A. Inoue, Synthesis of Fe-Cr-Mo-C-B-P bulk metallic glasses with high corrosion resistance, *Acta Materialia*, 50 (2002) 489-497.

[71] A. Inoue, B. Shen, A. Yavari, A. Greer, Mechanical properties of Fe-based bulk glassy alloys in Fe-B-Si-Nb and Fe-Ga-P-C-B-Si systems, *Journal of materials research*, 18 (2003) 1487-1492.

- [72] C. Qing-Jun, S. Jun, F. Hong-Bo, S. Jian-Fei, H. Yong-Jiang, D. McCartney, Glass-forming ability of an iron-based alloy enhanced by Co addition and evaluated by a new criterion, *Chinese Physics Letters*, 22 (2005) 1736.
- [73] P. Gostin, A. Gebert, L. Schultz, Comparison of the corrosion of bulk amorphous steel with conventional steel, *Corrosion Science*, 52 (2010) 273-281.
- [74] Z. Wang, J. Zhang, X. Chang, W. Hou, J. Wang, Susceptibility of minor alloying to corrosion behavior in yttrium-containing bulk amorphous steel, *Intermetallics*, 16 (2008) 1036-1039.
- [75] H. Fang, X. Hui, G. Chen, Effects of Mn addition on the magnetic property and corrosion resistance of bulk amorphous steels, *Journal of Alloys and Compounds*, 464 (2008) 292-295.
- [76] J. Farmer, J. Haslam, S. Day, T. Lian, C. Saw, P. Hailey, J. Choi, R. Rebak, N. Yang, J. Payer, Corrosion resistance of thermally sprayed high-boron iron-based amorphous-metal coatings: Fe<sub>49</sub>. 7Cr<sub>17</sub>. 7Mn<sub>1</sub>. 9Mo<sub>7</sub>. 4W<sub>1</sub>. 6B<sub>15</sub>. 2C<sub>3</sub>. 8Si<sub>2</sub>. 4, *Journal of materials research*, 22 (2007) 2297-2311.
- [77] J. Farmer, J. Choi, C. Saw, R. Rebak, S. Day, T. Lian, P. Hailey, J. Payer, D. Branagan, L. Aprigliano, Corrosion Resistance of Amorphous Fe<sub>49</sub>. 7Cr<sub>17</sub>. 7Mn<sub>1</sub>. 9Mo<sub>7</sub>. 4W<sub>1</sub>. 6B<sub>15</sub>. 2C<sub>3</sub>. 8Si<sub>2</sub>. 4 coating-a new criticality-controlled material, *Journal of Nuclear Technology*, vol. 161, no. 2, March 1, 2008, pp. 169-189, 161 (2007).
- [78] C. Luo, Y. Zhao, X. Xi, G. Wang, D. Zhao, M. Pan, W. Wang, S. Kou, Making amorphous steel in air by rare earth microalloying, *Journal of non-crystalline solids*, 352 (2006) 185-188.

- [79] H. Li, S. Yi, H.S. Sohn, Fe-based bulk metallic glasses Fe<sub>73</sub>. 8- xC<sub>7</sub>. 0Si<sub>3</sub>. 5BxP<sub>9</sub>. 6Cr<sub>2</sub>. 1Mo<sub>2</sub>. 0Al<sub>2</sub>. 0 (x= 3~ 9) prepared using hot metal and industrial raw materials, *Journal of materials research*, 22 (2007) 164-168.
- [80] X. Gu, A. McDermott, S.J. Poon, G.J. Shiflet, Critical Poisson's ratio for plasticity in Fe-Mo-C-B-Ln bulk amorphous steel, *Applied physics letters*, 88 (2006) 211905.
- [81] J. Pan, Q. Chen, N. Li, L. Liu, Formation of centimeter Fe-based bulk metallic glasses in low vacuum environment, *Journal of Alloys and Compounds*, 463 (2007) 246-249.
- [82] X. Gu, S.J. Poon, G.J. Shiflet, M. Widom, Ductility improvement of amorphous steels: Roles of shear modulus and electronic structure, *Acta Materialia*, 56 (2007) 88-94.
- [83] M.D. Demetriou, G. Kaltenboeck, J.-Y. Suh, G. Garrett, M. Floyd, C. Crewdson, D.C. Hofmann, H. Kozachkov, A. Wiest, J.P. Schramm, Glassy steel optimized for glass-forming ability and toughness, *Applied Physics Letters*, 95 (2009) 041907.
- [84] W.H. Wang, Roles of minor additions in formation and properties of bulk metallic glasses, *Progress in Materials Science*, 52 (2007) 540-596.
- [85] D. Xu, G. Duan, W.L. Johnson, Unusual glass-forming ability of bulk amorphous alloys based on ordinary metal copper, *Physical review letters*, 92 (2004) 245504.
- [86] B. Murty, D. Ping, K. Hono, A. Inoue, Influence of oxygen on the crystallization behavior of Zr<sub>65</sub>Cu<sub>27</sub>. 5Al<sub>7</sub>. 5 and Zr<sub>66</sub>. 7Cu<sub>33</sub>. 3 metallic glasses, *Acta materialia*, 48 (2000) 3985.

- [87] W. Wang, M. Pan, D. Zhao, Y. Hu, H. Bai, Enhancement of the soft magnetic properties of FeCoZrMoWB bulk metallic glass by microalloying, *Journal of Physics: Condensed Matter*, 16 (2004) 3719.
- [88] S.N. Gurbuz, Synthesis And Characterization Of Bulk Glass-Forming Iron-Boron Based Alloy Systems, In, Middle East Technical University, 2004.
- [89] M.V. Akdeniz, A.O. Mekhrabov, M.K. Pehlivanoglu, Solidification behaviour of bulk glass-forming alloy systems, *Journal of alloys and compounds*, 386 (2005) 185-191.
- [90] Z. Lu, C. Liu, A new glass-forming ability criterion for bulk metallic glasses, *Acta Materialia*, 50 (2002) 3501-3512.
- [91] X.H. Du, J.C. Huang, C.T. Liu, Z.P. Lu, New criterion of glass forming ability for bulk metallic glasses, *Journal of Applied Physics*, 101 (2007) -.
- [92] K. Mondal, B. Murty, On the parameters to assess the glass forming ability of liquids, *Journal of non-crystalline solids*, 351 (2005) 1366-1371.
- [93] Z. Long, G. Xie, H. Wei, X. Su, J. Peng, P. Zhang, A. Inoue, On the new criterion to assess the glass-forming ability of metallic alloys, *Materials Science and Engineering: A*, 509 (2009) 23-30.
- [94] A. Inoue, A. Takeuchi, High strength bulk amorphous alloys, *Mater. Trans. JIM*, 43 (2002) 1892-1906.
- [95] H.E. Kissinger, Reaction kinetics in differential thermal analysis, *Analytical chemistry*, 29 (1957) 1702-1706.

- [96] T. Ozawa, A new method of analyzing thermogravimetric data, *Bulletin of the chemical society of Japan*, 38 (1965) 1881-1886.
- [97] T. Ozawa, Kinetics of non-isothermal crystallization, *Polymer*, 12 (1971) 150-158.
- [98] J. Barandiaran, J. Colmenero, Continuous cooling approximation for the formation of a glass, *Journal of Non-Crystalline Solids*, 46 (1981) 277-287.
- [99] E. Mittemeijer, Analysis of the kinetics of phase transformations, *Journal of Materials science*, 27 (1992) 3977-3987.
- [100] M. Avrami, Kinetics of phase change. I General theory, *The Journal of Chemical Physics*, 7 (1939) 1103-1112.
- [101] S.R. Shatynski, The thermochemistry of transition metal carbides, *Oxidation of Metals*, 13 (1979) 105-118.
- [102] C.K. Ande, M.H. Sluiter, First-Principles Calculations on Stabilization of Iron Carbides ( $\text{Fe}_3\text{C}$ ,  $\text{Fe}_5\text{C}_2$ , and  $\eta\text{-Fe}_2\text{C}$ ) in Steels by Common Alloying Elements, *Metallurgical and Materials Transactions A*, 43 (2012) 4436-4444.
- [103] H. Bhadeshia, R. Honeycombe, *Steels: Microstructure and Properties: Microstructure and Properties*, Butterworth-Heinemann, 2011.
- [104] M. Yildirim, M.V. Akdeniz, A.O. Mekhrabov, Microstructural Investigation and Phase Relationships of Fe-Al-Hf Alloys, *Metallurgical and Materials Transactions A*, 45 (2014) 3412-3421.
- [105] Online Materials Information Resource, in, online, 2014.

## APPENDIX A

### T<sub>g</sub> CALCULATION

The glass transition temperatures of the samples were calculated by tangent method.

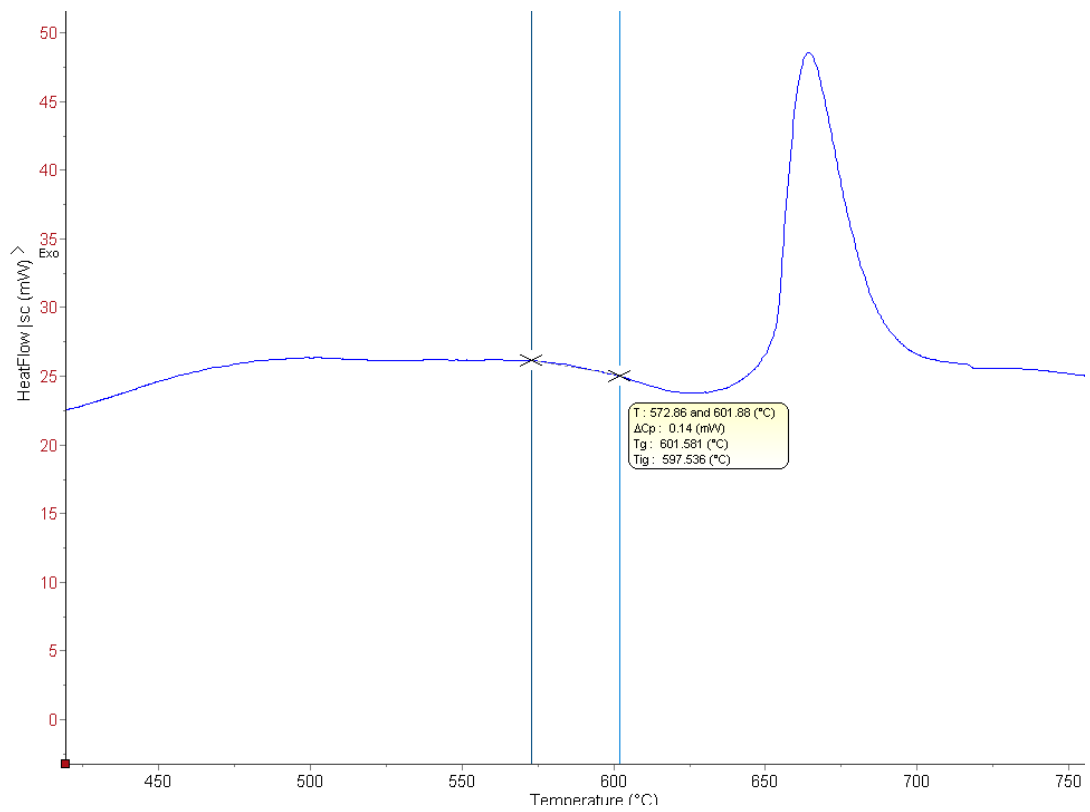


**Figure A.1** Example of T<sub>g</sub> calculation by SETARAM thermal analysis software